Università di Napoli "Federico II"

Scuola di Dottorato in Ingegneria Industriale

Dottorato in "Tecnologie Innovative per Materiali, Sensori ed Imaging" XXI ciclo.

Dynamic measurements for the electrical characterization of organic materials and related devices

Coordinatore:

Prof. Giancarlo Abbate

Candidato:

Dr. Pasquale D'Angelo

CONTENTS

List of figures……VI

List of tables……..XII

List of publications……..XIII

List of symbols and abbreviations……XIV

Introduction…….....1

Chapter I.

Dynamic electrical measurement techniques employed in materials and devices characterization.

1.1) Organic Electronics and role of the electrical Measurements…….....6

1.2) Electrical dynamic characterization techniques of organic materials and related devices: from static dc measurements to dynamic ac measurements…….9

1.2.a) Static electrical characterization: fundaments, utility and limitations……...……10

1.2.b) Standard dynamic electrical measurements:

Impedance Spectroscopy technique(IS)…….……14

1.2.c) Debye model vs. Universal Dielectric Response (UDR) model……..19

1.2.d) ac measurements on amorphous materials……...24

1.2.e) ac measurements on organic based Thin Film Transistors……...29

1.3) Dynamic measurements on materials and devices: motivations and experimental set-up...……...34

Chapter II

Dynamic electrical characterization of organic materials.

2.1) Introduction: IS technique for the characterization of organic materials……..40

2.2) Conducting properties of organic semiconductors: properties of thiophene-based semiconductors……..42

2.2.a) Preliminary dc characterization: sample preparation, structural and morphological characterization; experimental results……..43

2.2.b) ac measurements on thiophene-based polymeric thin films: conduction mechanisms in polthiophenes……..51

2.3) Phase transitions in organic based dielectric materials…….57

2.3.a) Phase transition in organic materials: standard techniques versus Impedance Spectroscopy for the evaluation of glass and melting transition temperatures……..57

2.3.b) ac measurements on dielectric Polydimethylsiloxane; sample preparation; experimental results……....61

Chapter III

ac electrical characterization of organic devices.

3.1) ac measurements on electronic devices: bulk properties……...71

3.1.a) ac measurements on polysilsequioxanic-based humidity sensors: device manufacturing and dc operating properties……...72

3.1.b) ac measurements on polysilsequioxanic-based humidity sensors: experimental results; effect of the glass transition on device working mechanisms……...76

3.1.c) ac measurements on conventional ITO/TPD:Alq_3/Al light emitting diode: study of the electro-optical degradation mechanisms…….80

3.2) ac measurements on electronic devices: interfacial properties……...85

3.2.a) ac measurements on organic Spin Valves: remind to operating properties, device manufacturing and experimental

details……..86

3.2.b) Comparison between ITO/Alq_3 and LSMO/Alq_3 interfaces: role of the manganite on magnetoresistive effect……...88

3.3) ac measurement techniques for the characterization of bottom contact OFETs properties……..96

3.3.a) Pentacene-based devices; device manufacturing and main features……..……96

3.3.b) Evaluation of static and dynamic device parameters…….100

Chapter IV

Dynamic study of stress phenomena in organic based Thin Film Transistors (TFT).

4.1) Introduction on bias stress phenomenology: shift of threshold voltage…….107

4.2) Hysteresis in transfer characteristics: a novel parameter for the study of charge trapping phenomena at gate dielectric/organic semiconductor interface……..113

4.2.a) Dynamic analysis of stress phenomena in pentacene TFTs……..117

4.3) A working cause: morphological effects on OTFT properties…….126

4.3.a) Theoretical features of Organic Molecular Beam Deposition (OMBD)……129

4.3.b) Morphological study of pentacene grown on SiO_2 substrates and correlation with TFTs transport properties……..……..132

4.3.c) Future developments: trapping phenomena versus morphology……...138

Conclusions……...141

References……145

Table of Figures.

Figure I.1. Broadband dielectric spectroscopy; the frequency windows in which the systems indicated (such as porous materials or glasses) interact with the external varying field are approximately indicated.

Figure I.2. Parallel Mode Representation; the complex impedance of the system is given by a parallel between a capacitor (imaginary part of Z; Z_i) and a resistance (real part of Z; Z_R), where the capacitor contains information on the permittivity (real part of the complex dielectric function) while the resistance expressing the losses through the material gives information about the ac conductivity σ_{ac} (linked to ε'', the imaginary part of the complex dielectric function).

Figure I.3. Parallel mode representation in the case of a basic device structure (typically, a metal/organic/metal heterojunction).

Figure I.4. UDR behavior of ac conductivity described by eq. (21). The low frequency contribution is given by a dc behavior, while the red-circled behavior describes the power-law dependence at higher frequencies.

Figure I.5. a) Temperature dependence of the index s in the case of different basic conduction models: Correlated Barrier Hopping (CBH), Overlapping Large Polaron tunneling (OLP), Quantum Mechanical Tunneling (QMT) and Small Polaron quantum mechanical tunneling (SP). Cases (i), (ii) regarding the OLP are reported for two values of the parameter r_0. Here, for SP and OLP the values of barrier height W_H = 0.2 and 0.26 eV have been chosen, respectively, while for CBH W= 1.85 eV has been used. Finally, $\omega\tau_0=10^{-9}$ has been assumed. b) Frequency dependence of the index s for the proposed microscopic transport mechanisms. For the OLP the reduced polaron radius has been fixed at 20 (i) and 2.5 (ii); W_H/kT value for SP and OLP has been considered equal to 10 while W_{eff}/KT for CBH is assumed to be equal to 75.

Figure I.6. Scheme of the ac measurement technique for the characterization of BC OTFTs.

Figure I.7. TFT in terms of a transmission line model (TLM) based on a distributed RC network (MOD 1) and a finer version (MOD 2) in which both contact resistance and capacitance are considered.

Figure I.8. Experimental set-up; a) LCR meter; b) cryogenic probe station; c) view of the internal probe chamber; d) closed cycle cryocooler.

Figure II.1. Chemical structure of thiophene.

Figure II.2. Regioregularity: in-plane lamellar self-organization of polythiophene chains.

Figure II.3. Molecular structure of a) polymers and b) corresponding monomers; the poly [3-(4-octyloxyphenyl)-thiophene] is obtained for n=8.

Figure II.4. UV-Vis spectra of poly [3-(4-octyloxyphenyl)-thiophene; 1 spin coated sample, 2 sample annealed at 200°C.

Figure II.5. Schematic representation of polymers packing.

Figure II.6. Planar a) and vertical b) layouts of the injecting electrodes.

Figure II.7. I-V measurements performer on poly [3-(4-octyloxyphenyl)-thiophene] thin films in planar configurtation in a temperature range from 295 K to 350 K.

Figure II.8. Conductivity (●) and charge carriers mobility (●) as a function of temperature, extracted from the measurements showed in Fig.8 using the formulas (1.a) and (1.b), respectively.

Figure II.9. Dependence of dc conductivity vs. temperature (scattered red curve) and comparison with VRH model prediction (dashed line) in a semilog plot as a function of $1/T^{1/4}$; in the inset it is shown the relative σ(T) measurement.

Figure II.10. Dielectric constant (●) and conductivity (▲) vs. frequency; the curves, recorded at room temperature, are fitted by using the UDR model (red lines).

Figure II.11. a) Capacitance and b) conductivity as a function of frequency at different temperatures. C) Capacitance and d) conductivity temperature dependance measured for different frequencies.

Figure II.12. Frequency dependence of the index s, extracted using eq. (13), at different environmental temperatures.

Figure II.13. PDMS chemical structure.

Figure II.14. ac conductivity (symbols) vs. frequency recorded at a) 260 °C as a function of three fixed values of dc bias, equal to 0V (■), 20V (●) and 40V (▲) and b) 163 K as a function of dc bias equal to 0V (■) and 5 V (●), are reported, together with the fitting curves (straight lines).

Figure II.15. a) Permittivity vs. temperature recorded at 1 KHz and 100 mV of voltage level; b) ac conductivity vs. temperature related to the permittivity displayed in a).

Figure II.16. Permittivty vs. temperature in a restricted temperature range for three different fixed frequencies, that is 300 Hz (×), 1 KHz (○) and 100 KHz (□).

Figure II.17. Conductivity vs temperature for 4 μm PDMS sample at 300 Hz (□), 1 kHz (○), and 100 kHz (Δ). T_m increases by increasing the frequency of the applied field (black line).

Figure II.18. Conductivity vs temperature for a fixed ac field (1 kHz and 100 mV of voltage level) performed on capacitive cells having the following geometries ($S \times d$): 9 $mm^2 \times 4$ μm (▲) and 20 $mm^{2\times}5$ μm (□). The glassy region is indicated with a circle.

Figure III.1. Poly (propylmethacryl-heptaisobutyl-POSS)-co-(N-butylmethacrylate) chemical structure.

Figure III.2. 15% POSS based sensors typical dynamic response as a function of different steps of humidity. The red line shows the relative humidity percentage in the chamber measured with a commercial humidity probe sensor.

Figure III.3. a) Capacitance (○) and ac conductivity (Δ) versus frequency for samples with a content in weight of cages equal to 25%, recorded in air at room temperature and; b) analogous measurement for 25% POSS based samples. The capacitance and conductivity are again indicated with the symbols (○) and (Δ), respectively.

Figure III.4. Permittivity (a) and conductivity (b) vs. temperature recorded at fixed frequencies, equal to 100 Hz (○) and 1 KHz (Δ), with a field amplitude equal to 0.1 V for 25 % POSS film. The inset in fig. b) shows the peak at 100 Hz in a linear scale. The black arrow in fig.a) shows the expected frequency dependence of T_g value (see Chapter II).

Figure III.5. Permittivity (a) and conductivity (b) vs. temperature recorded at 100 KHz with a field amplitude equal to 0.1 V for 15 % POSS film**.**

Figure III.6. TPD (a) and Alq3 (b) chemical structures.

Figure III.7. Optical (electroluminescence in arbitrary unities vs. Voltage) and electrical (current in arbitrary unities vs. voltage) device detriment. The temperature due to self-heating is monitored by an IR camera from the bottom of the substrate.

Figure III.8. ac conductance vs. temperature recorded on ITO/TPD-Alq3/Al device (ac field at 0.1 V level and 1KHz of frequency).

Figure III.9. Analyzed device structures. A cross configuration of electric contacts has been adopted (plate plane capacitors).

Figure III.10. Real part of complex impedance for ITO and LSMO based devices. In the plot are reported also the fitting curves obtained using the equivalent circuits in parallel mode representation [ITO single RC (—– – –), LSMO single RC (– – –) and double RC (———), depicted in the inset].

Figure III.11. Imaginary part of complex impedance for ITO and LSMO based devices and related fitting curves. In the inset a log-log Nyqvist plot is reported.

Figure III.12. Real part of the complex impedance spectra recorded at several fixed temperatures.

Figure III.13. Imaginary part of the complex impedance spectra recorded at several fixed temperatures. In the inset the log-log Nyqvist plot is shown.

Figure III.14. Temperature dependence of R_1 and R_2 parameters extracted for LSMO/Alq3/Al devices using the equivalent circuit in the parallel mode representation; the inset displays the log-log Nyqvist plot (symbols) and the relative fitting curves (solid lines).

Figure III.15. Experimental (symbols) MR temperature dependence compared with the theoretical data (solid line) calculated by multiplying superficial magnetization Msup (dashed line, Ref. [28]) with the normalized interfacial conductance G_{int} (dash dot line).

Figure III.16. P5 chemical structure.

Figure III.17. Typical output (a) and transfer (b) characteristics.

Figure III.18. device layout; on the left, the magnification of the interdigitated fingers together with the specifics of the channel devices are reported.

Figure III.19. (a) AFM image of the 6ML thick P5 film growth at 10Å/sec; (b) transfer characteristics recorded at V_{DS}=-40V by sweeping V_G from +40 V to -40 V. The accumulation of holes is evinced by the increase of current at high negative gate voltage biases.

Figure III.20. C-V measurement performed on P5 based device; the charge accumulation is displayed at high gate voltages by an increase of channel capacitance due to the field effect. The relative saturation indicates that the occurrence of the charge accumulation has been completed.

Figure III.21. Absolute channel capacitance vs. frequency at fixed dc biases (solid symbols) and fitting curves (lines) performed by using the finer TL model (Mod 2 considers also the contact resistances). By increasing the dc gate voltage bias, the dynamics describing the building of the accumulation layer can be monitored. The red arrow indicates the width of the region of charge accumulation.

Figure III.22. Transfer characteristics recorded in vacuum by sweeping the gate voltage from + 40V to - 40 V with V_{DS} fixed at -1V. In the inset the overall channel resistance, equal to 100 KΩ, calculated from the transfer characteristics using the Ohm's law, is reported

Figure III.23. Channel capacitance vs. angular frequency at a gate voltage bias equal to -40 V. The fitting curves (MOD1 and MOD 2) are reported a s solid lines.

Fig.IV.1. Trap states localized near the HOMO and LUMO levels in the context of a typical energetic diagram of organic materials (left) and effect of trap states on the relative density of states (DOS).

Fig.IV.2. a) channel current vs. time at an arbitrary fixed operating point; b) shift in time of transfer characteristics upon stress mechanisms.

Fig.IV.3. Transfer characteristics of a P5-based TFT recorded in air and in vacuum by sweeping the gate voltage in forward scan (black and blue symbols) and backward scan (red and magenta symbols) at a fixed drain voltage (-20V).

Fig.IV.4. Detail of the transfer characteristic for a pentacene based thin-film transistor measured in forward (■) and backward (●) scan in the neighborhood of V_G =-30 V . The gate voltage scan rate is a=1 $V*sec^{-1}$. The extracted differential slope of the transfer characteristics is $\Delta m=2.5*10^{-8}$ Siemens.

Fig.IV.5. Transfer characteristics of pentacene OFET exhibiting hysteresis. They are acquired with V_D=-20 V and gate voltage sweep V_G ranging from $[-V_{max};+V_{max}]$. Different hysteresis curves correspond to gate sweeps with V_{max} increasing from 20 V to 50 V by 5V step. The inset shows the trend of extracted Δm vs V_{max}. Continuous red line is the power law fit Δm $(A/V)=3.5\ (\pm0.7)\cdot10^{-6}\cdot(Vmax\ -17.9(\pm0.7))^{0.75(\pm0.05}$ (V).

Fig.IV.6. (a) Hysteresis parameter Δm vs $I_{D,max}$ extracted from the transfer characteristics in Fig. 2. Best fit (red line) is $\Delta m\approx0.112\ (\pm0.002)\ (V^{-1})\ I_{Dmax}$

(A). (b) differential logarithmic derivative at the turning point vs V_{max}. Best fit (red line) is y≈0.120 (±0.002) (V^{-1}) V_{max} (V).

Fig.IV.7. Differential logarithmic transconductance at the turning point vs. ΔV_{max} for scan rate a equal to 0.1 V*sec^{-1} (■) and 0.01 V*sec^{-1} (●). The red lines denote the fitting curves.

Fig.IV.8. Schematic representation of the three different film growth scenarios.

Fig.IV.9. AFM image and PSDF of a P5 sample growth at 0.03 Å/sec and fixing the substrate temperature at 60°C.

Fig.IV.10. AFM image and PSDF of a P5 sample growth at 0.75 Å/sec and fixing the substrate temperature at 60°C.

Fig.IV.11. AFM image and PSDF of a P5 sample growth at 1.92 Å/sec and fixing the substrate temperature at 60°C.

Fig.IV.12. Correlation length vs. deposition rate (expressed in ML/min) .

Fig.IV.13. Typical transfer characteristics recorded for the sample grown at 0.75 Å/sec. As it is shown, the different test patterns, characterized by the same geometrical factor, show a current with a nearly equal current. Such evidence implies a scarce effect of contact resistances in the measured devices.

Fig.IV.14. Mobility vs. deposition rate for the analyzed samples.

Fig.IV.15. Threshold voltage vs. correlation lengths plot; the red line corresponds to V_{th}=0.

List of tables.

Tab.II.1. Room temperature conductivity and mobility for films measured in planar and transverse configurations.

Tab.II.2. The fitting parameters extracted for the curves displayed in Fig.11. In particular, the value of the parameter A extracted by $\varepsilon_r(\omega)$ curve is in agreement with the value extracted from $\sigma_r(\omega)$.

Tab. III.1. Fitting parameters extracted from the C-V curve reported in Fig. 223 using TL MOD 1 and MOD 2. Here, R_{ch} is the channel resistance, C_i is the interfacial capacitance, R_c is the contact resistance and C_c is the contact capacitance.

Tab.IV.1. Morphologicl and transport parameters extracted by the performed measurements.

List of publications.

1. M.Barra, M.Biasiucci, A.Cassinese P.D'Angelo, and R.Vaglio: "*FIELD EFFECT DEVICES BASED ON STO ($SrTiO_3$) GATE DIELECTRIC FOR THE INVESTIGATION OF CHARGE CARRIER MOBILITY IN MACROMOLECULAR FILMS*"; Macromol. Symp., 2006, 234, 1-6.

2. M. G. Maglione, P. D'Angelo, M. Barra, A. Cassinese, P. Vacca, C. Minarini and A. Rubino: "*ELECTRICAL TRANSPORT PROPERTIES CHARACTERIZATION OF PVK (POLY N-VINYL CARBAZOLE) FOR ELECTROLUMINESCENT DEVICES APPLICATIONS*", Solid State Electronics, 2007, 51, 123-129.

3. P.D'Angelo, M.Barra, S.Guido, G.Tomaiuolo and and A.Cassinese: "*AN ELECTRIC CRITERION TO EVALUATE GLASS TRANSITION TEMPERATURE DIELECTRIC RELAXATION MEASUREMENTS*", Macromolecular Symposia, 2007, 247, 43-49.

4. P. D'Angelo, M. Barra, M. Nicodemi and A. Cassinese: "*PHASE TRANSITIONS AND AGING PHENOMENA IN DIELECTRIC-LIKE POLYMERIC MATERIALS INVESTIGATED BY A.C. MEASUREMENTS*", Journal of Applied Physics, 2007 101, 044910.

5. M. Barra, A.C. Barone, M. Biasiucci, A. Carella, A. Cassinese, P. D'Angelo and A. Rovello: "*DC AND AC ELECTRICAL TRANSPORT PROPERTIES OF REGIOREGULAR POLY[3-(4-ALKOXYPHENYL)-THIOPHENES]*", Journal of Applied Physics, 2007, 102, 093712.

6. A.Castaldo, L.Quercia, G.Di Francia, A.Cassinese and P.D'Angelo: "*AC ELECTRICAL INVESTIGATION OF POLYSILSESQUIPXANIC FILMS USED AS RELATIVE UMIDITY SENSORS*", Journal of Applied Physics, 2008, 103, 054511.

7. M.Barra, A.Cassinese, P.D'Angelo, L.E.Hueso, Y.Q.Zhan and V.Dediu: "*MANGANITE/TRIS (8-HYDROXYQUINOLINE)ALUMINIUM (Alq3) INTERFACES INVESTIGATED BY IMPEDANCE SPECTROSCOPY TECHNIQUE*", Organic Electronics, 2008, 9, 911-915

8. P. D'Angelo, P. Stoliar, T. Cramer, A. Cassinese, F. Zerbetto, F. Biscarini:*" QUANTITATIVE ANALYSIS OF CHARGE CARRIER TRAPPING IN ORGANIC THIN-FILM TRANSISTORS FROM TRANSFER CHARACTERISTICS"*, accepted by Applied Physics A.

List of symbols and abbreviations.

Symbols.

a, gate voltage sweep scan speed

B, magnetic field

C, capacitance

$C_{accum.}$, TFT channel capacitance recorded in accumulation mode

Cc, contact capacitance

$C_{electr.}$, TFT electrode capacitance

c_I, interfacial capacitance

c_{ox}, capacitance of the oxide (gate dielectric)

c', series between c_{ox} and c_I

d, dimensionality

D, electric displacement

e, elementary charge

E, electric field

G, conductance

I_D, drain current or TFT channel current

G_{int}, interfacial conductance

I_D, drain current or TFT channel current

k Boltzmann's constant

K, degree Kelvin

L, TFT channel length

m, mass of the charge carrier

MR_{th}, temperature dependent magnetoresistance

n, number of free charge carriers

N_f, free carrier density

N_{tr}, density of trapped charges

$N(0)$, $N(E_F)$, density of states at Fermi level

p, impulse

P, polarization

r, sheet resistance

r_0, polaron radius

R, electrical resistance

Rc, contact resistance

R_s, series resistance

R_ω, tunneling distance

R(f), real part of the complex impedance

T_c, Curie temperature

T_g, glass transition temperature

T_m, melting temperature

T_{sub}, substrate temperature

v_d, drift velocity

V_D, drain voltage

V_{DS}, source-drain voltage or channel voltage

V_G, gate voltage V_S, source voltage

V_{th}, threshold voltage

X(f), imaginary part of the complex impedance

Y_0, characteristic admittance of the TL

W_{eff}, effective activation energy for the hopping-like charge transfer

W_H, activation energy for the polaron transfer

W, TFT channel width

Z, atomic number

Z, complex impedance

Z_C, contact impedance

Z_L, load impedance

Z_0, characteristic impedance of the TL

α, polarizabilty

β, stretching factor

γ, propagation constant of the TL

γ_i, overlayer-substrate interface

γ_s, substrate-vacuum interface

γ_0, overlayer-vacuum interface

Δm, hysteresis parameter

ΔV_{th}, threshold voltage shift

ε, dielectric permittivity

ε_0, free space permittivity

ε′ or ε_r, dielectric constant

ε″, dielectric loss

ε_∞, dielectric constant for $\omega \rightarrow \infty$.

μ_{int}, intrinsic charge carrier mobility

ν_0, amplitude of the probe signal

ξ, localization length; correlation length

σ, conductivity

σ_{ac}, ac conductivity

σ_{dc}, dc conductivity

$\sigma(T)$, temperature dependent conductivity

τ, characteristic time constant, relaxation time

Φ, deposition rate

Φ_D, pulse-response function of polarization

χ, the dielectric susceptibility

ω, angular frequency

ω_p, plasma frequency

Abbreviations.

ac, alternating current

AFM, Atomic Force Microscope

Ag, silver

Alq_3, Aluminum tris(8-hydroxyquinoline)

α-Si:H, hydrogenated amorphous silicon

BC, bottom contact

CB, Carbon Black

CBH, Correlated Barrier Hopping

CO, carbon monoxide

CuPC, Copper Phtalocyanine

C-V, current voltage

dc, direct current

DMTA, Dynamic Mechanical Thermal Analysis

DOS, density of states

DSC, Differential Scanning Calorimetry

EL, electroluminescence

ETL, Electron Transport Layer

FV, Free Volume

GMR, Giant Magnetoresistance

GSCS, Gas Sensor Characterization System

HF, fluoridric acid

HOMO, Highest Occupied Molecular Level

HTL, Hole Transport Layer

H_2SO_4, sulfuric acid

ITO, indium tin oxide

IR, infrared

IS, Impedance Spectroscopy

I-V, current-voltage

LSMO, lanthanum strontium manganese oxide

LUMO, Lowest Unoccupied Molecular Level

ML, monolayer

MOKE, Magneto-Optical Kerr Effect

MR, Magnetoresistance

OFET, Organic Field Effect devices

OLED, Organic Light Emitting Diode

OLP, Overlapping Large Polaron

OMBD, Organic Molecular Beam Deposition

OSV, Organic Spin Valve

OTFT, organic thin film transistor

OTS, octadecyclltrchlorosilane

PDMS, Polydimethylsiloxane

POSS, organosilsesquioxanes

POT, poly [3-(4-octyloxyphenyl)-thiophenes]

PSDF, Power Spectral Density Fourier

PT, polythiophene

PPD, pulsed plasma enhanced deposition

PVK, Poly-vinilcarbazole

P3HT, poly [3-hexyl-thiophene]

P5, Pentacene

QMT, Quantum Mechanical Tunneling

RFID, radiofrequency identification tag

SCL, Space Charged Limited

Si_3N_4, silicon nitride

SiO_2, silicon dioxide

SP, small polaron

STO, strontium titanate

TFL, Trap Filling Limited

THF, tetrahydrofuran

TL, transmission line

TPD, N,N'-Bis(3-methylphenyl)-N,N'-diphenylbenzidine

T6, Sexithiophene

UDR, Universal Dielectric Response

UPS, Ultraviolet Photoemission Spectroscopy

UV-VIS, ultraviolet-visible spectra VHR, Variable Hopping Range

$VO(acac)_2$, vanadyl acetonate

XPS, X-Ray Photoemission Spectroscopy

Introduction.

Organic electronic devices have gained a noticeably interest in the scientific community tanks to the simultaneous participation of the peculiar mechanical properties of organics, the easiness of device manufacturing and the cheapness of the end product. At the present time, the commercial impact guaranteed by the optoelectronic devices is more and more increased by the feasibility of highly performing light emitting devices (OLEDs). Moreover, also the application of organics in the field of sensing, favored by their capability of interacting chemically and mechanically with external factors, seems to be ready for the commercial launch.

Actually, however, great efforts have to be made in order to develop the driving circuits such as switches and memories, required for implementing a fully flexible, plastic electronics. In particular, the interest towards field effect devices (OFETs), spintronic devices (Spin Valves, SPs) and, in general, memories based on organic materials, requires the implementation of some analytical tools in order to furnish an exhaustive comprehension of both the materials and devices features. In fact, even if static electrical measurements represent a basic tool for the analysis of the properties showed by both conventional and organic semiconducting materials, and related devices, their employment for the analysis of organics is limited by the intrinsic impossibility of investigating thoroughly all those aspects regarding their physical and mechanical properties. Of course, dc measurements show some limitations also in the analysis of the organic based devices. In this respect, device features cannot be essentially discriminated by employing static fields. In particular, the application of static external electric fields lacks in the possibility of probing the local

contributions to the observed overall properties showed by organics and devices, such as for example:

- the limiting charge trapping phenomena due to extrinsic, localized defects and their intimate effects on the overall performances of organic thin film transistors (OTFTs);
- the trapping produced by the intrinsic defects due to the structural features of the active organic materials, which is again a limiting factor in terms of OTFTs performances;
- the contribution of device sections such as the very relevant manganite/organic interfaces in organic spintronic devices and the limiting effects produced by the peculiar arising of interface dipoles located at metal/organic heterojunctions;
- the phase transitions showed by organics, with particular reference to the glass transition, a peculiar property for a wide class of organics;
- the effects of phase transitions on device working mechanisms.

With the aim of overcoming such limitations, standard ac electrical techniques (able to investigate both the interfacial and bulk properties) have been borrowed by the world of inorganic semiconductors in order to evidence all the aspects regarding the features of the bare organic semiconductors and the devices based on them. This fundamental step has been favored by the standards of quality reached recently for the organic films, which in the last years has become better and better.

In this respect, it is worth to mention that Capacitance-Voltage (C-V) measurements have been extensively applied to conventional TFTs, but otherwise it is not obvious their employment in the context of devices based on organics such as pentacene, a well known semiconducting oligomer characterized by high values of field effect mobility. In this case, their importance is maybe major, since this kind of measurement allows to discriminate the effects of contact resistances, which generally are of

relevant importance in the case of organic TFTs. Moreover, another typical ac analysis, e.g. the broadband Impedance Spectroscopy (IS), furnishes the possibility of shedding light on the role of some typical properties of organic materials. In particular, IS is able to clarify the microscopic basic conduction mechanisms of polymeric semiconductors in the context of some existing models (such as happens for the promising polythiophenes), and the peculiar glass transition showed by rubber organics. Moreover, as it has been already indicated above, IS plays a crucial role also for the analysis of device limiting factors and working mechanisms. In particular, as an example, the great impact of IS on OSVs operation properties is certified by the application of the well known RC parallel representation, whereas the arising of some further contributions to the analysis of devices via equivalent circuital elements well describes the magnetoresistive properties of manganite/organic (LSMO/Alq_3) interface

In this context, the thesis work proposal regards the application of both the above mentioned standard protocols of dynamic ac electrical measurements for the study of materials and related devices properties, and a novel dynamic technique employed for the analysis of trapping phenomena in a typical organic-based TFT. In particular, the last technique of measurement is carried out through the study of hysteretic phenomena in the characteristic curves showed by such device.

The organization of the thesis contents follows.

The first chapter is dedicated to the collection of the standard tools of electrical characterization employed for the study of materials and devices properties. The description of such techniques is performed motivating their strong impact on organic electronics through some argumentations reported at the state of art.

In the second chapter the application of the framework introduced in the previous chapter is extended to the case of two types of organics, that is conducting materials and dielectrics, in order to describe the microscopic

features of charge transport in the first class of materials here mentioned and the peculiar mechanical properties showed by a wide class of both the classes above indicated.

The third chapter deals with the application of the ac measurements in the case of organic-based devices, in order to study several features characterizing them. First of all, ac measurements will be employed to evidence the effects of the device bulk properties on its working mechanisms, with a special reference to the role of glass transition in terms of both operation features and degradation properties. The IS technique will be developed also with the sake of framing the crucial role of the interface between the injecting electrodes and the organic layers in spintronic devices. Moreover, the standard C-V technique will be employed for the evaluation of static and dynamic parameters of OTFTs, such as the very important contact resistances (which often can affect dramatically the device response) and the maximum device operation frequency (which plays a major role in the context of several important applications, such as rectifying devices or radio frequency identification tags, RFIDs), respectively.

The fourth chapter will be manly addressed to the dynamic study of stress phenomena in OTFTs (active layer constituted by pentacene). The study will be based on the analysis of the charge trapping on very short time scales with respect those generally involved in trapping mechanisms. The analysis will be in particular focused on the effects produced by charge trapping on the hysteretic device response. Moreover, as a working cause on which the development of the present work has to be orientated, the morphological features of device active layers will be checked, since their possible effect on the hysteretic behavior of transfer characteristics can be argued from the analysis of such curves.

Chapter I

Dynamic electrical measurement techniques employed in materials and devices characterization.

1.1) Organic Electronics and role of the electrical measurements.

Since the last four decades of the 21st Century, a wide class of organic materials, such as plastics, conductive polymers or small molecular compounds with a peculiar chemical property, able to confer them semiconducting properties (i.e. the π-conjugation), has gained the interest of many researcher operating in the field of condensed matter. At the beginning, organic semiconductors were not suddenly looked at as good candidate for the manufacturing of organic-based electronic devices. In fact, the interest in such class of organics was confined only to some basic studies, since plastics, which generally are not conductive materials, did not guarantee efficient performances in terms of device applications.

Historically, the first indication of the fascinating properties of such materials was given by the observation of an important property showed by PVK, Poly-vinilcarbazole. In detail, photoconductivity and emission of light in the visible spectrum (blue region) upon optical and electrical absorption were discovered in PVK by Hoegel during the sixties. After, for many time few isolated studies on the conduction mechanisms and device applications were performed. In particular, the conduction in some polymeric materials was explained on the basis of the model introduced by Mott for describing the charge carrier transport in disordered materials[1], while a prototype of a polymer-based electronic switch was developed[2]. The turning point toward the interest in organics as promising materials for the development of an efficient electronics fell especially in between the last seventies and the early eighties, when both the discovery of highly conductive polymers made by Heeger, Mac Diarmid and Shirakawa (culminated with the awarding of Nobel Prize for Chemistry in 2000)[3] and the manufacture of a prototype of light emitting diode, due to Friend, Burroughes and Bradley[4], followed by the development of the first efficient

prototypes of field effect transistors occurred in the late eighties[5,6], opened the way toward the born of 'organic electronics'.

From now on, the scientific community will assist to an exponentially growing number of researches focused mainly on some important aspects:

1) the synthesis of novel materials with the desired properties, conferred by operating a physical-chemical tailoring of materials properties in phase of synthesis, but also by acting on deposition parameters in phase of thin film manufacturing;

2) the manufacturing of devices with different geometries (sometimes aimed to improve device performances, other times with the purpose of obtaining multifunctional applications), being the device architecture crucial for exploiting selectively the desired properties of organics;

3) the introduction of novel experimental approaches in which the compatibility of organics with bio-molecules can be exploited for promising applications[7];

4) the attempt of exploiting the strong commercial impact offered by organics, in the context of low-cost, flexible and large area applications with not particularly demanding performances, favored by the cheapness of some deposition techniques.

All these aspects are indicators about the need of conferring a strong interdisciplinary character to the research in the field of organic electronics (which maybe represents the most fitting example of Converging Technologies (CTs)), since the convergence of the know-how belonging to different scientific educations represents the basis on which CTs found.

It is clear that all the topics stated above are deeply linked to the features of organic materials. In particular, the term 'organic electronics' is mainly due to the fact that the materials employed for the manufacturing of light, flexible and low cost devices, are carbon-based compounds with a more or less complex chemical structure, just like the living molecules. For this reason, organics experience aging phenomena which provoke a strong

degradation of their physical and mechanical properties. This latter aspect, together with an intrinsic difficulty consisting in a scarce reproducibility in device response, justifies the strong efforts required for optimizing the conventional applications allowed by organics (in view of their commercial launch) and the noticeably workforce lavished in the research of novel applications. Therefore, the electrical measurements performed via dc and ac techniques on organic materials and related devices are essential for characterizing both the materials and devices properties. In particular, electric measurements performed by using static fields (dc measurements) are required for the understanding of the macroscopic features regarding the charge transport in carbon based semiconducting aggregates composed by single organic molecules, short (oligomers) and long (polymers) chains, whereas the complexity of these aggregates culminates in a long range structural disorder affecting dramatically the charge transport in the resulting bulk materials. On the contrary, ac measurements are an alternative and very powerful tool leading to the comprehension of materials microscopic features, giving also a deep insight into the understanding of device properties and limiting factors, thanks to the discriminating character typical of such techniques. So, as a consequence, alternative dynamic techniques based on the employment of varying fields (ac measurements) are required for the comprehension of organic devices, with the further aim of governing their overall response. The main request for such techniques is the capability of separating each individual effect concurring to the overall device response from the others, allowing in this way an efficient understanding of any aspect exploitable for bettering device operation and for introducing novel possible applications.

1.2) Electrical dynamic characterization techniques of organic materials and related devices: from static dc measurements to dynamic ac measurements.

The fundamentals of organic electronics found obviously on the electrical measurement techniques, not only because of the practical need of determining the device operation or the necessary requirement of testing the device efficiency, but also for the aim to go into the details of basic working mechanisms in both the materials and related devices. In fact, the development of technology relies generally on the exploitation of the analytical aspects related to all those practical tools employed for putting the ultimate applications into practice. This is done basically in order to guarantee a deep understanding of the basic fundamentals within the same technology, as clearly the implementation of the reliable applications is in needs of the comprehension and the subsequent control of the material properties.

The electrical characterization of materials and devices is carried out following two different protocols of electrical measurements. Dc measurements are performed by recording the electrical response of materials and devices under the effect of static electric fields; dynamic ac measurements regard instead the response of capacitive device structures under the effect of time varying electric fields. In particular, the response upon time varying fields (more precisely the Impedance Spectroscopy, IS) goes beyond the simple comprehension of the global behavior of materials and devices, as it represents a powerful tool for the investigation of local effects concurring to the overall response.

Since it is clear that the paramount importance of electrical measurement techniques represents a predominant demand both in the field of the basic research on materials and the actual device applications, a general description of preliminary dc electrical measurements and a detailed

description of the technique representing the central core of the thesis, that is ac measurements, together with some experimental results at the state of art (which can be considered as a milestone of materials and devices characterization), are needed.

1.2.a) Static electrical characterization: fundaments, utility and limitations.

As stated above, dc measurements represent the first step to do for reaching an exhaustive comprehension of the overall conducting properties showed by organic semiconducting materials. In fact, the employment of dc measurements furnishes a criterion for the study of the intrinsic conducting parameters, such as the conductance and the thermal activation energy of conduction, being the second one a typical parameter in the case of semiconducting-like charge transport.

Technical current-voltage (IV) measurements are performed by recording the current flow into the bulk of the analyzed organic materials, deposited in form of thin films, in function of the applied static electric fields. The typical structures employed for this purpose are metal/organic/metal hybrid devices, where the charge injection inside the material is favored by the metallic electrodes. Generally, the deposition of metal electrodes is performed by thermal evaporation technique, in order to avoid damages to the surfaces of the fragile organics eventually provoked by the most invasive sputter deposition techniques.

The main request for the basic analysis of the electric response is the definition of the effective conducting channel, that is a defined geometry for the injecting electrodes deposited on films in which the thickness is known. In fact, the device geometrical factor allows to extrapolate from theoretical models some intrinsic conduction parameters regardless of the geometry of the measured device structures. As regards the comprehension

of the features of conduction contained in the overall electrical response, generally I-V measurements are performed in controlled temperature and environmental pressure conditions. In this way in fact it is possible to check the influence of thermally activated mechanisms on the semiconducting properties showed by organics, but also the possible effect of environmental factors such as the relative humidity or the oxygen contained in air. In this respect, it is known that the electric response is strongly affected by environmental conditions, since the degradation of materials provoked by some extrinsic factors affecting the electric measurements reflects itself in the presence of humidity and oxidative reactions induced by air, both these effects manifesting in a scarce reproducibility in the measurements[8]. Moreover, the control of external temperature is of paramount importance, as in the case of amorphous semiconductors the conducting properties are strongly related to some theoretical models in which the temperature-dependent conducting parameters are extracted in the context of hopping or tunneling phenomena. As regards these models, a special reference to the Variable Hopping Range transport, introduced by Mott for describing the low temperature conduction in strongly disordered systems with localized states[9], is opportune, since the hopping of charge carriers among non equally spaced adjacent localized states seem to be universally accepted as the main mechanism responsible for charge transport in disordered materials[10,11]. In this case σ(T), i.e. the temperature dependent behavior of conductivity, can be described as:

$$\sigma(T) = \sigma_0 \exp\left[-\left(\frac{T_0}{T} \right)^{\frac{1}{d+1}} \right], \qquad (1)$$

where d is the dimensionality of the system (for bulks d=3) and T_0 is defined by exploiting the form of the average energy level spacing in a volume ξ^3:

$$kT_0 = \frac{1}{N(0)\xi^3}, \quad (2)$$

where k is the Boltzmann constant, N(0) is the density of states at the Fermi level and ξ is the localization length[9].

Additionally, a strong anisotropic character of charge conduction is experienced in organic semiconductors due to their amorphous structure[12], so both planar (i.e. electrodes deposited on the top of the organic thin film, or vice versa) and vertical geometries of the injecting electrodes (i.e. organic sandwiched between metallic electrodes) can be employed.

The actual greatest limiting factor of dc measurements lies generally in the global view about the nature of conduction mechanisms they solely can offer, giving them only a general depiction of the overall charge transport produced by the simultaneous contribution of the involved possible local conduction mechanisms. In fact, the study of the local microscopic features of charge transport in organics is not allowed by dc measurements. Moreover, dc measurements on devices are affected by the superposition of several mechanisms concurring at the same time to the overall response. In fact, for example, even if it is true that the output characteristics and the transfer characteristics (i.e. the typical responses recorded in the case of organic thin film transistors, OTFTs) are indicators of the device operation performances and furnish a tool for the evaluation of device parameters, on the other hand it is also true that they usually display the simultaneous effect of:

- hybrid metal/organic injecting heterojunction;
- the intrinsic charge transport;
- the contact resistances at the metal/organic interface;
- the charge trapping at the gate dielectric/organic interface (bias stress phenomena);
- the eventual presence of thermal drifts (which can be generated by local heating as a consequence of the application of high static

fields, generally greater than 10^4 V*cm^{-1} in the case of conventional device structures).

Of course, a deeper understanding of the individual weight of each aspect concurring at the overall device response requires that all these topics need to be probed separately. In this respect, the most important factor limiting the device response is usually constituted by the metal/organic interface. In fact, above all in the case of electroluminescent devices, it has been widely reported the effect of the metal/organic interface on the efficiency of charge injection[13,14]. Physically, the energetic scheme of such junction predicts a strong mismatching between the metal work function Φ and the hole and electron conduction levels [HOMO (Highest Occupied Molecular Level) and LUMO (Lowest Unoccupied Molecular Level), respectively] or alternatively their energetic position (electron affinity and ionization potential, respectively). The magnitude of this mismatching is dramatic for the organics typically employed as semiconductors, being the energy barrier for charge injection usually about 1eV. For this reason a capacitive effect limiting the ohmic charge injection arises at the interface when the thermal equilibrium conditions are reached, i.e. when the alignment of the work function and the Fermi level of the materials is reached after the contact has been carried out.

This occurrence produces a significant effect on the device electric response, that is the non-ohmic electric contact causes a non-linear and asymmetrical current flow upon the application of a static field, depending on the height of the injection barrier. Moreover, the interface produces also other significant phenomena, such as the arising of interfacial dipoles[15] or the band bending at the interfaces[16].

The phenomenology of the non-ohmic metal/organic junctions is investigated by recurring to some models developed for the study of conventional semiconductors, such as the Fowler-Nordheim model[17], describing the tunneling of injected carriers through the above described

energy barrier, or the Richardson-Schottky thermal activated charge injection through the same barrier[18]. Moreover, the super-linearity showed by the bulk electric currents can be related to the arising of Space Charged Limited (SCL) phenomena at higher electric fields[19], also in presence of a discrete trapping level (in this case, the non linearity can be ascribed to typical Trap Filling Limited phenomena, TFL, describing generally the progressive population of shallow trap states during the application of an external voltage[20]). Although these phenomena are very useful for the study of some intrinsic parameters (since the analytical expression of the related current density contains information on conducting parameters such as the bulk intrinsic charge carrier mobility and the dielectric permittivity), a more detailed investigation of the intrinsic bulk microscopic conduction mechanisms and the dielectric nature of organics, but also a deep analysis of the role played by interfaces, is necessarily based on more sophisticated techniques, which allow the local probing of material and device properties. This task is well accomplished by the ac dynamic electrical measurements.

1.2.b) Standard dynamic electrical measurements: Impedance Spectroscopy technique(IS).

Impedance Spectroscopy is a versatile tool for the study of materials and devices[21,22,23,24]. Basically, IS probes the relaxation processes induced by the application of an alternate electric field, varying in a wide window of frequencies. This means that IS is very sensitive to relaxation processes in an extremely wide range of characteristic times (10^{5}-10^{-12} ^{s}); in particular, depending on the intimate structure of materials, on their phase and on their dielectric properties, it is possible to distinguish between Broadband and Time Domain Dielectric Spectroscopy (Fig. 1). In general, the

relaxation of condensed matter is waited in a window of frequencies ranging from fractions of Hz to some MHz.

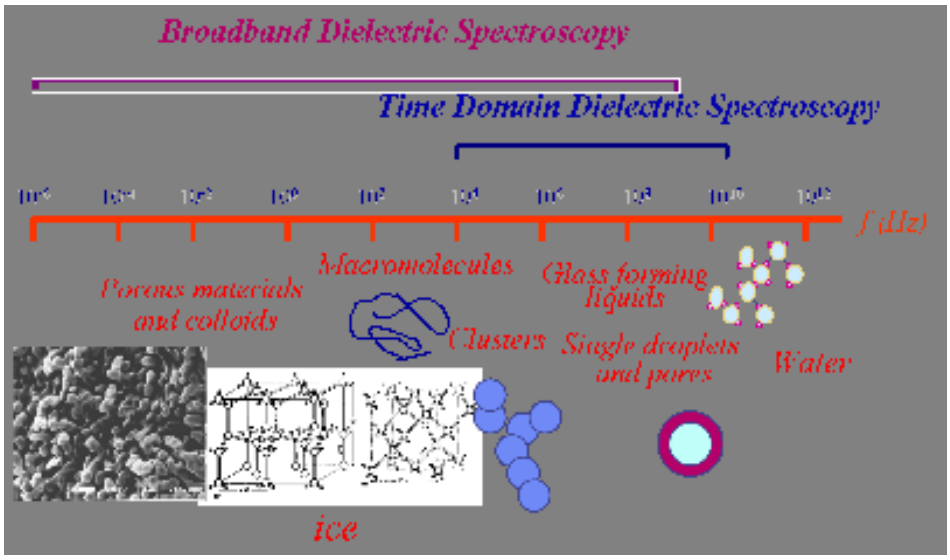

Fig. I.1: Broadband dielectric spectroscopy; the frequency windows in which the systems indicated (such as porous materials or glasses) interact with the external varying field are approximately indicated.

In detail, when a material is immersed in a varying field, it experiences an induced dipole moment. The dipole moment arises because the centers of gravity of the positive and negative charge distributions inside the material do not coincide. This dipole moment can be induced by the external fields (induced dipole moment), but in many cases it can be an intrinsic property of molecules with a non-symmetric charge distribution (permanent dipole moment for polar molecules). In both cases, the material can be viewed as a continuum treatable as a dipole density of matter. So the effect of the external electric field **E** in which the material is immersed consists in the arising of a non-null overall distribution of charge due to the field produced inside the matter; on its turn this field, which of course is the source of the distribution of charge, can be defined by means of the dielectric displacement **D**. Therefore, it is clear that inside the matter the vector **E** is 'scaled' by a quantity depending on the arising of a non-null

dipole moment **P** (polarization) generated by diversely charged portions of the material:

$$\boldsymbol{D} - \boldsymbol{E} = 4\pi\boldsymbol{P} \tag{3}$$

Since **P** is proportional to the strength of **E**, it is possible to introduce a factor χ, the dielectric susceptibility, such as:

$$\boldsymbol{P} = \chi\boldsymbol{E} \tag{4}$$

Moreover, in this context another important parameter, the dielectric permittivity ε, can be introduced:

$$\boldsymbol{D} = \boldsymbol{E} + 4\pi\boldsymbol{P} = (1 + 4\pi\chi)\boldsymbol{E} = \varepsilon\boldsymbol{E} \tag{5}$$

Clearly, the knowledge of the effect produced on the matter by an external field **E** depends strictly on the knowledge of the permittivity, or equivalently the susceptibility χ. Generally ε depends on the frequency of applied field, the temperature, the density (or the pressure) and the chemical composition of the system[25].

If the system experiences the effect of a time dependent external electric field, applied at a defined time t', the electric displacement at the time t can be written as:

$$\boldsymbol{D}(t) = \varepsilon \int_{-\infty}^{t} \boldsymbol{E}(t')\phi_D(t - t')dt' \tag{6}$$

where Φ_D is the pulse-response function of polarization (obeying to the casuality principle). Performing the Laplace transform of eq. (6), taking into account the deconvolution theorem, the vector **D** can be written in frequency domain as:

$$D^*(\omega) = \varepsilon^*(\omega)E^*(\omega), \tag{7}$$

where:

$$\varepsilon^*(s) = \varepsilon_s \int_0^{\infty} \phi_D(t)\exp(-st)dt = \varepsilon_s L[\phi_D(t)] \tag{8}$$

A more convenient form of the eq. (8) is given by:

$$\varepsilon^*(i\omega) = \varepsilon_\infty + (\varepsilon_s - \varepsilon_\infty)L[\phi_p^{or}(t)] \tag{9}$$

Eq. (9) defines a function, analytical in the upper half plane, named complex dielectric permittivity ε(ω):

$$\varepsilon^*(\omega) = \varepsilon'(\omega) - i\varepsilon''(\omega) \tag{10}$$

Both the real and imaginary part of this response function, that is ε′ and ε″, are physical observables that, due to the principle of casuality, can be linked by means of a Hilbert transform, giving thus the well known Kramers-Kronig relations[26,27]:

$$\varepsilon'(\omega) = \varepsilon_\infty + \left(\frac{2}{\pi}\right)\int_0^\infty \frac{x\varepsilon''(x)}{x^2-\omega^2}dx \;\; ; \;\; \varepsilon''(\omega) = \left(\frac{2\omega}{\pi}\right)\int_0^\infty \frac{\varepsilon'(x)}{x^2-\omega^2}dx \,. \quad (11)$$

For the ideal physical case of a non interacting population of dipoles, the relaxation of all these dipoles experiencing an alternating external field occurs in unison, that is it is characterized with by a single relaxation time τ. In this case, ε′ and ε″ are expressed as:

$$\varepsilon'(\omega) = \varepsilon_\infty + \frac{\varepsilon_s - \varepsilon_\infty}{1+\omega^2\tau^2} \;\; ; \;\; \varepsilon''(\omega) = \frac{(\varepsilon_s - \varepsilon_\infty)\omega\tau}{1+\omega^2\tau^2} \,, \quad (12)$$

also known as Debye's formulas. For a large number of condensed systems Debye's formulas in frequency domain give an adequate description about the behavior of the orientation of polarization under the effect of **E**, even if for many other systems serious deviations from these formulas occur. Differently to what one could deduce in a first time, these formulas do not contain information exclusively on dielectric properties of the matter. In fact, in first approximation, in the context of an equivalent circuit representation, a system given by an actual material sandwiched between two electrodes (i.e. a capacitor filled with the referential material) do not constitutes an ideal case, since a perfect dielectric is just a schematic representation. So, as represented in Fig. 2, the actual system can be viewed in the parallel mode RC representation as a parallel between a capacitance C and a conductance G (resistance R), the latter element describing the losses through the material.

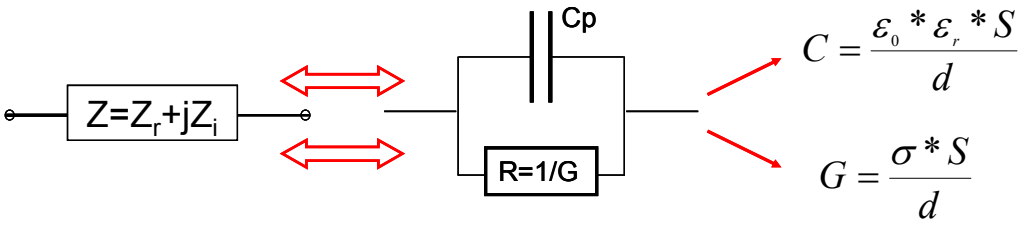

Fig. I.2: Parallel Mode Representation; the complex impedance of the system is given by a parallel between a capacitor (imaginary part of Z; Z_i) and a resistance (real part of Z; Z_R), where the capacitor contains information on the permittivity (real part of the complex dielectric function) while the resistance expressing the losses through the material gives information about the ac conductivity σ_{ac} (linked to ε″, the imaginary part of the complex dielectric function).

Experimentally, one probes the total complex impedance by measuring the couple C,G, where C is linked to the dielectric permittivity ε′ while G is linked to ε″ (ε″ ~ σ_{ac}/ω, where σ_{ac} is the real part of ac conductivity[28]) (Fig. 2). Then, it is clear that ε″ is intimately correlated to the electrical current flowing through the material, so in principle its experimental behavior is the mirror of microscopic mechanisms governing the charge conduction inside the considered matter. So, by probing the relaxation effects into the material via ac measurements, it is possible to study the dynamics of all the microscopic processes occurring in it. In particular, in the case of organic materials, which are characterized by a distribution of relaxation times due to their amorphous nature, IS technique can be employed for studying the dynamics of both conduction mechanisms and structural variations (induced by possible phase transitions) in terms of their peculiar contribution to the observed overall relaxation.

Of course, the technique can be employed also for testing device properties, both by applying an ac field and by superimposing to it a dc bias voltage. In fact, it is possible to monitor the overall relaxation process in a device and to ascribe each observed relaxation peak to the different device parts. In this respect, by varying the frequency of the external field in a wide window, the device can be viewed as a more complex equivalent

circuit. In the simplest representations, depending on several aspects (such as the nature of the employed materials), a metallic resistance, a series between a metallic resistance and a capacitor (employed in the case of strong charge accumulation at interfaces or in the case of SCL phenomena at high dc bias) or a series between a metallic resistance and an RC parallel can be employed, all these contributions simulating the injecting contacts. Similarly, the bulk can be represented in the parallel mode representation as one or more RC parallel circuits in series (above all in the case of organic heterojunctions) (Fig. 3).

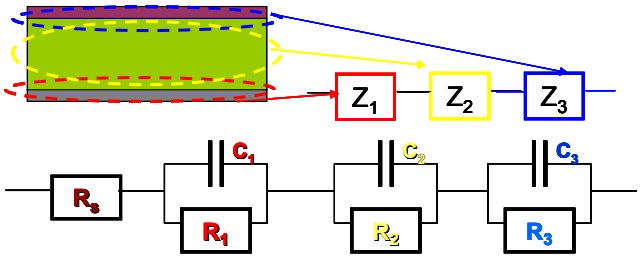

$$\mathrm{Re}(Z_i) = \frac{R_i}{1+(\omega R_i C_i)^2} \qquad -\mathrm{Im}(Z_i) = \frac{\omega R_i^2 C_i}{1+(\omega R_i C_i)^2}$$

Fig. I.3: Parallel mode representation in the case of a basic device structure (typically, a metal/organic/metal heterojunction).

1.2.c) Debye model vs. Universal Dielectric Response (UDR) model.

The ac conductivity of materials can be studied using the response function introduced in section 1.2.b). As it has been already stated during the introduction of complex dielectric permittivity, the ideal case of non interacting dipoles can be described as a process characterized by a single relaxation time τ. The Debye's formulas allow to describe experimentally such processes. But, if we consider a conductive crystalline material, the complex dielectric permittivity ε(ω) can be simply generalized by introducing a charge density accounting for the conduction phenomena into the material. In this case, without entering into details of calculation, the expression of the generalized complex permittivity becomes:

$$\varepsilon(\omega) = 1 + 4\pi\chi(\omega) - \frac{4\pi}{i\omega}\sigma(\omega). \tag{13}$$

In this respect, considering the band-like transport in crystalline metals described by the Drude model, it is possible to explicit the expression of the ac conductivity in eq. (13). In fact, according to this model, metallic charge transport can be described as the motion of charge carriers under the effect of an external field in a viscous medium, simulating in this way the electron-phonon interaction, i.e. the collisions between electrons and the atomic nuclei in the lattice positions. The equation describing the dynamics of carriers in metals is then:

$$\frac{dp}{dt} = -\frac{p}{\tau} - eE(t), \tag{14}$$

where p is the impulse of the charge carrier (electrons), τ is the characteristic time between two consecutive collisions and E is the external field. By considering the eq.(14) in the frequency domain one obtains:

$$\tilde{p}(\omega) = \frac{-e\tilde{E}(\omega)}{\frac{1}{\tau} - i\omega}. \tag{15}$$

Since the Drude model predicts that the local form of Oh m's law can be written as $J=\sigma E=-nev_d$, where J is the current density, σ is the conductivity, v_d is the drift velocity of charge carriers and n is the number of free charge carriers, it is simple to verify that the Fourier transform of such expression gives:

$$\tilde{J}(\omega) = \tilde{\sigma}(\omega)\tilde{E}(\omega) = -\frac{\tilde{p}(\omega)}{m}ne = \frac{e^2 n}{m\left(\frac{1}{\tau} - i\omega\right)}\tilde{E}(\omega), \tag{16}$$

that is:

$$\tilde{\sigma}(\omega) = \frac{e^2 n}{m\left(\frac{1}{\tau} - i\omega\right)}, \tag{17}$$

where m is the mass of the charge carrier. In this case, the ac conductivity is expressed by the eq.(17). The ac conductivity in frequency domain is then a complex quantity. Measuring the ac conductivity in a metal, a relaxation phenomenon produced in the material by the external varying electric field is expected at a certain frequency.

As far as this relaxation process in crystalline conductors is concerned, hypothesizing that $\chi(\omega)\sim 0$, the dielectric constant in this case can be written as:

$$\varepsilon(\omega) = 1 - \frac{4\pi}{\omega i}\frac{e^2 n}{m\left(\frac{1}{\tau} - i\omega\right)}\left[= \varepsilon_0 + \frac{i\sigma(\omega)}{\omega}\right]. \qquad (18)$$

Splitting eq.(18) into its real and imaginary parts:

$$\begin{aligned} \mathrm{Re}[\varepsilon(\omega)] &= \varepsilon'(\omega) = 1 - \frac{\omega_p^2 \tau}{1+\omega^2\tau^2}; \\ \mathrm{Im}[\varepsilon(\omega)] &= \varepsilon''(\omega) = \frac{\omega_p^2 \tau}{\omega(1+\omega^2\tau^2)} \end{aligned} \quad , \qquad (19)$$

where ω_p is the plasma frequency, given by:

$$\omega_p = \sqrt{\frac{ne^2}{\varepsilon_0 m}} \ . \qquad (20)$$

The eq.(19) describes a process characterized by a single relaxation time, τ, which can be strictly correlated to a Debye-like response. In particular, since this relaxation occurs in unison, a metal immersed in a time varying field experiences a collective oscillation of charge density inside the material with a characteristic frequency ω_p (Eq. (20)).

Of course all these topics are valid for metals whit a band-like transport arisen from the long range crystalline order. For these systems the Drude model describes in an excellent way the charge conduction upon the action of external fields, while at the same time a closely ideal Debye response is

suitable for the description of relaxation phenomena occurred upon the action of a varying field.

The case of organic materials is firmly different from the above described , not only because the conduction in organics shows a semiconducting behavior, but also because another requirement, that is the long range order, fails. In fact, in a time-honored review article[29], Jonscher demonstrated that the ac response of disordered matter (for example glasses, pure dielectrics, ionic conductors, semiconducting ceramics and amorphous organic semiconductors) to electromagnetic fields in a wide frequency region, starting from a typical quasi-dc behavior up to the GHz, follows the so-called ‘‘universal dielectric response’’ (UDR), showing up as a sublinear power law in the frequency-dependent conductivity σ(ω) (with s<1, Fig.4):

$$\sigma_{ac} = \sigma(\omega) = \sigma(0) + A\omega^{s}, \qquad (21)$$

where σ(0) represents the dc conductivity, generally separated from the ac contribution (even if this one is not related to relaxation phenomena, as happens for some materials), while A, weakly frequency dependent, is the constant phase element that shows dispersion of conductivity and dielectric properties of the filling material.

The universality of the power law behavior showed by ac conductivity suggests the dominant role of many-body interactions, since such behavior departs from the concept of independent non-interacting polarizing entities and replaces it with interacting systems in which varying degrees of interaction in lead to a deviation from the Debye model.

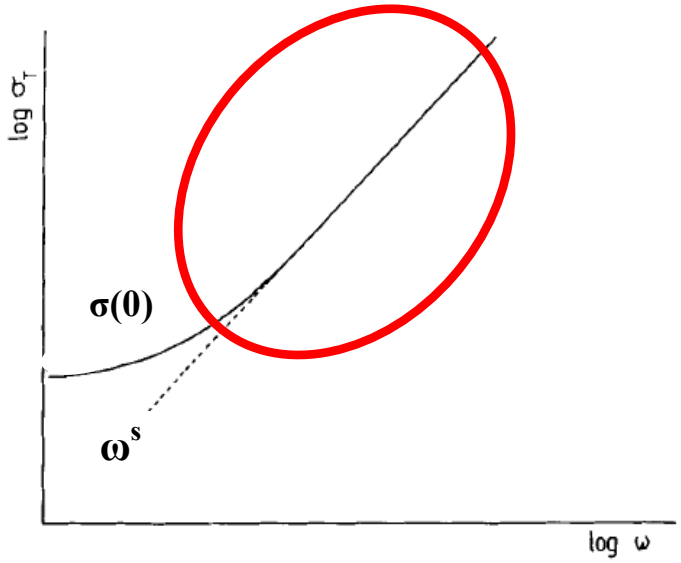

Fig. I.4: UDR behavior of ac conductivity described by eq. (21). The low frequency contribution is given by a dc behavior, while the red-circled behavior describes the power-law dependence at higher frequencies.

In this respect, the power law behavior can found its essence on the local effect of charge conduction in disordered solids, since charge transport is dominated by hopping or tunneling between a couple of localized states where a distribution of 'hopping distances', i.e. the distances between two adjacent states, has to be considered (VHR, Variable Hopping Range)[30]. So, the mutual interaction between polarizing entities suggests that a Debye-like response with a distribution of relaxation times is more suitable for describing the dynamic process of the charge motion in disordered materials.

Experimentally, thanks to the casuality principle (Kramers-Kronig relations) from the ac conductivity σ_{ac} described in (21) (linked to the imaginary part of dielectric function: $\varepsilon'' \sim \sigma_{ac}/\omega$) it is possible to extract the frequency dependent behavior of the dielectric constant as:

$$\varepsilon_r(\omega) = \varepsilon'(\omega) = \varepsilon_\infty + \frac{A}{\varepsilon_0}\tan\left(\frac{\pi s}{2}\right)\omega^{s-1}, \qquad (22)$$

where ε_∞ is the dielectric constant for $\omega \to \infty$.

Looking at the eq.(22) it turns out that the power law index (s-1) describing the frequency dependent behavior of the dielectric constant is the

complement to the unity of the power law in ac conductivity, described by the index s.

So, eq. (21) and eq. (22) describe the universal response of organic materials, both conductive and dielectrics, in terms of the simultaneous ac conduction and dielectric response capture. The analysis of conducting materials is performed by studying essentially the ac behavior of conductivity, while the dielectric nature of organics is reflected in the frequency dependent permittivity. In particular, as state by Jonscher, the adimensional index s in conducting disordered materials varies generally in the range of values 0.6-0.8, while for highly disordered dielectrics is close to 1.

Of course, the experimental measurements are performed in the equivalent circuit representation (RC parallel mode) by recording the capacitance C (that is ε', or equivalently ε_r) and the conductance G (that is ε'', or equivalently σ_{ac}).

For the sake of clearness, in the next sections the sense of UDR model will be discussed by framing it into the context of the state of art, while the employment of IS technique in the context of devices characterization, with particular reference to thin film transistors, will be discussed in terms of a powerful model introduced recently in literature.

1.2.d) ac measurements on amorphous materials.

Ac conductivity measured on disordered materials follows the power law behavior predicted by eq. (21), where generally the dc contribution can be separated from the frequency dependent one if dc conduction is band-like or if the states contributing to ac conduction do not constitute a percolation path contributing to the dc transport. Besides the origin of the frequency dependence of ac conductivity in organics, ascribable to the presence of a distribution of relaxation times as a consequence of hopping mechanisms

or phonon assisted through the barrier separating two equilibrium states (pair approximation, according to which only a couple of states contribute to each individual relaxation and the overall response can be viewed as the summation over the total number of pairs)[30], the UDR model reveals the dominating microscopic charge transport mechanisms in amorphous materials upon testing via ac measurements.

In this respect, many transport phenomena such as Quantum Mechanical Tunneling (QMT) like electron tunneling (proposed in the case of amorphous semiconductors by Austin and Mott[31]) and tunneling of small polaron (SP)[32], or hopping mechanisms such as Correlated Barrier Hopping of electrons (CBH)[33], have been considered as charge transport mechanisms in amorphous materials.

In general, as regards the tunneling phenomena, if the electronic relaxation represents the origin of dielectric losses, QMT can be set at the basis of charge transfer mechanism. In this case, the real part of σ(ω) is given by[30]:

$$\sigma = \frac{C' e^2 kT}{\alpha} N^2\left(E_F\right)\omega R_\omega^4, \tag{23}$$

where C' is a constant, e the elementary charge, K the Boltzmann's constant, α is the polarizabilty of the couple of states involved in tunneling mechanism, R_ω is their distance at a given frequency ω and $N(E_F)$ is the density of states at Fermi level. In this case, the index s describing the power law-like ac conductivity can be extracted calculating the derivative of the logarithmic expression of σ(ω) versus the logarithm of the angular frequency ω as[34]:

$$s = \frac{d\ln\sigma(\omega)}{d\ln\omega} = 1 - \frac{4}{\ln\left(\frac{1}{\omega\tau_0}\right)}, \tag{24}$$

where for the characteristic relaxation time of the phenomenon under study $\tau_0 \sim 10^{-13}$ sec, the index s at ω equal to some KHz is approximately equal to 0.8[30]. The eq. (24) predicts a decrease of s as the frequency increases but

also a temperature independent behavior in the context of QMT phenomena.

If a structural distortion is associated with the charge carrier motion described by tunneling phenomena, a new excitation, the polaron, is responsible of charge transport[35]. In this case, the contribution of the polaron tunneling to the relaxation has to be kept in consideration in calculating the real part of ac conductivity and, consequently, in extracting the index s. In detail, if the polaron is assumed to be strongly localized, the spatial extent of the wave function describing the distortion cloud is at least comparable with the spacing between the two states forming the pair. In this case, at high temperatures the hopping mechanism causes the movement of small polaron, which can be then viewed as a phonon assisted tunneling between neighboring sites, while at lower temperatures the motion of small polaron takes place in a narrow band, without invoking the assistance of phonons, if the overlap between wavefunctions describing the small polaron states occurs. In this case, the index s extracted from the expression of σ(ω) can be written as[30]:

$$s = 1 - \frac{4}{\ln\left(\frac{1}{\omega\tau_0}\right) - \frac{W_H}{kT}}, \tag{25}$$

where W_H is the activation energy for the polaron transfer.

In this case, the frequency dependent tunneling distance R_ω characterizing the expression of σ(ω) and, consequently, the extracted index s, is a temperature-dependent parameter. As a consequence, the index s depends on both frequency and temperature, showing an increase as those two parameters tend to increase. Such behavior has been observed by Bobnar and coworkers in thin films based on an organic semiconductor, that is the Copper Phtalocyanine (CuPC)[36]. If the overlap of polaron distortion clouds is not so localized below the interatomic spacing between the pair states, a

large polaron is obtained. In this case an ac conductivity giving rise the following expression for s is predicted:

$$s = 1 - \frac{1}{R'_\omega} \frac{4 + \frac{6W_{H,0} r'_0}{kTR'^2_\omega}}{\left(1 + \frac{W_{H,0} r'_0}{kTR'^2_\omega}\right)}, \tag{26}$$

where r_0 and R_ω are the polaron radius and the hopping distance, respectively, $R'_\omega = 2\alpha R_\omega$ is the reduced hopping distance, $r'_0 = 2\alpha r_0$ is the reduced polaron radius and $W_{H,0}$ describes the reduced polaron hopping energy in the form of $W_H = W_{H,0}\left(1 - \frac{r_0}{R}\right)$. Again the index s turns out to be both temperature and frequency dependent, describing then a peculiar behavior for systems in which Overlapping Large Polaron (OLP) can be viewed as basic conduction mechanism.

As far as the hopping models is concerned, the first evidence regarding such mechanism in amorphous semiconductors can be dated back to Pollak and Pike[37]. In their model, it is foreseen that ionized atoms are able to hop the energy barrier W between two molecular sites. Such thermally activated phenomenon predicts in its zero-order the independence of W from the distance R between the localized states. In this particular case, the ac conductivity σ(ω) predicts a linear dependent behavior with respect frequency and temperature, giving thus s=1. If the dependence of the barrier W on R is introduced, the index s is given by:

$$s = 1 - \frac{6kT}{W_{eff} - kT \ln\left(\frac{1}{\omega\tau_0}\right)}, \tag{27}$$

where the lowering the barrier W is expressed by introducing the effective barrier W_{eff}. Such lowering arises from the thermally activated electron

transfer over the barrier between the two interacting localized states. In this case, the frequency dependence

of the index s manifests itself in its increase at higher ω while the temperature dependence of s follows the opposite trend, being s lower at higher temperatures.

All the above results are collected in a plot (taken from ref. 30) describing both the temperature (Fig. 5.a) and frequency (Fig. 5.b) dependence of the index s, showing in this way the peculiar behavior followed by each basic conduction mechanism in which pair approximation is kept in consideration as the basic assumption for the calculation of ac conductivity. These results have been plotted at 10^4 Hz, considering $\tau_0 \sim 10^{-13}$, sec by fixing the barrier height W_H in the case of SP and OLP at 0.2 and 0.26, respectively, while the barrier height for CBH has been fixed at 1.85 eV. Such values are presumed to be typical for the phenomena involved in relaxation processes in amorphous materials[30].

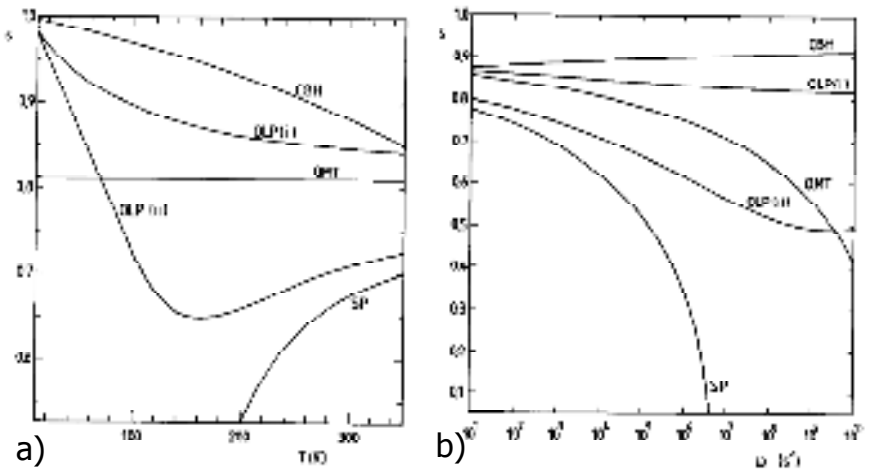

Fig. I.5: a) Temperature dependence of the index s in the case of different basic conduction models: Correlated Barrier Hopping (CBH), Overlapping Large Polaron tunneling (OLP), Quantum Mechanical Tunneling (QMT) and Small Polaron quantum mechanical tunneling (SP). Cases (i), (ii) regarding the OLP are reported for two values of the parameter r_0. Here, for SP and OLP the values of barrier height W_H = 0.2 and 0.26 eV have been chosen, respectively, while for CBH W= 1.85 eV has been used. Finally, $\omega\tau_0=10^{-9}$ has been assumed. b) Frequency dependence of the index s for the proposed microscopic transport mechanisms. For the OLP the reduced polaron radius has been fixed at 20 (i) and 2.5 (ii); W_H/kT value for SP and OLP has been considered equal to 10 while W_{eff}/KT for CBH is assumed to be equal to 75.

1.2.e) ac measurements on organic based Thin Film Transistors.

As regards the dispositivistics, the versatility of IS technique can be exploited also for the study of devices in order to evidence in a precise way their features, as it will be seen in Chapter III. In particular, UDR model will be employed in Chapter II for studying material properties while in Chapter III it will be used for evaluating their effects on devices operation. Furthermore, also TFTs can be studied via IS techniques in order to both evaluate their intrinsic conduction parameters in a precise way, extrapolating them from the overall device response (Chapter III), and clarify the problems related to their operation (Chapter IV).

In respect of the former aspect, generally dynamic measurements on TFT device structures are allowed above all on sandwich like structures. As a consequence, the IS technique is not suitable for the study of conventional bottom contact organic based devices due to their peculiar architecture. In fact, OTFTs are commonly manufactured in form of devices with a very thin semiconducting layer and, above all, a bottom like planar configuration (BC) of charge injecting electrodes (source and drain), providing then some structures in which it is not possible to single out a mechanism of complete induction for the strength lines of the electric field between these electrodes (i.e. capacitive effect into the device channel). An alternative technique consists for example in evaluating the C-V, current voltage, response of bottom-gated thin film transistors with a top-contact configuration of the source and drain electrodes. Such structures, indeed, are operatively less efficient and show some technological disadvantages, since they foresee the deposition of injecting contacts on the top of the organic layers. In this case it is very complicated to deposit electric contacts with the desired shape; in fact, it is commonly recognized that a

good device has to be based on interdigitated contacts in order to both increase the ratio W/L between the width and the length of the channel (avoiding thus the short channel effect) and to miniaturize the device active surface[38,39].

Recently, Gundlach et coworkers have discussed the possibility of performing C-V measurements on thin film transistors with a BC configuration. The method exposed by Gundlach provides a "detailed analysis of the C-V data and the frequency response of the charge-accumulated channel of the transistor"[40].The measurement is performed in the following way: the source and drain contacts are electrically shorted together and connected to the low terminals of the LCR meter, while the gate electrode is connected to the LCR meter high terminals in order to measure the device capacitance as a function of a dc gate bias (Fig. 6).

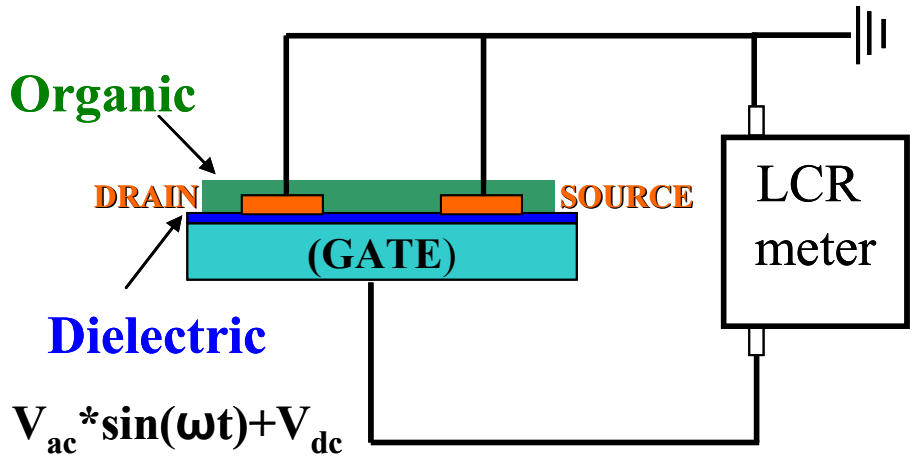

Fig.I.6: Scheme of the ac measurement technique for the characterization of BC OTFTs.

By varying the dc gate bias it is possible to monitor the dynamics of charge carriers accumulation in the channel and at the same time both to extract the total channel resistance and to extrapolate the contribution of the contact resistance from the overall channel resistance recorded by dc measurements.

The model is based analytically on a transmission line (TL) of a distributed RC network. In detail, the device channel is divided into infinitesimal elements of length dx, whose series composes the TL, where the resistance

of each element is given by dR =(r /W)dx and the capacitance is given by c'Wdx (here r is the sheet resistance and c' is the series between the capacitance of the oxide c_{ox} and the interfacial capacitance cI, that is $c'=c_{ox}c_I/c_{ox}+c_I$) (Fig. 7). As regards the last introduced element is concerned, it is clear that for OTFTs in accumulation it is $c_I \rightarrow \infty$, so $c'=c_{ox}$, while for a device fully depleted it is c'~0 (no charge at interface). Moreover, a finer version of the RC transmission line network, where a contact component consisting of a resistance element Rc in parallel with a contact capacitance element Cc has been also proposed (Mod.2 in Fig. 7).

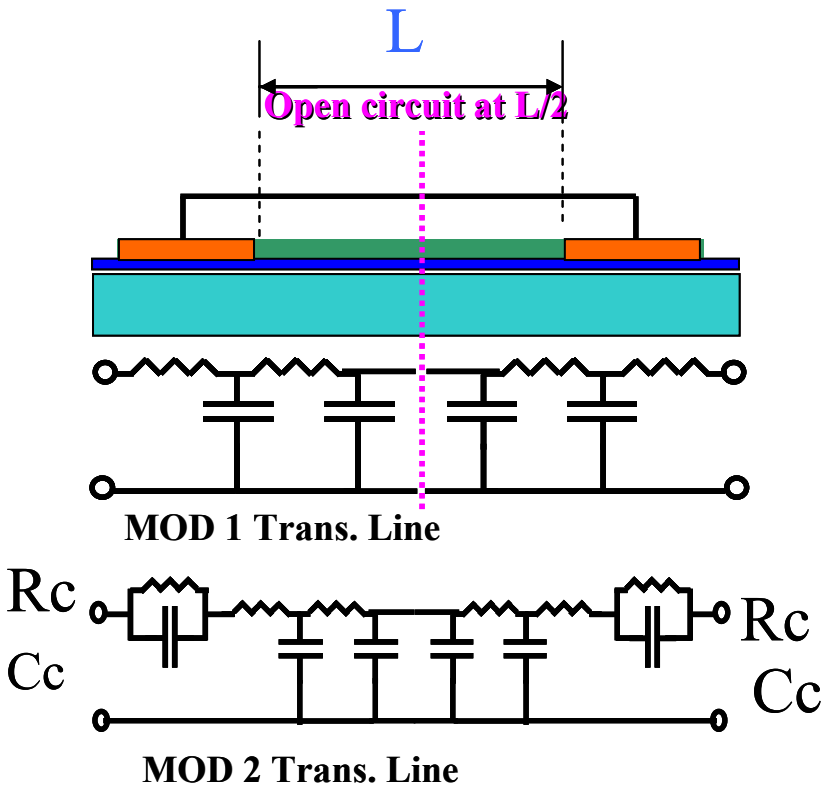

Fig. I.7: TFT in terms of a transmission line model (TLM) based on a distributed RC network (MOD 1) and a finer version (MOD 2) in which both contact resistance and capacitance are considered.

In detail, given a generic transmission line, its impedance can be written as:

$$Z_{IN} = Z_0 \frac{Z_L + Z_0 \tanh(\gamma L)}{Z_0 + Z_L \tanh(\gamma L)} \qquad (28)$$

where Z_0 is the characteristic impedance of TL (that is the ratio between the amplitude of a single voltage wave and the related current wave) and Z_L is the load impedance.

In the case of a simple distributed RC network the propagation constant γ and the characteristic impedance Z_0 are given respectively by:

$$\gamma = \sqrt{j\omega R_T C_T} = \sqrt{j\omega r' c'} \tag{29}$$

$$Z_0 = \sqrt{\frac{R_T}{j\omega C_T}} = \sqrt{\frac{r'}{j\omega c' w}} = \frac{1}{w}\sqrt{\frac{r'}{j\omega c'}}\,. \tag{30}$$

From Z_0 it is possible to obtain the characteristic admittance as:

$$Y_0 = \frac{1}{Z_0} = w\sqrt{\frac{j\omega c'}{r'}} \tag{31}$$

At this point, focusing the attention on the analyzed measurement configuration, the drain and the source are electrically shorted (V_d=V_S), so we have a parallel between two transmission lines, long L/2, closed on a open circuit (the current at the centre of our device, for symmetry, is equal to zero). So, as Z_0=0 and Z_L=∞, the expression (28) becomes:

$$Z_{IN} = \frac{Z_0}{\tanh\left(\gamma \frac{L}{2}\right)}. \tag{32}$$

By inverting the expression of Z_{IN} the admittance of the transmission line Y_{IN} is obtained as follows:

$$Y_{IN} = \frac{1}{Z_0}\tanh\left(\gamma \frac{L}{2}\right) = Y_0 \tanh\left(\gamma \frac{L}{2}\right). \tag{33}$$

In this way, using the eq. (33) of the complex admittance it is possible to solve the equivalent circuit representing the model 1 (MOD 1) in Fig.6 in order to evaluate the analytical expression of the current flowing into the channel:

$$i = j\omega WLc' \frac{\tanh\lambda}{\lambda}\upsilon_0, \tag{34}$$

where v_0 is the amplitude of the probe signal. Here, the term λ is given by:

$$\lambda = \sqrt{\left(\frac{j\omega c' r L^2}{4}\right)}. \tag{35}$$

In this context the measured capacitance is given by:

$$C = \mathrm{Im}\left(\frac{i}{\omega \upsilon_0}\right) = c' W L \,\mathrm{Re}\left(\frac{\tanh\lambda}{\lambda}\right). \tag{36}$$

The second equality has been obtained explicating the dependence of i on λ given by eq.(34).

The eq.(36) predicts a frequency dispersion for C in which the dependence on V_G is implicitly contained in the sheet resistance r. As a result, at higher frequencies it is expected a drop in capacitance as the charge carriers no longer respond to the applied ac signal (finite RC time constant).

The above mentioned finer version (MOD 2) is obtained considering an additional Z_C contact impedance for the added R_C,C_C components. In this case:

$$Z_C = \frac{jR_C}{j - C_C R_C \omega}, \tag{37}$$

And the current flowing into device is then given by:

$$i = j\omega W L c'\left(\frac{\tanh\lambda}{\lambda}\right)\left(\upsilon_0 - iZ_C\right). \tag{38}$$

So, to summarize the model is able to predict some important static parameters such as contact resistance (explicated in the finer version of the model). In particular, Gundlach has applied this model to the case of a polythiophene based TFT[40], showing that it is possible to evaluate with a good precision the contact resistance and capacitance, but also the precise mobile charge accumulated in the channel device and, consequently, the actual charge carrier mobility which generally is strongly affected by trapping mechanisms. In truth, the model seems also to be suitable for the evaluation of dynamic parameters such as the dynamic frequency

dependent response of an OTFT device. More precisely, by evaluating the frequency dependent response at different fixed dc gate voltages, the model is able to give also some important information on the maximum operation frequency for the analyzed device.

1.3) Dynamic measurements on materials and devices: Motivations and experimental set-up.

Organic semiconductors and dielectrics can be used in a huge set of device applications, starting from the conventional solid state devices up to some innovative and multifunctional applications in which the operation can be widely sustained by exploiting the peculiar structural and mechanical properties of organics, as happens in the case of sensoristics[41]. But also other aspects, such as the atoxcity, the scarce chemical activity and the biocompatibility are very useful for some device applications, such as for example the Lab on a Chip[42]. In general, the main interest in organic based materials can be summarized by invoking both their low cost character and their mechanical flexibility concretizing in the final device application such as Field Effect devices (OFETs)[43], non volatile memories[44], Light Emitting Devices (OLEDs)[4,45], Solar Cells[46], spintronic devices[47] and sensors[41].

Although organics guarantee remarkable advantages, as stated in the introductive section 1.1), many aspects about device features need to be still understood in order to reach a complete control of their response. First of all, device-quality must meet a number of stringent criteria, including long-term thermal, chemical, photochemical, and mechanical stability of organics, being such aspects dramatically affected by the nature of the weak Van der Waals interactions governing the structural features of such materials. In fact, aging phenomena, electrical stresses, but also environmental agents concur at the same time, each one with a certain

weight, to the worsening of device performances. In this respect, the short device lifetime limits the employment of organics to those applications in which it is not required a long time operation. Furthermore, the structural disorder reduces dramatically the commutation of organic based switches, so their range of applicability is restricted to not particularly fast applications.

In this respect, the attention of researchers is mainly focused on the development of strategies aimed to the reaching of the best conditions for the improvement of device life-time and performances. All these topics regard directly the manipulation of materials in phase of both synthesis and thin films deposition, respectively. In fact, chemical functionalization of organic materials can impart advantages in terms of stability, but also in terms of charge transport (due to the improvement of structural order), while the self-assembling and self-organization of oligomers, controlled by means of deposition parameters, ensure the high degree of order required for improving both device miniaturization and performances. The growth, however, is a process intrinsically out of thermodynamic equilibrium conditions, so the control of the film morphology, and consequently the reproducibility of device response, is not obvious, even if it is possible to reach growth conditions close to equilibrium by acting on the substrate temperature and the deposition flux. Otherwise, different kinetic aspects have to be considered for controlling the final morphology[48].

Of course, not only the bulk of organic materials concurs to device working. In fact, an organic based device can be viewed as a whole like a series of different interfaces. The most important interface, is the hybrid heterojunction between the charge injecting metal and the organic active layer. The paramount importance of such interface in device working has been widely underlined since the beginnings of device applications. In fact, in most cases the order of magnitude of the strong mismatching between the work function of the injector and the conducting molecular levels (i.e.

HOMO and LUMO levels) is of one eV. This aspect has been looked at as a limiting factor for the ohmic injection of charge carriers, generating for example SCL phenomena in OLEDs with a negative effect on device efficiency[49]. Otherwise, the interfaces are not only a limiting factor, since in some applications they sustain completely the device working, as happens in the case of Organic Spin Valves or in the case of vertical OFETs[50]. Moreover, other important interfaces characterize some device applications. In this respect, the interface between the conducting channel and the gate dielectric, generally SiO_2, is decisive in terms of the field effect induction. In fact, it is widely known that a special care has to be dedicated to the cleaning and the functionalization of such interface in order to reduce trapping phenomena and consequently bias stress phenomena[51]. Finally, it is worth to mention that also the same oligomers tends to form different interfaces, according to their morphology. Grain boundaries occurred for growths out of equilibrium, but also the interfaces between two adjacent layers obtained in near-equilibrium conditions can produce undesired effects, such as eventual scattering of charge carriers at the grains[52] or the arising of interfacial dipoles[15].

Therefore, on the basis of the above mentioned topics, the comprehension of organic devices with the aim of governing their overall response requires the introduction of the dynamic alternative techniques of electrical characterization. The main request for such techniques is the capability of separating each individual effect concurring to the overall device response from the others, allowing in this way the better understanding of any aspect exploitable for bettering device working and for introducing novel possible applications. This task is well accomplished by the dynamic character of those measurements exploiting varying fields as probing tools.

In fact, the employment of dynamic measurements in the case of organic materials is a powerful tool for probing the local effects governing their response (since the macroscopic conduction and the structural features are

the outcome of the cooperation of local effects), also in a non invasive way, due to the low electric fields needed for the response analysis. The implementation of the dynamic technique to the case of devices, instead, needs to be framed in the context of both their architectures and operation principles. In fact, the requirement of a preliminary comprehension of the suitable circuit representations used for the description of the relaxation dynamics in devices, favors the practical understanding of the tools aimed to both the knowledge and the bettering of device properties, since the analysis of the effects displayed by the parts composing a device allows eventually to control its overall response.

As far as the operative aspect of dynamic electric measurements is concerned, IS is performed by means of an LCR meter (Fig. 8.a)) in a frequency window ranging between 100 Hz and 1 MHz, operating with a signal amplitude ranging from 10 mV to 20 V peak-peak and a dc bias stress ranging from -40V to 40V. The electric contact between the instrument and the device electrodes is carried out by means of a cryogenic probestation (Figs. 8.b), 8.c)) in which both temperature (from cryogenic values to about 100 °C) and vacuum conditions (from 10^{-5} mbar up to atmospheric pressure), but also the air composition and its humidity content can be controlled. The probe station is equipped with four arms, able to operate also in radio frequency regime, closed on metallic tips. The probing of the electric response is carried out by landing with micrometric slides the metallic tips on the injecting electrodes. Alternatively, also a closed cycle cryocooler in which temperature ranges from 40K to about 350K can be used (Fig 8.d)). The experimental apparatus is controlled by a NI Labview 7.1 software. Furthermore, it is worth to mention that not only the IS techniques facilitate the comprehension of device response. In fact, also other protocols of dynamic measurements, with a special reference to those performed by applying opportune waveform-like voltage sweeps to devices, allow to study the operating limiting factors. At this purpose, as it

will be widely treated in chapter IV, it is possible to monitor stress phenomena in device structures by applying triangular waveform scan sweeps to OFETs. This is done in order to monitor trapping phenomena occurred in the device channel on shorter timescales with respect those involved in the process of charge trapping. Again, the dynamic measurement turn out to be a practical, non invasive tool for the study of organic devices. Moreover, as far as the experimental procedure is concerned, in this case some electrometers (i.e. a picoammeter and a source meter) are employed in a first time for both materials and devices responses and, then, for dynamic measurements on OFETs. Operatively, the triangular wavelike scan voltage is controlled again by Labview 7.1 software.

Finally, it is clear that an extremely wide-ranging picture of device properties can be obtained by exploiting the dynamic techniques. Even if both the versatile IS technique for device analysis and the timely dynamic study of stress phenomena are for sure not simple, they allow to link several individual aspects in the context of the overall device behavior.

So, finally, it can be deduced that the dynamic measurements are an essential requirement in the bosom of the knowledge of organic materials and device applications.

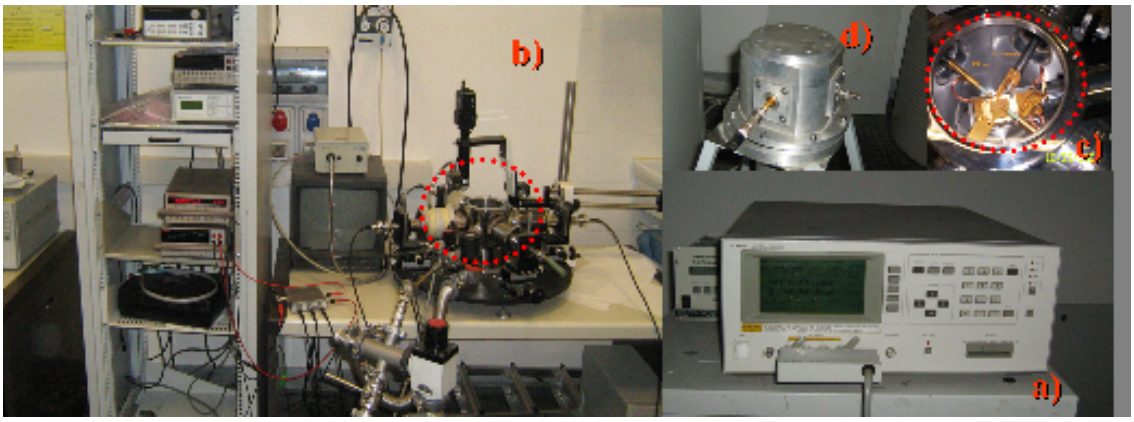

Fig. I.8: experimental set-up; a) LCR meter; b) cryogenic probe station; c) view of the internal probe chamber; d) closed cycle cryocooler.

Chapter II

Electrical characterization of organic materials.

2.1) Introduction: IS technique for the characterization of organic conducting materials.

The first step towards the development of good performing electronic devices based on organic thin films pertains to the knowledge of the materials employed as active layers in device operation. In fact, in accordance with the operation executed by a device, the active material which allow to put in practice such operation has to meet some requirements. For instance, a satisfactory high commutation speed of an OFET requires a high field effect mobility for the semiconductor employed as device channel, while the capability of hosting external analytes, exploitable in sensoristics, needs for opportune structural and chemical features for the organics composing the active part of a sensor.

The primary purpose of the comprehension of material properties lies in the fact that the knowledge of microscopic basic mechanisms offers a tool for an intervention aimed to obtain the desired control of macroscopic properties. This intervention is operated in different ways since, for example, it is possible to tune the properties of the individual molecules by means of an opportune chemical functionalization or to operate on the film morphology by controlling the deposition parameters.

In regard to such topics, in this chapter two examples of material analysis performed by IS technique will be treated.

In the first example, a conducting polythiophene (PT), opportunely functionalized for improving its charge transport properties, will be studied (section 2.2) in order to elucidate the efficiency of the operated chemical functionalization in terms of the reaching of an improved conduction and, above all, for emphasizing the powerfulness of IS technique in terms of a precise clarification of the microscopic conduction mechanisms. This will be done in the context of the Universal Dielectric Response (UDR) model, which has been introduced in the seventies by A.K. Jonscher[29] in order to

adapt the features of the complex dielectric permittivity ε(ω) to the case of disordered organic materials.

In the second example IS technique will be employed for the study of dynamic glass transition experienced by rubbery materials too. In particular, the technique will be employed for determining in a non invasive way the relaxation processes induced by phase transitions in the case of Polydimethylsiloxane (PDMS) thin films (section 2.3), a well known dielectric material which can find employment in several technological applications such as the microfluidics.

2.2) Conducting properties of organic semiconductors: properties of thiophene-based semiconductors.

PTs are for sure among the most studied p-type organic semiconductors. Their basic unity, the thiophene ring, is an aromatic heterocyclic compound consisting of four carbon atoms and one sulfur atom in a five-membered ring (Fig.1). The resulting molecular formula is C_4H_4S. Thiophene was discovered by Viktor Meyer in 1871[53] as a contaminant in benzene. Among thiophene basic properties, the solubility in most organic solvents and the immiscibility in water, together with the melting point at 235 K and the boiling point at 357K, render it promising for device application, being the molecule easily processable and structurally stable at room temperature.

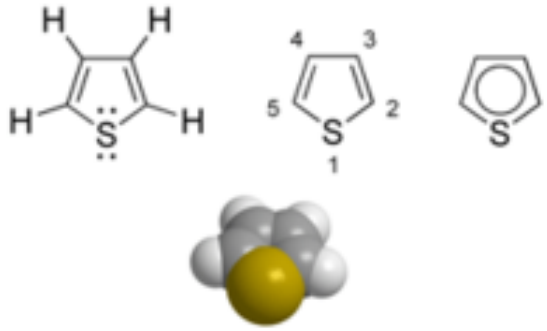

Fig. II.1: Chemical structure of thiophene.

PTs result from the polymerization of thiophene rings. A wide class of PTs which is very promising in the fabrication of OFETs, but also OLEDs and Solar Cells, can be obtained by operating a substitution in position 3 of the thiophene ring with alkylic, alkoxylic, alkylphenyl and alkoxyphenyl groups. The most known PT is poly [3-hexyl-thiophene] (P3HT), for which a considerable record of 0.3 $cm^2*V^{-1}*s^{-1}$ for field effect mobility has been reported[54]. High values of field effect mobility can be reached thanks to the in-plane lamellar self-organization of polythiophene chains (Fig.2).

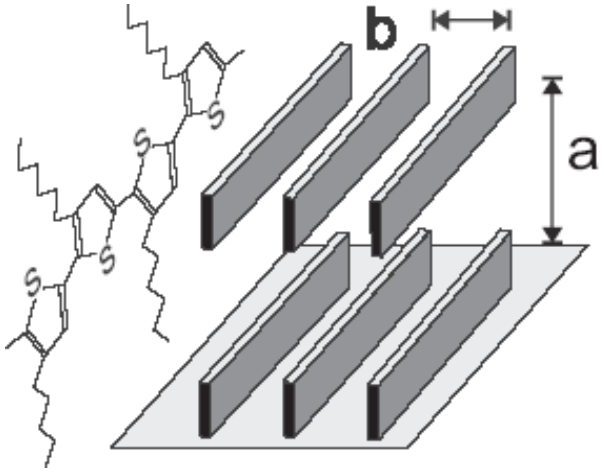

Fig. II.2: Regioregularity: in-plane lamellar self-organization of polythiophene chains.

This property, named regioregularity, is then a milestone for an efficient charge transport. In fact, the regular head-to-tail connection sequences favors the stretching of the polymeric backbone along the plane, providing thus a wide delocalization of the π electronic density. This type of structural organization supports the charge carrier transport, dominated by hopping phenomena, and determines the macroscopic conductivity. Regioregularity can be reached by acting on the polymerization process of the starting 3-substituted thiophene monomers. The resulting lamellar structure is reached thanks to the presence of side-chain groups conferring a ribbon-like packing of macromolecules. In this respect, at present time many issues are opened about the influence of the polymeric properties on the conducting efficiency. In particular, many studies deals with the influence of side chain length on the mobility[55,56].

2.2.a) Preliminary dc characterization: sample preparation, structural and morphological characterization; experimental results.

In this section, the electric transport properties of a regioregular poly [3-(4-octyloxyphenyl)-thiophenes] (POTs), a poly[3-(4-alkylphenyl)thiophenes] with n=8 (Fig.3.a), will be studied in order to classify to the first order the

overall response of such material, while the IS will be employed in the next sections for clarifying the basic conduction mechanisms of such material. In detail, this material has been synthesized by oxidation of 3-(4-alkylphenyl)-thiophenes) (with n=8) (Fig3.b) operated with molecular oxygen O_2 in presence of $VO(acac)_2$ (vanadyl acetonate), used here as catalyst[57,58].

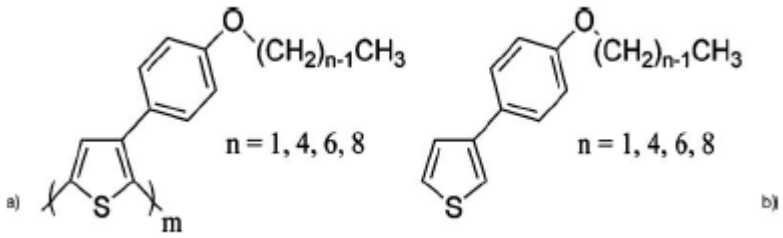

Fig. II.3: Molecular structure of a) polymers and b) corresponding monomers; the poly [3-(4-octyloxyphenyl)-thiophene] is obtained for n=8.

In this reaction, as expected on the basis of the properties showed by alkoxylic chains, the obtained polymers show an high regioregularity, a great electron donor capability (which improves the hole density) and are completely soluble. Moreover, they are thermally stable and preserve their structural order upon deposition by spin coating technique, without any further procedure of annealing.

The deposition of 1μm thick films has been carried out in this case from an opportunely filtered chloroform solution (about 5% by weight) on glass substrates. The thicknesses of the obtained thin films have been measured with an Alphastep profilometer.

The morphological and structural features of the manufactured samples have been extensively checked by means of optical analysis and diffraction methods. In particular, ultraviolet-visible (UV-VIS) spectra have been collected at room temperature by a JASCO V-560 spectrometer, while X-Ray diffraction technique has been carried out by a Geiger counter with a Ni-filtered Cu Kα radiation.

UV-VIS spectra are reported in Fig.4. These spectra furnish a good checking of the reached regioregularity in phase of synthesis and preserved during the deposition. In fact, as reported by Mc Cullough[59], regioregular polymers are characterized by a peak of absorbance located about at 550-560 nm, and a fine structure with secondary peaks located at 590-600 nm and at 665-700 nm.

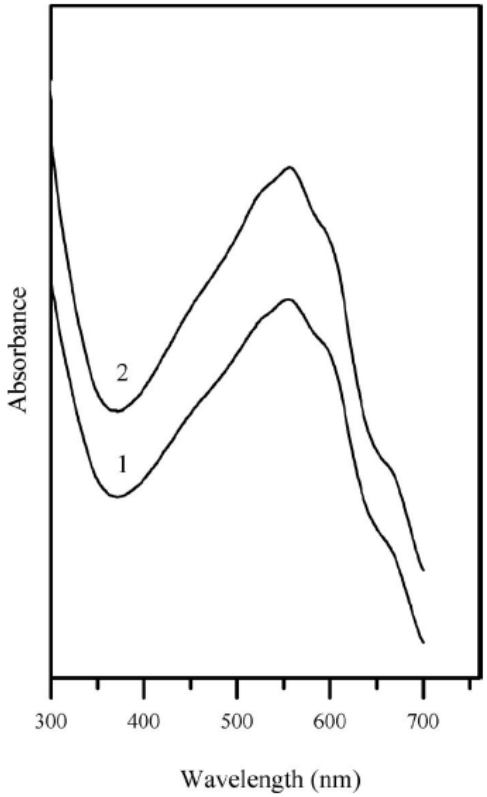

Fig.II.4. UV-Vis spectra of poly [3-(4-octyloxyphenyl)-thiophene; 1 spin coated sample, 2 sample annealed at 200°C.

The collected spectra regard the bare films obtained upon spin coating (curve 1) and films that have undergone an annealing procedure at 200°C for 10 minutes (curve 2). It is clear that both the spectra are similar in all the investigated range of waveligth. According to McCullough statements, this experimental evidence confirms the high degree of regioregularity of the spincoated POTs films, also without recurring to annealing procedures, being the high degree of the reached regioregularity about 94%[60,61].

The powder diffraction measurements have been carried out on solution casted polymeric films. These measurements have indicated a close

ribbon-like packing model, that is a structure in which polymeric backbones are planar (spacing between lamellae ~ 28Å) and alkoxylic substituents are disposed as reported in Fig. 5 (the ribbon thickness, that is the height of each lamella, is about 28 Å).

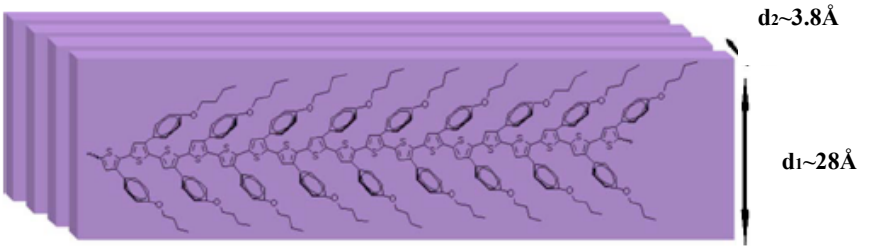

Fig.II. 4: Schematic representation of polymers packing.

The checking of dc response has been performed by recording I-V characteristics both on planar and vertical geometries of charge injecting electrodes. In the first configuration, the gold electrodes have been deposited by thermal evaporation on the top of the samples, where the second configuration has been obtained by sandwiching the semiconducting film between evaporated gold electrodes in cross configuration. The conducting channel length L for the two configurations is 100 nm and 1 μm (film thickness), respectively. The channel width for the planar configuration is W= 5mm, while the surface A of the cross sections of the two measured vertical structures is 0.1 × 0.1 mm^2 and 1 × 0.1 mm^2, respectively. The device layouts are showed in Fig.6.

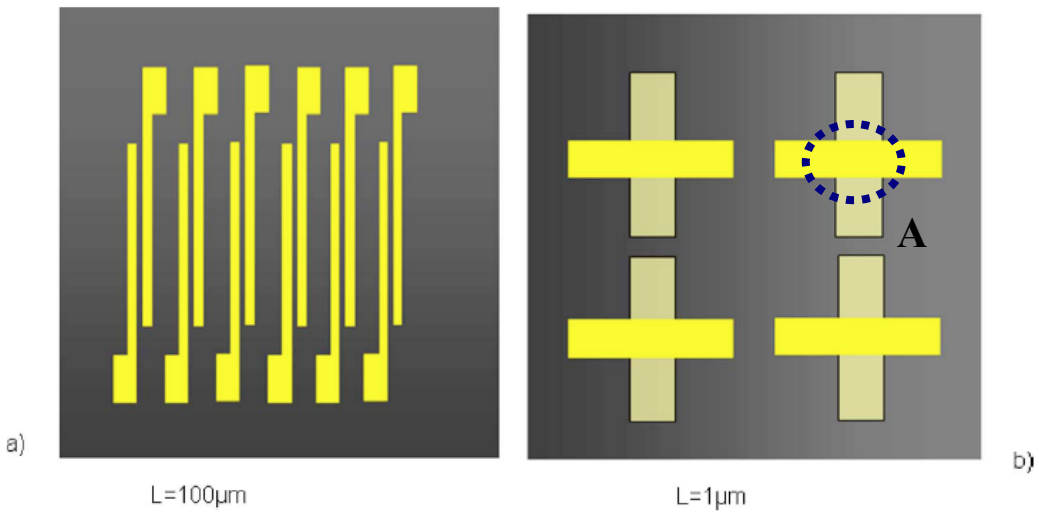

Fig. II. 5: Planar a) and vertical b) layouts of the injecting electrodes.

The measurements have been carried out in vacuum by a Keithley 487 picoammeter closed on the probes of the cryogenic probe station. Vacuum conditions are a fundamental request for the evaluation of polythiophenes electrical properties. In fact, the thiophene based polymers experience a strong oxidative effect in air resulting in a dramatic spontaneous doping[62,63]. This aspect is undesired in device applications, above all in the manufacture of efficient OFETs. In this respect, the spontaneous doping tends to worsen the device performances by acting on the on-off ratio, since the field effect doping is masked by an undesired doping level in device off state[64].

The I-V measurements in planar configuration, recorded at different fixed values of environmental temperature ranging from 295K to 350K, have evidenced both ohmic and space charge limited current (SCLC) regimes, at low and high electric fields, respectively, that is a crossover of the electric current between a linear behaviour with the applied electric field and a square power low of the electric field (Fig.7). The crossover between the observed regimes occurs for a value of the electric field equal to 10^4 V/cm, in agreement with the values reported in literature for many amorphous materials[65,66].

In this way, conductivity and mobility can be simultaneously extracted by using the expressions of ohmic and SCL currents for two dimensional thin films[67]:

$$I_{ohm} = \frac{\sigma * d * W}{L} V \qquad (1)$$

$$I_{SCLC} = \left(\frac{2}{\pi} W \mu_{\text{int}} \varepsilon \frac{V^2}{L^2} \right) \qquad (2)$$

where W and L have been already defined, σ is the dc conductivity, V the applied voltage, μ_{int} the intrinsic charge carrier mobility, $\varepsilon=\varepsilon_0\varepsilon_r$ the material permittivity (ε_0 is the free space permittivity, or electric constant, ε_r is the dielectric constant of the organic film).

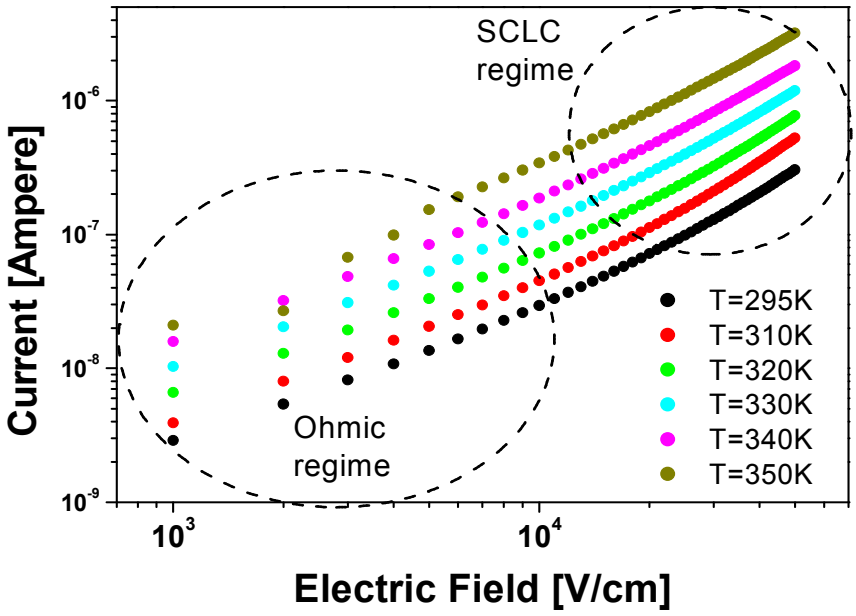

Fig. II. 6: I-V measurements performer on poly [3-(4-octyloxyphenyl)-thiophene] thin films in planar configurtation in a temperature range from 295 K to 350 K

Similar measurements have been carried out in transverse configuration using this time the three dimensional expression for SCLC regime (bulk materials):

$$I = A * \frac{9}{8} \varepsilon \mu_{\text{int}} \frac{V^2}{L^3} \qquad (3)$$

where A is the surface of the electrodes cross section. The intrinsic conduction parameters have been extracted from all the performed measurements, indicating a strong anisotropy for charge conduction (Tab.I). This aspect confirms the high degree of regioregularity reached for simply spin coated POTs films.

CONFIGURATION	*CONDUCTIVITY (S/cm)*	*BULK MOBILITY (cm2 /Volt*sec)*
PLANAR	$3.66*10^{-8}$	$1.29*10^{-3}$
TRANSVERSE	$0.63*10^{-9}$	$0.438*10^{-5}$

Tab.II.1: Room temperature conductivity and mobility for films measured in planar and transverse configurations.

Here, it is worth to mention that the bulk mobility is strongly lower than the field effect mobility, being it an intrinsic parameter of the organic

material, while in the case of transistors devices it can be increased by means of the field effect doping.

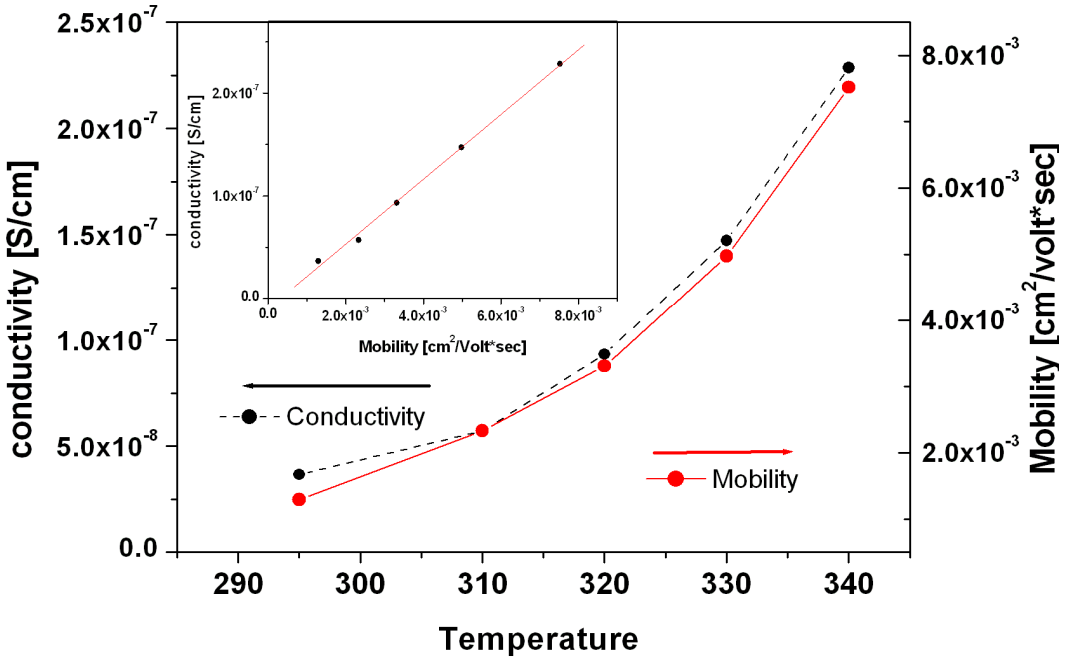

Fig. II. 7 Conductivity (●) and charge carriers mobility (●) as a function of temperature, extracted from the measurements showed in Fig.8 using the formulas (1.a) and (1.b), respectively.

As far as the semiconducting nature of POTs is concerned, temperature dependent measurements show that conductivity, as expected for semiconductive materials, depends linearly on mobility (Fig.8, see the inset). Assuming that $\sigma=n\mu E$, where E is the applied field, the charge carrier density results to be 1.5×10^{14} cm^{-3}.

Moreover, temperature dependent measurements can furnish also information about the basic charge carrier transport mechanism, since as reported in chapter I, a comparison between experimental conductivity temperature dependence and Mott's Variable Range Hopping model (eq. (1) in chapter I) can be simply performed (Fig.9).

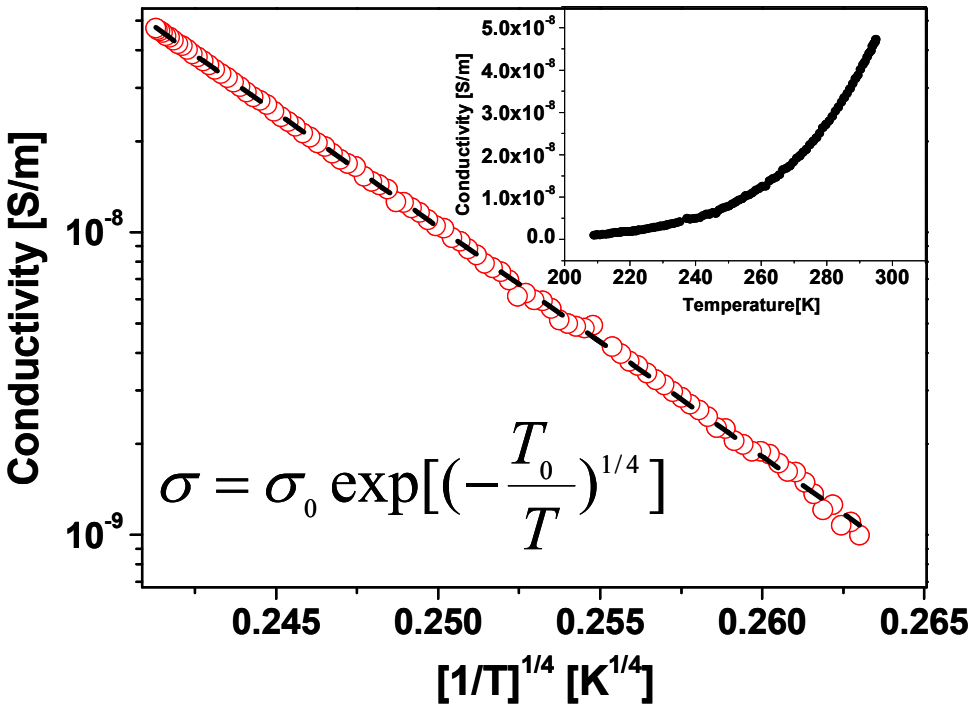

Fig. II. 8: dependence of dc conductivity vs. temperature (scattered red curve) and comparison with VRH model prediction (dashed line) in a semilog plot as a function of $1/T^{1/4}$; in the inset it is shown the relative σ(T) measurement.

The experimental result confirms that, in a semilog plot, the experimental measurement depends linearly on $1/T^{1/4}$, according to the classical Mott's formula (indicated in Fig.9). Such measurement can also furnish information on some parameters such as the density of states at the Fermi level [see chapter I, eq.(2) $N(E_F)=1/\xi^3 kT_0$, in this case, assuming that the localization length is equal to 3.7 Å, the distance between two thiophenic rings, $N(E_F) = 4.468 \times 10^{18}\ cm^{-3}\ eV^{-1}$].

The analysis performed confirms that dc measurements can allow to extract many useful information about the features of materials, giving also the possibility of both extracting some conduction parameters and singling out the overall conduction mechanisms governing the transport in organic semiconductors. In this respect their usefulness is undoubted. Otherwise, dc measurement limitation consists in the fact that it does not represent a

criterion suitable for the investigation of local effects, since this technique furnishes an overall view of the charge conduction mechanisms, allowing the assessment of both macroscopic and microscopic conducting parameters. Moreover, microscopic parameters are extracted in the context of the global temperature dependent dc response showed by organics, so they can be viewed as an effect averaged on a wide range of temperatures. In general, it is expected that the environmental temperature supports the charge transport mechanisms above all at its higher values, since the thermal effects are in this case energetically comparable to the interactions sustaining the structure of organic material. So, both the requirement of investigating the thermal effects on charge conduction and the demand of depicting a wider scenario concerning the basic conduction mechanisms, imply the use of powerful probing tools, able to furnish the opportunity of focalizing the investigation on local aspect. This task can be surely performed by means of IS technique.

2.2.b) ac measurements on thiophene-based polymeric thin films: conduction mechanisms in polthiophenes.

The analysis of PTOs properties via ac measurements shows that such material at room temperature shows semiconducting properties. In this respect, the capacitance C and the ac conductance σ_{ac} measured in a parallel RC mode representation as a function of frequencies at T_{room}. Just as a reminder, it is worth to remember here the expressions of permittivity and ac conductivity extracted in the context of UDR model, also going back over briefly their sense.

UDR model predicts a sublinear behavior for the frequency-dependent conductivity $\sigma(\omega)$ (with $s<1$):

$$\sigma_{ac} = \sigma(\omega) = \sigma(0) + A\omega^{s}, \qquad (4)$$

where σ(0) represents the dc conductivity, generally separated from the ac contribution and A, which is weakly frequency dependent, is the constant phase element showing both the dispersion of conductivity and the dielectric properties of the filling material. The origin of (4) lies in the intimate character of many-body interactions occurring among the organic material basic constituents, which lead to a cooperative relaxation of polarizable entities rather than an independent behavior for them under the effect of a varying field. The frequency dependent behavior of the dielectric constant can be deduced instead by exploiting the casuality principle (Kramers-Kronig relations) from the eq.(4). In this case:

$$\varepsilon_r(\omega) = \varepsilon'(\omega) = \varepsilon_\infty + \frac{A}{\varepsilon_0}\tan\left(\frac{\pi s}{2}\right)\omega^{s-1}, \qquad (5)$$

where ε_∞ is the dielectric constant for $\omega \to \infty$. The intimate link existing between eq.(4) and eq.(5) is clearly deducible from the power law index s-1 describing the frequency dependent behavior of the dielectric constant that is the complement to the unity of the power law index s in ac conductivity.

The experimental results, displayed in Fig.10, show that the analyzed material is conductive. In fact, the value of the index s extracted from both experimental curves, that is equal to 0.8, indicate the conducting nature of POTs spincoated thin films. Moreover, also the parameter A extracted by $\varepsilon_r(\omega)$ curve is in agreement with the value extracted from $\sigma_{ac}(\omega)$. This agreement is expected for systems obeying to the UDR model, since the behavior of the capacitive element is obviously linked to that of the resistive one, in accordance with the sense of Kramers-Kronig relations.

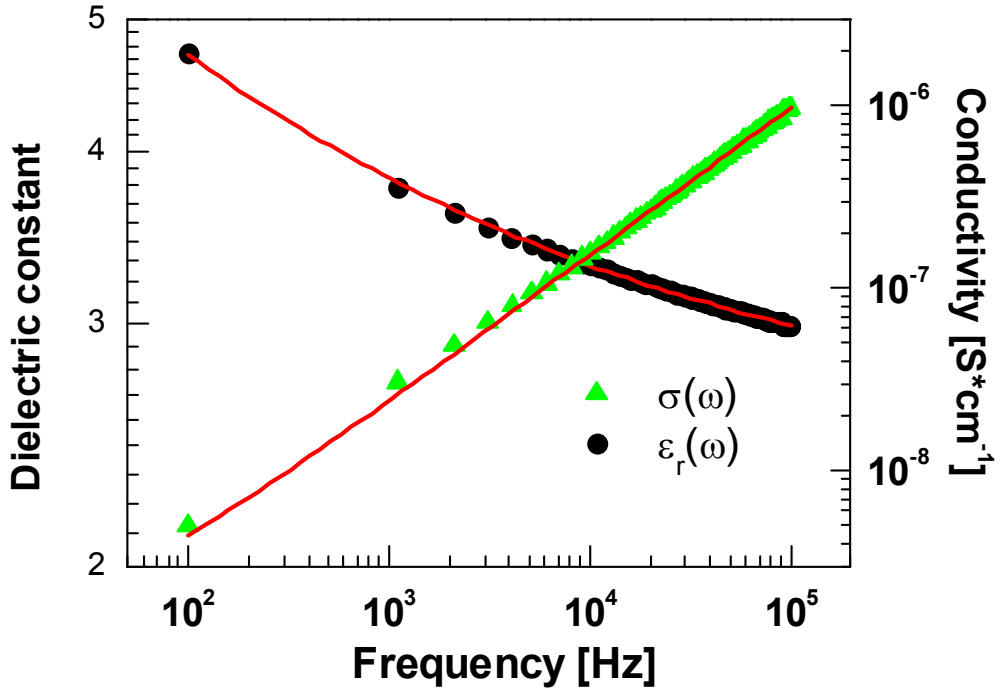

Fig. II. 9: Dielectric constant (●) and conductivity (▲) vs. frequency; the curves, recorded at room temperature, are fitted by using the UDR model (red lines).

In table II the fitting parameters extracted from data recorded in Fig.10 are reported.

	UDR fitting parameters
ε_∞	2.52
A	8.7×10^{-11}
s	0.81

Tab.II.2: The fitting parameters extracted for the curves displayed in Fig.11. In particular, the value of the parameter A extracted by $\varepsilon_r(\omega)$ curve is in agreement with the value extracted from $\sigma_r(\omega)$.

The UDR model offers the possibility of determining the ac conductivity of PTOs thin films with a cross-like vertical configuration of electrodes. In

particular, exploiting the temperature dependent behavior of the index s extracted by the power law describing ac conductivity, it is possible to analyze the main issues of the basic conduction mechanisms to which charge transport in such materials obey. In this respect, it already has been argued by other studies that the overall macroscopic conductivity is the summation of individual processes that can be described as quantum mechanical tunneling through the energy barrier or thermally activated hopping over the energy barrier separating two equilibrium sites[31,68,69]. In order to discriminate among the possible microscopic conduction mechanisms, the behavior of s against the varying environmental temperature has been assessed by measuring the capacitance C and the ac conductance σ_{ac} as a function of frequencies at different fixed temperatures (Fig. 11a, 11b). Moreover also temperature dependent measurements at fixed frequencies of the applied field have been recorded (Fig. 11c, 11d). Such measurements show that both C and σ_{ac} decrease with temperature, being as expected such decrease less pronounced at higher frequencies[70]. The dependence of s from temperature has been calculated as:

$$s = \frac{d \ln[\sigma(\omega)]}{d \ln(\omega)} . \qquad (6)$$

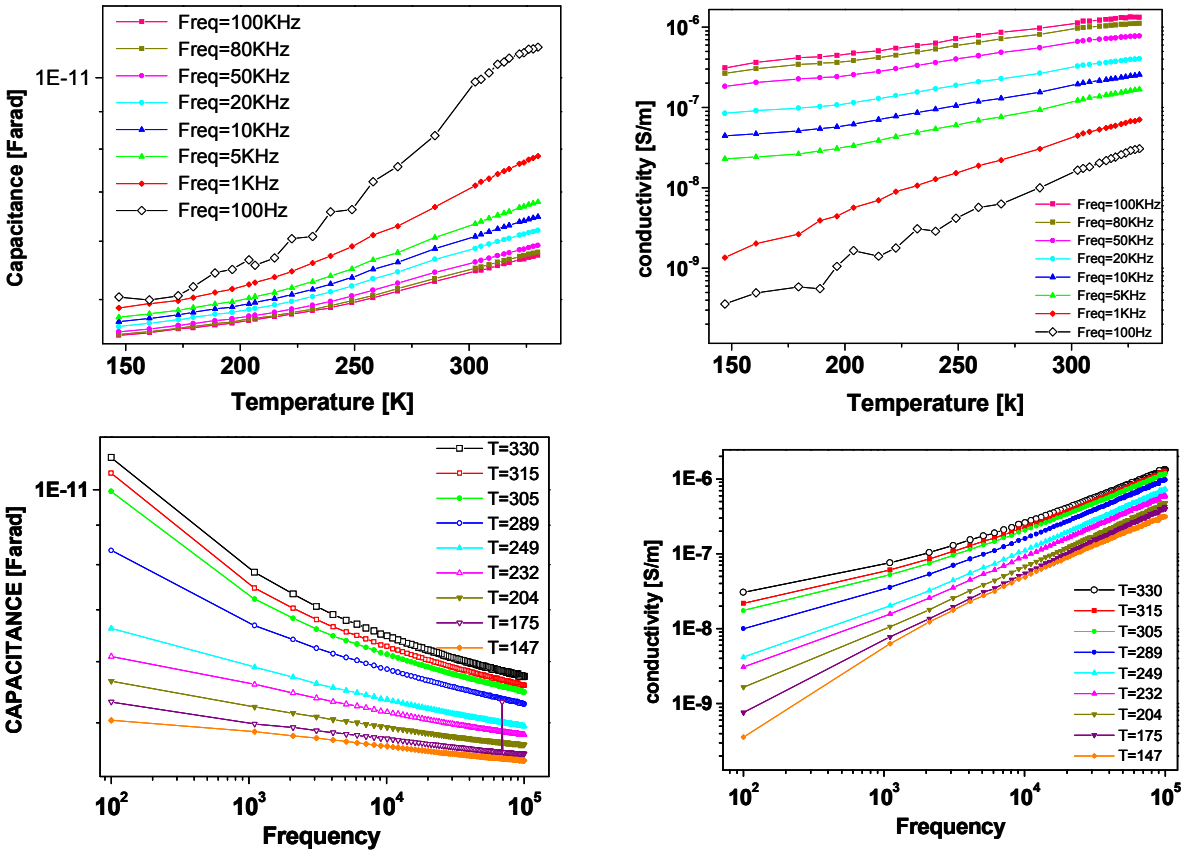

Fig. II. 11: a) Capacitance and b) conductivity as a function of frequency at different temperatures. C) Capacitance and d) conductivity temperature dependance measured for different frequencies.

The experimental results, reported in Figg. 11 and 12, reveal that the index s is really frequency dependent. For $T>T_{room}$, in fact, s slightly increases with frequency, while at lower temperatures (less than 250K) s decreases with frequency. In the context of the quantum mechanical calculations of s performed supposing different basic conduction mechanisms, ac measurements over a wide range of temperature and frequency reveal that is not possible to describe the ac properties considering only one conduction basic model. In particular, in agreement with dc measurement, at room temperature and low frequencies the influence of thermally activated hopping mechanisms between localized states on charge transport dominate the motion of carriers, whereas quantum mechanical tunneling mechanisms are more relevant when temperature decreases. It is

also evident that at high frequencies (f>10KHz), s value (about 0.8) is almost temperature independent. This occurrence suggests in turn that QMT mechanisms are more significant at higher frequencies.

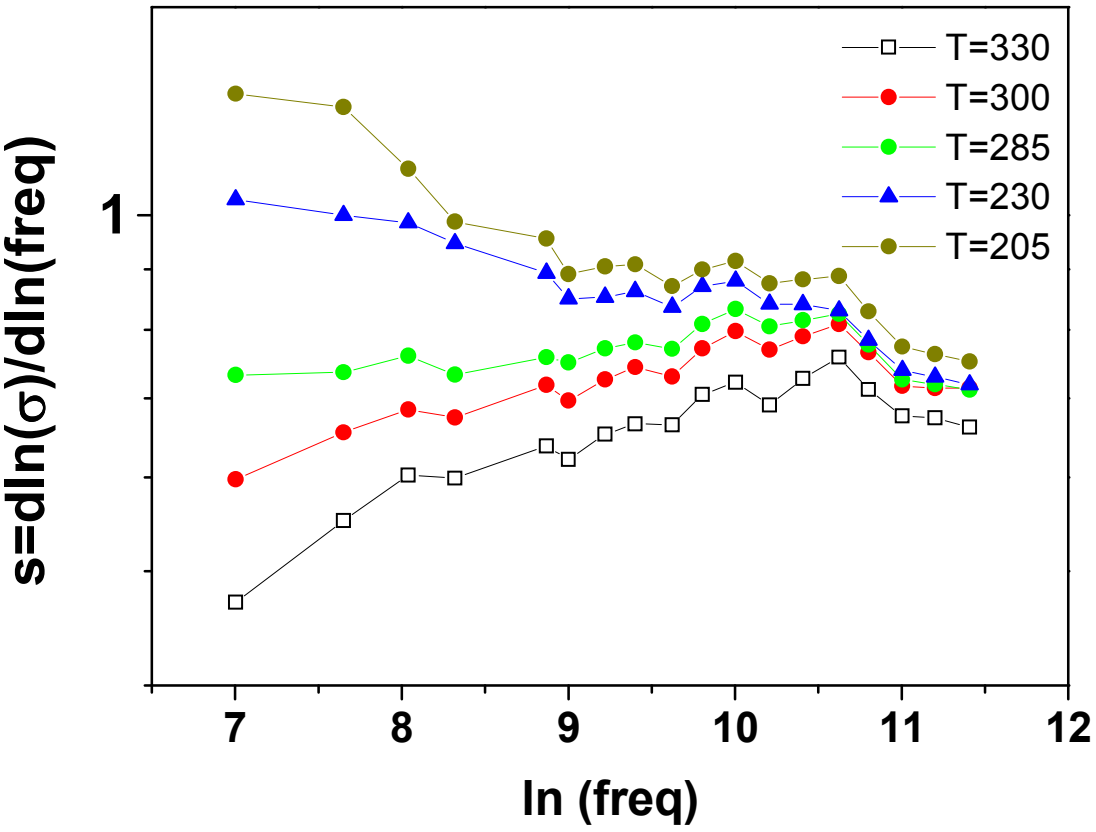

Fig. II.12: Frequency dependence of the index s, extracted using eq. (13), at different environmental temperatures.

2.3) Phase transitions in organic based dielectric materials.

The basic study of charge transport conduction mechanisms is performed form the study of the ac conductivity in a RC parallel mode representation. In particular, the behavior of charge motion under the effect of an ac field is deduced by monitoring the peculiar effects produced on the resistive element in the RC parallel circuit representing the sample. As remarked in the last section, also the ac study of the capacitive element shows a peculiar behavior according to the physical nature of the analyzed material, since the UDR model represents the tool suitable for the description of relaxation in different disordered materials. Thus, the monitoring of the ac response of organic materials with dielectriclike properties can be likewise carried out by IS techniques.

In this respect, a very important aspect of IS technique has to be underlined. In fact, relaxation phenomena in organics can furnish a powerful criterion for a non invasive analysis of phase transition in such materials. So, on the basis of this important further aspect, in the next sections the usefulness of IS in terms of phase transition temperature evaluation, compared to the features of standard techniques showing many limitations in the case of thin films, will be first discussed and then showed with a practical example.

2.3.a) Phase transition in organic materials: standard techniques versus Impedance Spectroscopy for the evaluation of glass and melting transition temperatures.

Among the distinctive phase transitions in organics, a very important issue in material physics concerns the nature of the “glassy” state of matter. In detail, rubbery polymers, upon cooling, undergo a typical Glass Transition and in many cases a partial crystallization, depending on the eventual

presence of structurally ordered domains. The basic topics of this peculiar phase transition lie in the amorphous structure of the organic materials, which involve some typical effects consisting in the arising of this peculiar phase transition. Glass transition sets its basic macroscopic features into the framework of a microscopic theory, that is the Free Volume theory (FV). In short, glass transition can been depicted as a peculiarity of amorphous materials with weak Van der Waals forces governing the interactions among polymeric chains. In particular, the glassy state of matter can been viewed as an effect linked to the reduction of the FV in which polymeric chains can move. In this scenario, glass transition can be explained in terms of the lowering of segmental mobility, generally ascribed to a reduction of the free volume, occurred upon cooling, up to the chains are completely frozen below a certain temperature, indicated as T_g (glass transition temperature). Unlike it happens in the case of melting transition, which is classified thermodynamically as a first order phase transition and is ruled by equilibrium processes, such transition is classified apparently as a pseudo-second order phase transition, , since it shows a discontinuity in the first temperature derivative of the geometric volume, not an abrupt reduction of it as happens during the crystallization.

This means in turn that glass transition is a kinetic phase transition (not thermodynamically at equilibrium). This aspect is of paramount importance under the experimental point of view, since the evaluation of glass transition temperature value T_g can be strongly affected by the kinetics of the experimental procedure chosen each time for its assessment (being T_g characterized by a range of values, not by an unique value).

Essentially, T_g depends slowly both on the cooling and heating rate[71], being generally lower for smaller rates, and it approaches the ideal transition point T_g^* in the asymptotic limit of vanishing rate[72,73]. Moreover, the glass transition temperature value T_g assessment in the case of polymeric thin films depends on the film thickness[74], on the features of the

interactions between the film and the substrate[75] but also on the molecular weight of the constituents, on the thermal history and the age of the analyzed material.

So the precise knowledge of T_g in defined device architectures generally has to disregard the results obtained by conventional methods of measurement. In particular, the strong dependence of T_g from the features of the experimental methods employed for its evaluation is dramatic if, for example, one thinks of using thin films as gate dielectric in flexible field effect devices[76] or as packaging materials for devices, food, or objects sensible to wide variations of environmental temperature. Moreover, all the conventional methods used for T_g evaluation, such as the most used Differential Scanning Calorimetry (DSC), the mechanical Elastic Modulus Method or the Dynamic Mechanical Thermal Analysis (DMTA), show many disadvantages. In fact, first of all, being reminiscent of the just above mentioned T_g dependences, such methods are generally employed on materials in form of powders or bulk samples, not on thin films. This aspect has to be kept in consideration if one considers that the strong dependence of glass transition from the employed method sometimes is so wide to cover many tens degrees Celsius. Furthermore all these standard methods are decisively invasive since they are based on the probing of thermal and mechanical properties of materials, showing also a scarce sensitivity in many applications. In particular, above all as regards the latter aspect, the glass transition is probed via evaluation of some quantities, like the elastic modulus or the specific heat capacity, directly linked to the observation of macroscopic effects.

So, the evaluation of phase transitions on thin films with the desired geometries (apart from the Ultra DSC measurement employable on films with a lot of difficulties[77]), carried out adopting a method useful for testing their precise effect in the case of devices, requires the utilization of finer techniques. In particular, the techniques required have to be based on the

probing of local effects induced by the freezing of polymeric chains. The electric measurements can be useful in this sense. Many studies deal with the evaluation of phase transitions in the case of confined molecular condensated, such as acetonitrile[78] or carbon monoxide (CO) condensed in mesoporous glasses[79], and polymeric thin films, such as polydimethylsiloxane (PDMS)[80]. In detail, these studies reveal that resistance versus temperature (R(T)) measurements can highlight the effects produced by glass transition on the microscopic conduction mechanisms. Unfortunately, such measurement requires sometimes a doping procedure, above all in the case of strong insulators. Actually, in this case it is clear that this technique requires also the application high fields, resulting then very invasive. Moreover, the evaluated T_g value can be modified by the presence of dopants and, above all, by their concentration[81,82].

For all these reasons a concrete alternative electrical tool for the evaluation of glass transition temperature in polymeric thin films is represented by the non invasive, practical and precise dielectric relaxation measurements, carried out via IS technique. In few words, using the parallel mode representation, it is possible to record both permittivity and ac conduction as a function of temperature, at a fixed frequency of the applied external varying field. In this way, the relaxation linked to the phase transitions can be displayed as an effect on both the recorded capacitance and conductance. Basically, since such measurement allows to study the local and cooperative chain dynamics of polymers, it is clear that the segmental dynamics, which is referred to as the α-relaxation (in the low and middle frequency regions, up to 10^5 Hz), well reflects the dynamic glass transition. In the next section, the application of such method to a PDMS thin film will be shown and discussed into the framework of the dynamic relaxation of polymeric chains.

2.3.b) ac measurements on dielectric Polydimethylsiloxane; sample preparation; experimental results.

The choice of PDMS as testing material for glass transition evaluation is due to different motivations. The main reason is constituted by the fact that PDMS is recognized as a promising material in many technological applications such as Microfluidics, thanks to its rheological properties, or soft lithography, due to its remarkable mechanical properties, but it is believed promising also in Organic Electronics due to its low dielectric constant value[83]. PDMS, in fact, is a chemically inert, stable material with an high degree of flexibility. Another important aspect which have led to the choice of PDMS is the fact that it is one of the most known Semi-Crystalline polymers, so its phase transition have been already investigated widely (PDMS shows a melting transition located at T_m about 220 K and a glass transition equal to 150 K[84]); for this reason it constitutes a good term of comparison for testing the efficiency of the electrical method which we are going to show.

PDMS simple chemical constituent (Fig.13) is a backbone $[SiO(CH_3)_2]_n$ arranged in a network-like structure, where the Si–O bonds are responsible of the considerable flexibility showed by the polymeric backbone.

The starting point of the analysis concerning the study of phase transitions in PDMS dielectric films is constituted by the fabrication of simple parallel plane plate capacitors, similar to those depicted in Fig.6.b, filled with such material. PDMS thin films, Sylgard 184 purchased by Dow Corning, were spin coated in a clean room on the above mentioned metallic plane plates; in detail, Sylgard 184 is a two-component heat-curing system consisting of one part by weight of curing agent and ten parts of base. The base and the curing agent are mixed in a plastic cup using a plastic spoon for at least a few minutes, depending on the amount of material. After the mixing, the silicone mixture needs to be degassed in vacuum in order to remove air

bubbles incorporated during the mixing phase. When the silicone is completely clear and transparent it is ready to be spin coated. By this procedure, 4-5 μm thick PDMS films have been deposited on glass substrates equipped with silver (Ag) electrodes (deposited by sputter coating technique). In particular, two geometries of plates have been fabricated; the surface A of the manufactured electrodes are 2×10^{-5} m^2 and 9×10^{-6} m^2, respectively. After spinning, the samples were annealed for one hour at 100 °C. Finally, counterelectrodes were deposited by high vacuum thermal evaporation in order to prevent both damages, expected in the case of the most invasive sputtering of Ag atoms, and contaminations (high vacuum guarantees a high level of cleanliness).

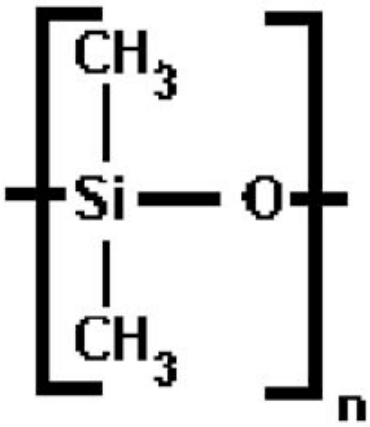

Fig. II. 13: PDMS chemical structure.

In this study, both capacitance and ac conductance have been measured in a RC parallel mode representation at fixed frequencies as a function of temperature, from T_{room} down to 40 K with a cooling rate equal to 5 K/min, and as a function of frequency, in a window ranging from 100 Hz to 1 MHz, at different fixed temperatures below T_{room}, also by applying a dc bias.

A first analysis of material properties has been carried out by comparing the experimental behavior of ac conductivity with the predictions of the UDR model. In Fig 14.a the frequency dependent ac conductivity recorded

in the rubber phase, at a fixed temperature equal to 260°C, also by superimposing a dc bias to the varying field (the amplitude of the varying signal is 100 mV), is reported. In Fig. 14.b a similar measurement, differing only for the environmental temperature fixed at 163K, in the middle of the melting region, is reported.

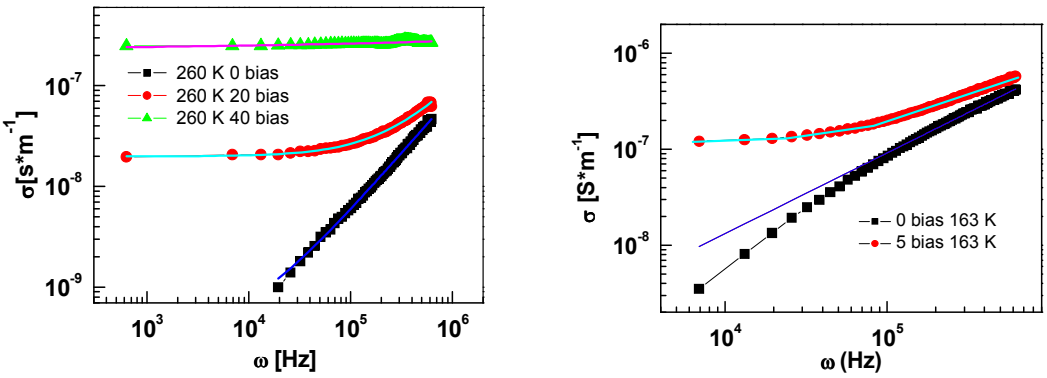

Fig. II. 14: ac conductivity (symbols) vs. frequency recorded at a) 260 °C as a function of three fixed values of dc bias, equal to 0V (■), 20V (●) and 40V (▲) and b) 163 K as a function of dc bias equal to 0V (■) and 5 V (●), are reported, together with the fitting curves (straight lines).

The ac conductivity shows at lower frequencies and high dc bias a crossover to a frequency independent behavior. The value of the index s extracted at 260 K, equal to 0.99 confirms the expected dielectric nature of PDMS in this temperature region, in agreement with the statements of UDR model. Moreover, the value extracted in the melting region, where the growing crystalline phase is expected to increase the electrical conduction, the index s, equal to 0.88, again agrees with the prediction of UDR model, being this value a further confirmation of the increased charge conduction. The permittivity value extracted at room temperature and lower frequencies is 2.4, in agreement with data reported in literature[85].

The phase transition, instead, have been studied by recording simultaneously the capacitance and the ac conductance, this time by fixing the frequency of the applied external field (100 mV of voltage level) at

three different values (that is 300 Hz, 1 KHz and 100 KHz) and by varying the environmental temperature. The capacitance and the relative ac conductance acquired at 1 KHz for a capacitor with a surface of the plates equal to 9×10^{-6} m^2 are reported in Fig. 15.a and 15.b, respectively.

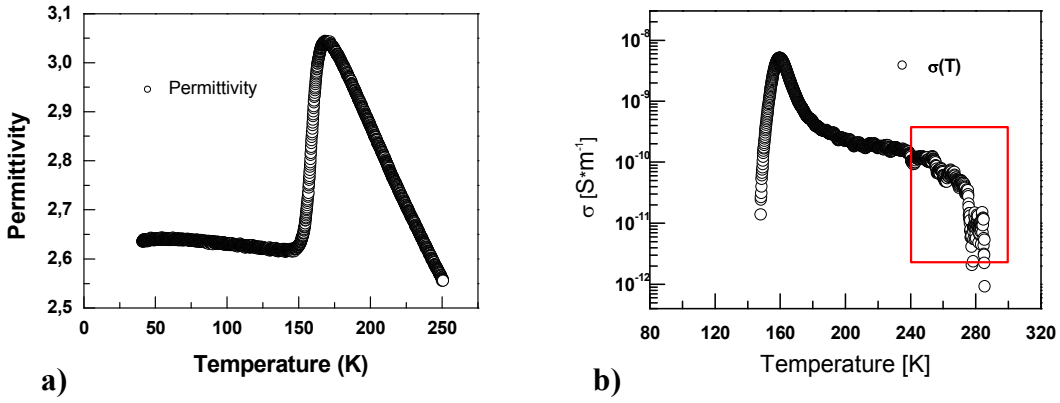

Fig. II. 15: a) Permittivity vs. temperature recorded at 1 KHz and 100 mV of voltage level; b) ac conductivity vs. temperature related to the permittivity displayed in a).

The recorded permittivity ε_r in a restricted temperature range for different fixed frequencies is instead reported in Fig. 16.

$\varepsilon_r(T)$ measurement showed in Fig. 15.a allows the localization of phase transition temperatures. In this respect, if a varying electric field is applied to a dielectric-like polymeric material, its polar groups tend to align with the external field. If glass transition temperature T_g is approached from above, the permittivity is expected to grow for two reasons: the rotation of molecular bonds gets more difficult (as a consequence of the reduction of thermal vibrations) and the thickness of polymeric layer reduces (due to the reduction of the available specific volume). When the external temperature reaches the glass transition region, the permittivity drops because of the freezing of polymeric chains occurred in glassy phase.

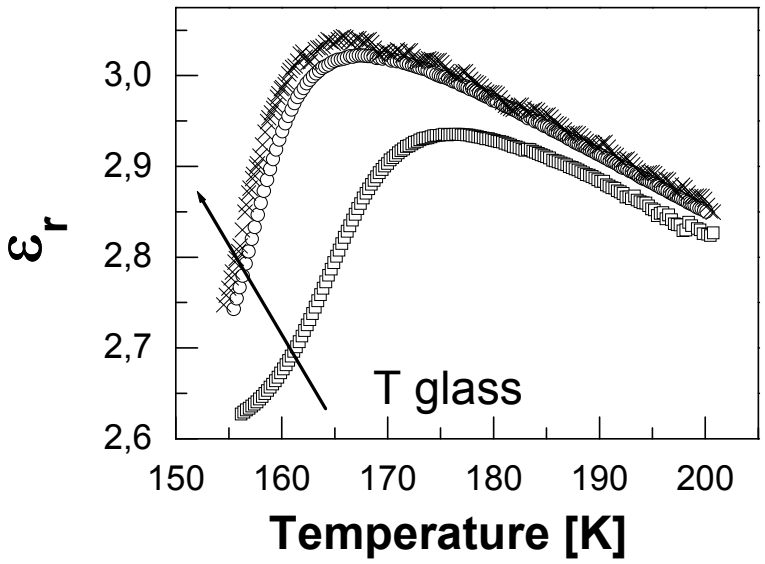

Fig.II.16: Permittivty vs. temperature in a restricted temperature range for three different fixed frequencies, that is 300 Hz (×), 1 KHz (○) and 100 KHz (□).

Below T_g, instead, the available specific volume (where polymeric chains show a non null segmental mobility) is expected to be minimum, since the rotation of the bonds doesn't occur any more (the material is fully hard due to complete freezing of polymeric chains). As a consequence, far below T_g the permittivity results to be constant, tending both to increase when the increased external temperature approaches T_g from below and to decrease again when the material returns in its 'rubberlike' phase, far above T_g (since the regained thermal expansion of the polymeric film, frozen in the glassy phase, increases the thickness of the material, decreasing thus the capacitance). So the glass transition results to be completely reversible once the sense of the varying external temperature is inverted. In this context, the experimental T_g value corresponds to the inflection point displayed by permittivity. Obviously, it is noteworthy that $\sigma(T)$ shows both the phase transitions occurring in the material. In particular, ac conductance reflects in a precise way phase transition and allows to better quantify the temperature values at which such transitions occur. In fact, the maximum value of temperature dependent ac conductivity (maximum of the losses in the material, see Figg. 15.b, 17), corresponds to the T_g value.

This topic can be argued by the fact that the glassy phase is reached in correspondence of a peak in dielectric losses, since the freezing of polymeric chains below T_g has to correspond to a relaxation phenomenon. Moreover, the ac conductance allows a better experimental identification of T_g value since the localization of peaks in losses appear more simple and practical if compared with the determination of the inflection point in permittivity. As far as the melting transition is concerned, it is reasonable to retain that melting temperature T_m corresponds to the change in slope of conductivity, as indicated in Fig. 16.b by the red rectangle. In fact, with the increasing of the relative weight of the crystalline phase in PDMS films, it is expected that both the current flowing into the material increases and the noise related to the measurement of ac current reduces (see Fig.17).

Another crucial feature of glass transition is its frequency dependence. In fact, the black arrow in Fig. 16 shows that the inflection point, that is T_g value, tends to shift towards higher values when the frequency of the applied field is increased. In fact, it is clear that the higher is the frequency of the applied field, the sooner the polar groups are unable to follow the variations of the field; so the peak signaling the "glass transition" is shifted to higher temperatures. Of course, also the peaks in the related ac measurements (Fig.17) experience a shift towards higher temperature values for higher frequencies of the applied field. As far as such dependency is concerned, it is expected on the basis of glass transition phenomenology that the glass transition temperature in the range of frequencies investigated ($\omega>1$) varies approximately with the following logarithmic behavior[72]:

$$T_g(\omega) = T_g^* - \frac{A}{\ln\left(\frac{\omega}{B}\right)}, \qquad (7)$$

where $B>>\omega$. The T_g^* parameter, already cited previously, is the "ideal transition", or static limit, obtained for $\omega \rightarrow 0$. In our case, from the

recorded experimental data a T_g quasistatic value equal to 145 K was extracted, in good agreement with the values reported in literature[84]. The onset of melting transition at lower frequencies of the applied field, instead, is believed to be located at about 225 K, that is in the temperature region in which the slope of ac conductivity changes (this region is delimited by the black line in Fig. 17).

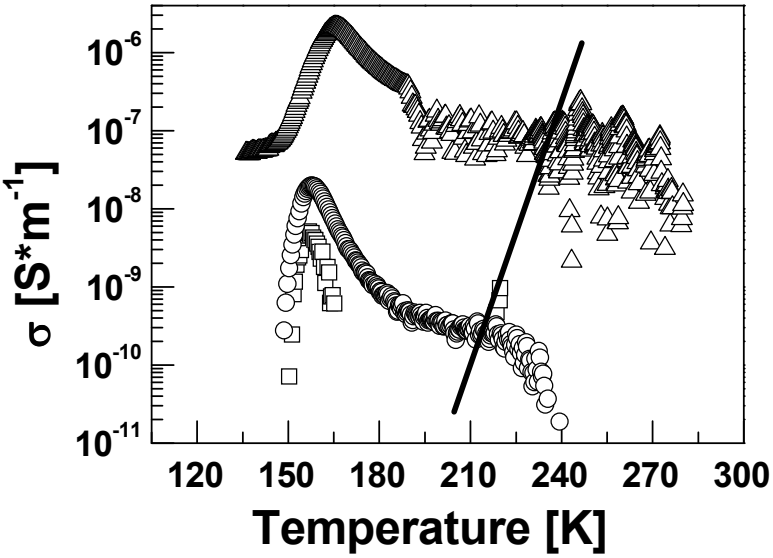

Fig. II.17: Conductivity vs temperature for 4 μm PDMS sample at 300 Hz (□), 1 kHz (○), and 100 kHz (Δ). T_m increases by increasing the frequency of the applied field (black line).

This last result is confirmed also by the frequency dependent measurements showed in Fig. 14, since the application of a dc bias to frequency dependent measurements clarifies this aspect. In fact, the total conductivity can be written in this case as $\sigma_{tot} = \sigma_{dc} + \sigma_{ac}$, where σ_{dc} is the contribution introduced by the applied dc bias. This dc contribution to the overall conductivity can't be detected by performing I-V measurements since it is too low. It is more simple, instead, to determine experimentally σ_{tot} by means of the ac technique. So, σ_{tot} measurements show that the dc bias changes the ac conductivity, particularly in the region of low frequencies of the ac field. Such variation depends on the phase of the material. In fact, just below room temperature (260 K) the effect displayed by superimposing a dc bias of 20 V to the ac field is comparable to that

occurred in the "crystalline phase" under a dc bias of 5 V. This evidence confirms again the increasing of conductivity occurred in such region.

Finally, it is worth to mention here that, as it has widely underlined in the previous section, the conditions of measurement chosen for the T_g evaluation strongly affect the obtained experimental results. In fact, a strong dependence of both the T_g value and the width of the "glass transition zone" on the performed experiment is indicated by the fact the width of the peaks showed by σ(T) measurement in Fig.18, related to the two different geometries chosen for the capacitors and representing the width of the glass transition zone, differs in the analyzed configurations.

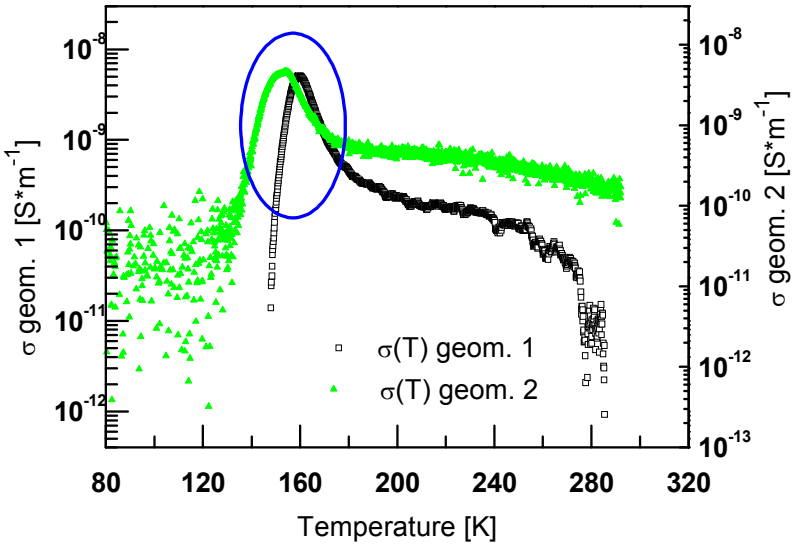

Fig. II.18: Conductivity vs temperature for a fixed ac field (1 kHz and 100 mV of voltage level) performed on capacitive cells having the following geometries (*S*×*d*): 9 mm^2×4 µm (▲) and 20 mm$^{2\times}$5 µm (□). The glassy region is indicated with a circle.

Probably this difference is linked to the fact that the local heating due to the electrical power dissipated through the dielectric films is different for the samples in analysis. This trend can be confirmed also by the fact that the loss peak (corresponding to the T_g value) occurs at higher temperatures if compared with the sample, characterized by a smaller geometrical factor, that is a lower current. It is then clear that such criterion allows to monitor

the glass transition temperature dependence on film dimensions and, if believed useful, also the interactions with the substrate.

In conclusion, the results obtained by means of IS techniques and the features of the performed measurements can be summarized as follows:

- The nature of the analyzed material, i.e. PDMS, has been clarified by means of UDR model.
- The phase transitions occurring in such material are displayed in a non invasive way by detecting the relaxation induced by the same transitions.
- The dependence of glass transition evaluation on the experimental conditions resulted evident from the performed measurements; in particular, a frequency dependent behavior has been assessed for Tg evaluation by means of external varying fields and a dependence on geometrical factors has been noticed.
- The high degree of sensitivity reached by this method is directly connected with the sensitivity of ac measurements, allowing to measure capacitance and conductance with a resolution of 0.1 pF and 10^{-10} S, respectively (allowing a tolerance in measurements equal to 0.3%).

Chapter III

ac electrical characterization of organic devices.

3.1) ac measurements on electronic devices: bulk properties.

Organic based devices are in general very complex systems, also in the case of the simplest conceivable device structure. In fact, a simple organic device is macroscopically composed in its basic layout by an active organic layer and at least two interfaces (metal/organic/metal heterojunctions). Actually, focusing the attention on the microscopic features of such devices, further interfaces can be distinguished if the organic materials employed as active device layer are composed by small molecules and oligomers. As a matter of fact, in this case we can distinguish between injecting macroscopic interfaces (that is metal/organic heterojunctions) and microscopic interfacial defects. In particular, in this latter case the interfaces are constituted by grain boundaries, step-like islands or interfaces separating two adjacent organic layers, according to both the nature of the material and the conditions chosen for thin film deposition. The presence of these discontinuities suggests the arising of several local effects that act cooperatively into the economy of device operation. So these interfacial local effects have to be investigated necessarily by recurring to experimental techniques able to shed light on the different local contributions participating to the overall device operation. Moreover, such techniques have to satisfy another important requirement: in fact they have to be able to detect also those effects played by the cooperative dynamics of macromolecules composing the organic material in the context of device working mechanisms. By the way, in chapter II IS has proved to be a very powerful tool for the investigation of local properties affecting the macroscopic nature showed by organics. Following such direction, it is reasonable to think that the extension of the IS analysis to device structures can furnish a fundamental tool in order to discern the role played by the different parts forming the whole device structure. Of course, as just discussed in chapter I, it is required that IS has

to be carried out by performing ac measurements by choosing the opportune experimental conditions (that is by identifying the frequency window in which the bulk or the interfaces are probed).

In this section, the ac technique will be extended to those structures in which the role of the active organic thin film is reasonably retained predominant in terms of device operation. In detail, both a humidity sensor, based on a novel, promising polymeric material, and a bilayer light emitting device, assembled by using a very common organic heterojunction, are studied by means of ac technique with the aim of understanding in which manner the employed materials contribute to both device working (in the case of the sensor) and degradation (in the case of the OLED). In particular, the analysis is aimed to clarify with a non invasive technique the effect of structural phase transitions on device working, being however such effect not necessarily destructive.

3.1.a) ac measurements on polysilsequioxanic-based humidity sensors: device manufacturing and dc operating properties.

There is a wide production regarding the employment of polymeric materials in the field of sensing[86]. The sensing properties of long chain based organic materials are guaranteed by the structural properties resulting from the typical interchain interactions which sustain their solid state. More precisely, polymers used as active layers in sensing devices, generally experience the effects of the analytes which have to be detected as a consequence of the arising of an active interaction with such external agents. The detection is based on the change of material properties induced by the above mentioned interaction. In this respect, organic sensors require in most cases the use of conducting active layers that are able to change their intrinsic electric response[87]. Indeed, also organics films which can induce variations on the charge transport properties showed by transducers

integrated with them can be used, as happens for example in the case of bi-layer configurations[88], where the first organic serves as active interacting layer and the second one works as transducer element. In this respect, the use of both conducting materials and active insulators in which a conducting network can be integrated is needed[89]. Of course organics allow the sensing of chemical species in form of gases[90] and external environmental agents such as humidity[91]. Moreover, a strong requirement for a practical application of organic materials is represented by the selectivity, that is a particular property that has to guarantee an efficient sensing of the desired species in presence of other possible analytes, searched for by recurring to the preparation of novel materials[92]. This aspect represents a basilar topic in the context of the development of novel materials, able to satisfy the contemporary request of an efficient response and a selective sensing.

Among the most promising materials developed for this purpose, polyhedral organosilsesquioxanes (POSS) are gaining an increasing interest due to their particularly marked properties in humidity hosting. The general formula of POSS composites (where the octahedral form (n=8), that is the poly-(propylmethacryl-heptaisobutyl-POSS)-co-(N-butylmethacrylate), reported in Fig.1, is considered in such study) is $[RSiO_{3/2}]$, consisting in a central core, long about 0.53nm, with organic groups R on the corner. Its chemical structure is often cage-like with various reactive and non-reactive chemical functional groups on the surface. Such composite can be easily functionalized in order to obtain main chain or side-chain hybrid polymers with a complete control of the material structure and properties, such as porosity[93] or high thermal[94] and mechanical[95] stability. In particular, functionalization allows to obtain hybrid polymers characterized by good performances in relative humidity sensing[96].

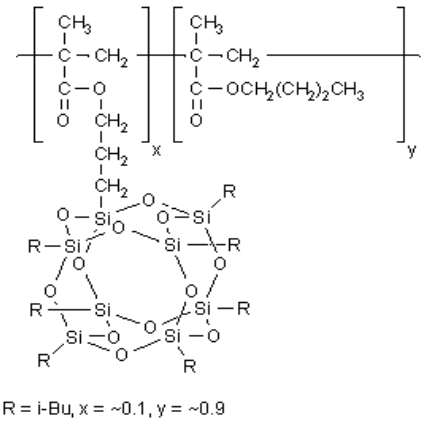

Fig.III.10: Poly (propylmethacryl-heptaisobutyl-POSS)-co-(N-butylmethacrylate) chemical structure.

In this scenario, on the basis of the topics concerning the IS technique, an analysis of the working mechanism of POSS based sensing devices via ac measurements seems to be appropriate for better clarify the effects produced on device working mechanisms by an expected glass transition in device operating temperature range.

First of all, prior to enter into details of ac analysis, the sensing properties of the commercial (propylmethacryl–heptaisobutyl-POSS)- co- (N-butylmethacrylate), purchased by Sigma Aldrich, with a POSS cage content of 15% and 25% in weight have been tested on thin films deposited by means of spin coating technique on glass substrates with an interdigitated architecture of the injecting gold contacts (3000Å thick, deposited by e-gun evaporation technique). In this case, spin coating has been carried out by dissolving the powders of such material in tetrahydrofuran (THF). The solution has then spun on the rotating substrate with a spin speed of 4000 rpm, resulting thus 500 nm thick films.

The sensing response has been monitored in a homemade Gas Sensor Characterization System (GSCS), a system in which it is possible to simulate the desired atmospheric conditions, also in presence of some mixtures of gases. Here the system has been used for varying the relative humidity percentage keeping the environmental temperature fixed at 20 °C. Anyhow, POSS based devices with 15 % of cage content have

evidenced a very good dynamic response in function of different steps of humidity (Fig.2); the 25% based devices resulted instead less performing. The strong increasing of conductivity in presence of humidity, covering many orders of magnitude, indicates that a porous mechanism rules the device working, unlike happens in other polymer based sensors, where the conductivity tends to decrease as a consequence of the polymer swelling in presence oh humidity. In fact, a network of pores is formed in polymeric material, being such pores delimited by amphiphilic silsesquioxanic cages (in ref. 11 the SEM images of such material in presence of some induced fillers, aimed to obtain a conducting nanocomposite with high sensitivity versus external atmosphere, show the pores delimited by the silsesquioxanic cages). In this context, the increase of conductivity can be addressed to the presence of water molecules inside the pores, since the increasing of conductivity can be explained in terms of a promotion of a charge transfer mechanism among the cages, due to the creation of a hydrogen bond network. This mechanism is also consistent with the observation of some features related to the analyzed devices, such as the response quickness, the very high sensitivity and the performance in the full RH% range, generally unexpected in the case of polymer-based sensors. Moreover, the influence of the cage content on device response can confirm this idea, since it is believed that the a minor content of rigid silsesquioxanic cages in 15% based films determines a major volume of pores and a more simple motion of these cages, leading to the water molecules to be hosted more efficiently.

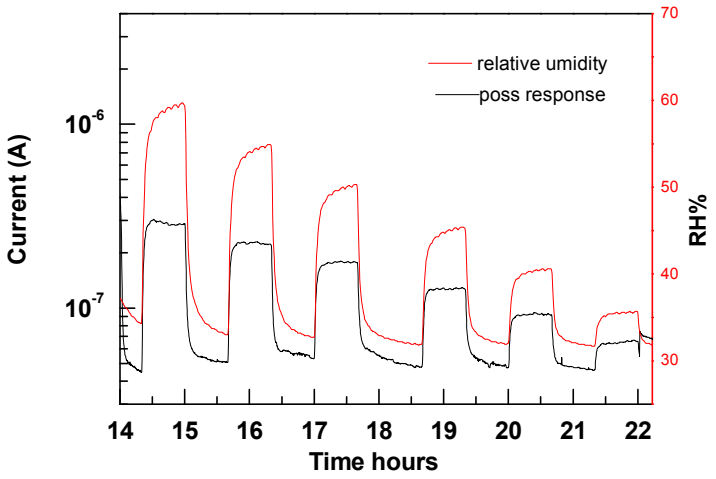

Fig. III.11: 15% POSS based sensors typical dynamic response as a function of different steps of humidity. The red line shows the relative humidity percentage in the chamber measured with a commercial humidity probe sensor.

On the basis of the preliminary dc characterization, the good response associated to POSS based humidity sensors has been assessed. However, as stated above, preliminary studies concerning the evaluation of glass transition have indicated the possibility that the material experiences such transition around the device operating temperature. The eventual role of T_g can be revealed by performing ac measurements as a function of temperature.

3.1.b) ac measurements on polysilsequioxanic-based humidity sensors: experimental results; effect of the glass transition on device working mechanisms.

The ac electrical characterization has been performed on devices with a sandwich like structure (parallel plate capacitors). The thickness of polysilesquioxanic films ranged from 250 nm to 800 nm, being such thicknesses typically employed for manufacturing the active polymeric layers in sensing devices, while the surface of the thermally evaporated Ag electrodes was 9 mm^2 or 0.3 mm^2 (3 mm × 3 mm and 100 μm × 3 mm,

respectively). Both frequency dependent (at room temperature) and temperature dependent (at a fixed frequency of the applied field) capacitance C and conductance G have been measured in the parallel RC mode representation. In particular, temperature dependent measurements at 100 Hz and 1 KHz have been performed by warming the samples up to 360 K, while the frequency dependent characterization has been performed by sweeping the frequency of the low amplitude applied field (0.1 ÷ 1V) in the range 100 Hz ÷ 100 KHz.

The experimental results regarding the frequency dependent measurements, reported in Fig.3.a, confirm the dielectric nature of 25% POSS based devices (the material is a low-k dielectric with $k=\varepsilon_r=1.2$ at lower frequencies). In fact, the UDR model well fits the observed behavior: the index s extracted by the fitting procedure is close to unity in the region of low and middle frequencies (s~1 is typical for dielectrics). For the samples with a POSS cage content of 15% in weight, the frequency dependent measurements reported in Fig.3.b have shown a different behaviour with respect the 25% ones. Such difference reflects the more conductive state of 15% POSS based samples, as indicated by preliminary dc measurements. This aspect is also deductible by the higher ac conductivity recorded for these 15% POSS based samples (10^{-6} -10^{-4} $S*m^{-1}$, in agreement with the dc value of conductivity, versus 10^{-9}-10^{-8} $S*m^{-1}$ recorded in the case of 25% POSS based samples). In fact, both permittivity and conductivity show an irregular non monotonic behaviour in the analysed region of frequencies. Moreover, in this case UDR model is not able to furnish any additional information on the microscopic nature of conduction, as generally happens in the case of materials with a hopping like conduction mechanism. This evidence can be viewed as a confirmation that the charge transfer assisted by the network of hydrogen bridges can be proposed with good reason as the basic charge conduction mechanism in highly conducting 15% POSS based films.

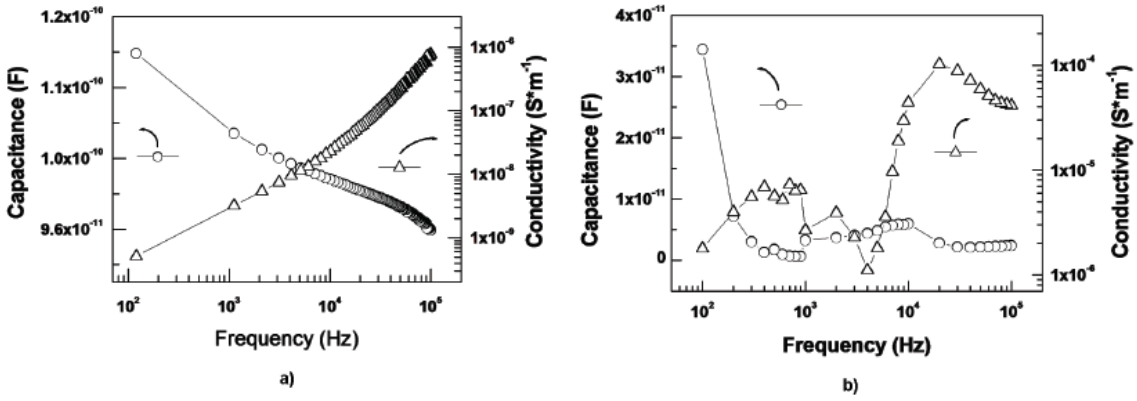

Fig. III.12: a) Capacitance (○) and ac conductivity (Δ) versus frequency for samples with a content in weight of cages equal to 25%, recorded in air at room temperature and; b) analogous measurement for 25% POSS based samples. The capacitance and conductivity are again indicated with the symbols (○) and (Δ), respectively.

As already introduced above, the temperature dependent measurements have been performed by recording permittivity and its related losses, both at 100 Hz and 1 KHz, by warming the samples from T room up to about 360K (in Fig. 4 are reported the measurements performed on a sample with a POSS cage content equal to 25%).

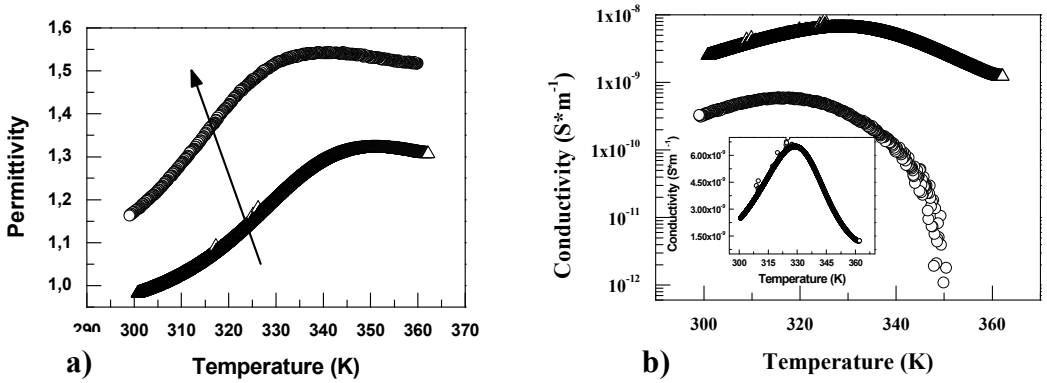

Fig. III.13: Permittivity (a) and conductivity (b) vs. temperature recorded at fixed frequencies, equal to 100 Hz (○) and 1 KHz (Δ), with a field amplitude equal to 0.1 V for 25 % POSS film. The inset in fig. b) shows the peak at 100 Hz in a linear scale. The black arrow in fig.a) shows the expected frequency dependence of T_g value (see Chapter II).

Analogous measurement for a sample with a cage content of 15%, performed by fixing the frequency of the varying field at 100 KHz, is reported in Fig. 5.

In fig 4.a), the expected frequency dependent behaviour of T_g [$T_g(\omega)=T_g^*-A/[\ln(\omega/B)]$, with $B>>\omega$][97] is evidenced by the black arrow. In this case, it has been obtained a stronger frequency dependent glass transition temperature compared to the one displayed by Polydimethylsiloxane (PDMS).

As far as the value of glass transition temperature is concerned, in the first case, a T_g value of about 320 K, just above room temperature, has been evaluated at 1KHz.

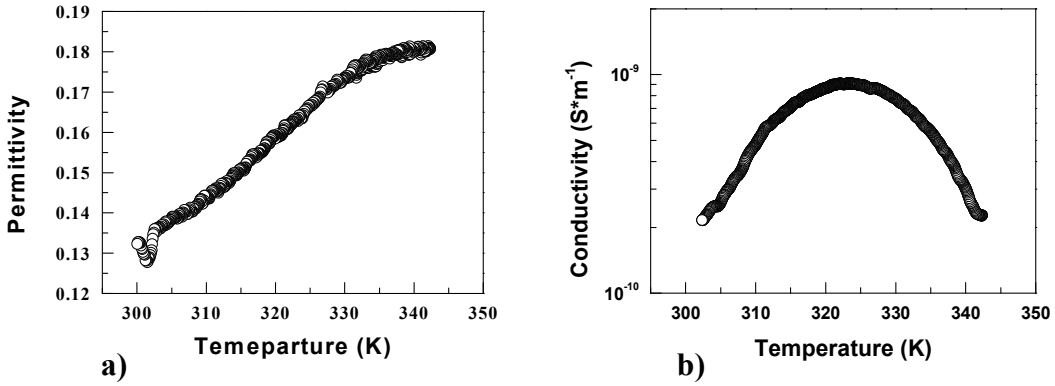

Fig. III.14: Permittivity (a) and conductivity (b) vs. temperature recorded at 100 KHz with a field amplitude equal to 0.1 V for 15 % POSS film.

The T_g value obtained by the measurement performed on 15% POSS based device at 1KHz (not reported here) is indeed a little bit higher and less frequency dependent with respect the previous one. This analysis evidences that some differences arise between the two different types of samples. This trend is expected on the basis of the fact that glass transition is a dynamic phase transition (characterized by a wide temperature region in which the structural changes gradually occur). So, for this reason it can be influenced by the film morphology. In this case it has been observed that the more is the cage content the lower is the onset of the glass transition region, showing thus an influence of the increasing size of inter-cage pores on the growing of T_g.

Since the architecture of sensing devices is based on gold interdigitated contacts, the analysis has been operated also on such device structures. In

this way the exact device layout has been tested in order to exclude the influence of film thickness and device architecture on the extracted T_g value. The experimental results, not reported here, have confirmed the location of a glass transition at about 320 K.

By way of summary, the assessment of T_g value just above room temperature indicates a partially fluid behaviour occurring in device operating temperature range. This occurrence involves for sure a more simple motion of POSS cages that, on its turn, could determine the above mentioned porous framework in which water molecules are able to host in a simple way, eventually creating those hydrogen bonds among cages retained responsible of charge transport. So, in this case it is reasonable that the hosting of water molecules and the subsequent arising of the conducting network of hydrogen bonds can be sustained by the gained fluidity of the material.

3.1.c) ac measurements on conventional ITO/TPD:Alq_3/Al light emitting diode: study of the electro-optical degradation mechanisms.

Many studies have been reported about the correlation between the glass transition and the degradation of OLEDs[98]. In general, it is a matter of fact that the analysis of the effects induced by the glass transition on devices in operational conditions is remarkably difficult[99]. The understanding of device intrinsic degradation dependence on temperature is essential for OLED commercial applications. So, temperature dependent studies can have a decisive impact in establishing the critical temperature for device failure since, as it has been argued, the higher is the current flow inside the device (i.e high current density), the faster is the performance degradation because of the current induced device heating (self-heating). Of course, by highlighting the degradation induced by the increase of temperature it is possible to devise some strategies useful for overcoming the device

limitations. The main problem in implementing such studies lies in the fact that the degradation is linked to structural transitions occurring in the organic active layers, that is to glass transition, so, as it has been widely underlined in the previous chapter, it is very difficult to localize exactly the temperature value at which degradation occurs, that is T_g. The strong dependence of such important parameter on both experimental tools used for its evaluation and device architecture (with a special reference to the thickness of the active layer[100]) of course represents the main source of difficulty in its operational evaluation.

Ac measurements again can facilitate this task, since they allow to locate the glass transition region directly on the desired structures during device operation. This aspect is of paramount importance, since it is clear that the glass transition can be probed in this way also in the meanwhile a dc current passes trough the device, eventually turning on it. This means that the experiment can be carried out by a non invasive electric criterion as near the actual device working condition it is possible, reducing then the possible fluctuations on T_g evaluation which may be induced by other invasive techniques. Moreover, ac measurements can be viewed also as a direct tool for monitoring in which manner the thickness of the analyzed sample affects the glass transition. This aspect is very important, since by varying the thickness of the sample the T_g value can be modified; in particular it is possible to shift T_g towards lower values by reducing the thickness[101]. In this respect, combining this effect with the requirement of an acceptable efficiency of emission, it is possible to overcome the problems in device working induced by a possible degradation of the active emitting layers, what's more guaranteeing at the same time a good emitting efficiency.

In this section, the IS technique is employed on a conventional ITO/TPD-Alq_3/Al green light emitting device in order to show the powerfulness of the technique in addressing the degradation of the device to the occurrence

of the glassy phase transition in N,N'-Bis(3-methylphenyl)-N,N'-diphenylbenzidine (TPD, Fig.6.a)).

In detail, 100 nm thick of TPD (acting as Hole-Transport Layer, HTL) and 60 nm of Alq_3 (Aluminum tris(8-hydroxyquinoline, the Electron-Transport Layer)) have been evaporated in series, at a rate of 1÷ 2 Å/s, on a Corning 1737 glass substrate, with 150 nm thick commercial ITO (indium tin oxide) layer as anode. Then, an aluminum cathode has been thermally evaporated on the top of Alq_3. The reference to the ITO/TPD-Alq_3/Al structure founds its justification in the possibility of comparing the experimental results with the features reported in literature of this very common structure. In particular, Alq_3 (Fig. 6.b) consists of one aluminum ion (Al^{3+}) and three 8-hydroxyquinoline molecules in which one nitrogen atom and one oxygen ion for each ligand coordinates the Al^{3+} ion with a pseudo-octahedral structure. The electronic structure of Al^{3+} is $1s^2 2s^2 2p^6$, similar to that of an inert gas atom, leading to the Alq_3 high stability in dry atmosphere.

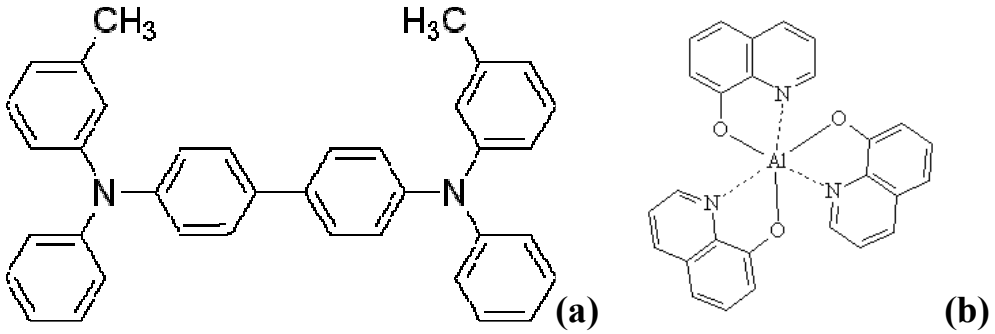

Fig. III.15: TPD (a) and Alq3 (b) chemical structures.

Moreover, TPD has been selected for its low glass transition temperature, so it is easy to evaluate the HTL morphology change and its influence on the device behavior without damaging the emitting Alq_3 layer (recombination and the following emission occur in the ETL).

Preliminarily, the optical (irradiance) and the electrical (I-V) detriment of device due to voltage scan has been monitored in function of substrate temperature (recorded by monitoring the infrared IR emission) (Fig. 7). It

is clear that optical detriment starts before the electrical one. As it has been reported in literature[102], at high voltages, approaching the optical failure voltage the electrical stress produces a significant increase of hole traps near the HTL/ETL interface. Such traps act as recombination centres with a largely non-radiative behaviour, so an evident reduction of electroluminescence (EL) is measured in a temperature range starting from 340 K. Such effect can be linked to the self-heating and the related reaching of the glass transition region in TPD.

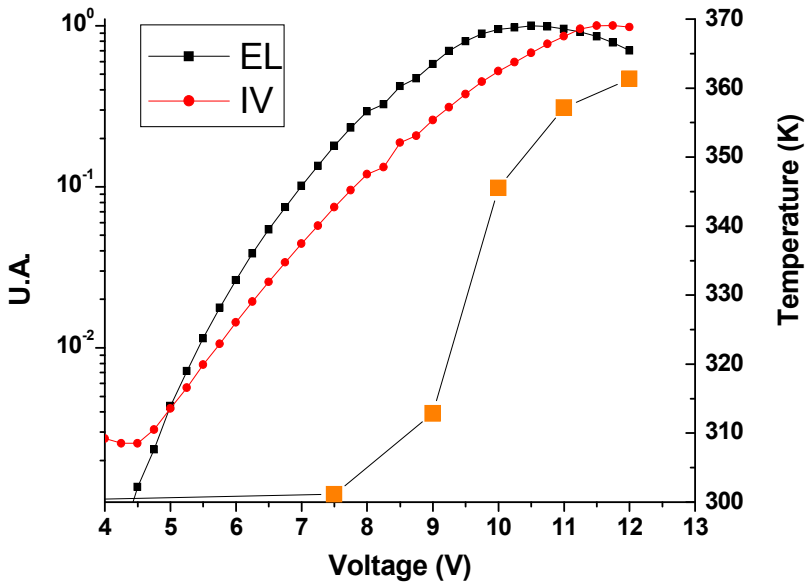

Fig.III.7: Optical (electroluminescence in arbitrary unities vs. Voltage) and electrical (current in arbitrary unities vs. voltage) device detriment. The temperature due to self-heating is monitored by an IR camera from the bottom of the substrate.

This topic has been effectively confirmed by the ac measurements carried out in function of temperature, from about 300K (room temperature) up to 350K, by applying a field at 100 mV of voltage level and 1 KHz of frequency (Fig. 8).

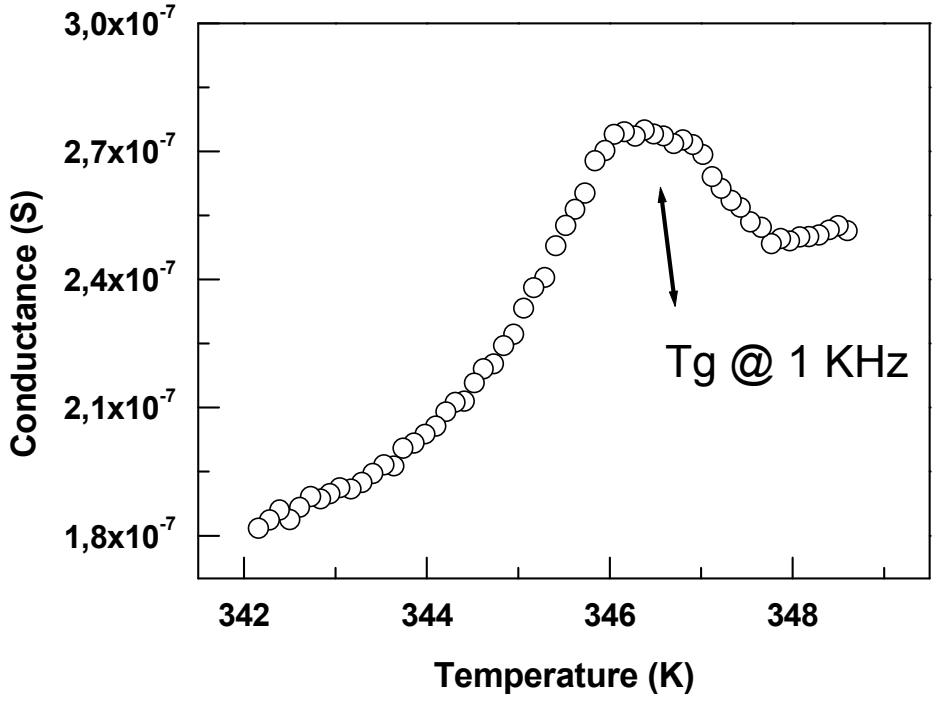

Fig.III.8: ac conductance vs. temperature recorded on ITO/TPD-Alq3/Al device (ac field at 0.1 V level and 1KHz of frequency).

The ac measurement shows in fact that 340 K about corresponds to the onset of the glass transition region. So the self-heating of the device provokes the glass transition of TPD. In this context, it is possible that on one hand the fluid like structural features of TPD can still favor a residual overall charge conduction but, on the other hand, for sure this fluidity alters the radiative decay of excitons.

3.2) ac measurements on electronic devices: interfacial properties.

The local character of ac measurements has been demonstrated useful to shed light on the features of organic materials. Also devices can benefit from this important aspect, since it has been showed in the pervious sections that the effects of material properties can be exploited for an exhaustive comprehension of device overall working mechanisms and limitations. In Chapter I the choice of opportune conditions has been underlined to be suitable for extending the IS techniques to the study of individual contributions given by the different parts composing a device in the bosom of its overall response. In this respect, the parallel mode representation has been depicted as a very sensitive tool for extrapolating the effect of interfacial contributions in the context of measurements regarding the frequency dependent behavior of the couple capacitance-conductance, recorded in a wide window of the field frequencies. In particular, at higher frequencies it is expected to be possible to restrict the action of the varying field to the hybrid interface constituted by an organic material and an inorganic injecting electrode. In this context, ac measurements can furnish very important information on the role played by such a kind of interface in many device applications, being in general this role limitative, as happens in the case of light emitting devices. In truth, there are some applications in which interfaces play an active role into the economy of device working, as happens in the case of Organic Spin Valves (OSVs). In this respect, in the next sections such aspect will be showed in a detailed way: IS spectroscopy technique will be employed for recording the response of hybrid manganite/organic material structures and an equivalent circuital scheme of the device will be used in order to study the crucial active role of the manganite/organic interface in OSVs operation.

3.2.a) ac measurements on organic Spin Valves: remind to operating properties, device manufacturing and experimental details.

OSVs are very fascinating devices in which the combination of the highly spin polarized manganite LSMO (lanthanum strontium manganese oxide) and organic semiconductors, together with the employment of another ferromagnetic electrode (usually cobalt), exhibit a spin valve effect as a function of the electrode magnetization orientation. So, organic spintronic devices show a magnetic field (**B**) induced modulation of the current flowing into the organic layer, fairly considerable in the region of low temperatures (spin valve effect). The magnetoresistive effect is responsible of the control of electrical current flowing inside the organic material. Such current can be viewed as the superposition of two contributions: the first contribution is constituted by the movement of injected charge carriers and the second one is linked to the spins injected at the LSMO/organic interface. So, at cryogenic temperatures and for low magnetic fields, it is possible to control the spin alignment inside the device, thus modulating the overall current in it. Magnetoresistance (MR) values up to some tens per cent have been demonstrated[103,104]. In particular, in ref. 18 a 40 % change in the electrical current flowing (GMR effect, giant magnetoresistance) has been demonstrated while in ref. 19 the magnetoresistive response has been demonstrated also at room temperature. The spin alignment during the movement of electrons through the semiconductor has been addressed to the long spin relaxation times, favored by the weak spin-orbit interaction in organics (low atomic number Z)[105].

Since a negative magnetoresistive effect has been found at high magnetic fields (B > 1Tesla) also in LSMO based organic diodes with a non ferromagnetic metallic counter-electrode (aluminum) as top electrode, IS

technique will be used here in order to study the nature of this type of interface. In fact, this further evidence indicates that the spin polarized manganite/organic semiconductor interface is crucial for spin injection. In particular, the study regards the acquiring of complex impedance spectra of a LSMO/Alq_3/Al diode in a frequency window ranging from 20 Hz to 1 MHz by varying also the temperature, from 35K to 292K. A comparison with the results obtained in the parallel mode representation on a conventional ITO/Alq_3/Al diode will be reported in order to discriminate the eventual effect of the LSMO/Alq_3 interface. In fact, the ITO/Alq_3 interface has been widely discussed in literature in order to analyze Alq_3 properties[106,107], so it represents a good reference to evidence the features of the LSMO/Alq_3 interface.

The LSMO based samples have been manufactured on commercial single crystal oxide substrates (i.e. STO, strontium titanate) with 30-40 nm thick LSMO films deposited by pulsed electron deposition (pulsed plasma enhanced configuration, PPD) using a shadow mask with a width approximately equal to 1mm. LSMO grown using PPD has been widely studied in literature; Curie temperature T_c is reported[108] to be about 340 K while room temperature conductivity is 10^2 $S*cm^{-1}$. Moreover, the magnetic properties of LSMO have been checked with Magneto-Optical Kerr Effect (MOKE), founding in this way a complete agreement with literature. ITO based devices instead have been deposited on commercial glass substrates covered with ITO patterned electrodes (d=120nm), respectively. Before to proceed with Alq_3 evaporation, operated simultaneously on a couple of LSMO and ITO based substrates, both a cleaning procedure, consisting in a rinse in acetone and a following ultrasonic bath in isopropanol, and an annealing treatment, aimed to remove surface carbon contamination and to restore the oxygen stoichiometry in LSMO, have been adopted. The Alq_3 deposition has been carried out by thermal evaporation at 10^{-8} mbar with growth rate of 0.1-0.2

Å/sec. 60 nm of Al contacts have been finally evaporated on the top of Alq_3 films using a shadow mask a with width of 1mm, obtaining a crossbar structure (i.e. a capacitor) with a surface a equal to 1mm×1mm (Fig.9).

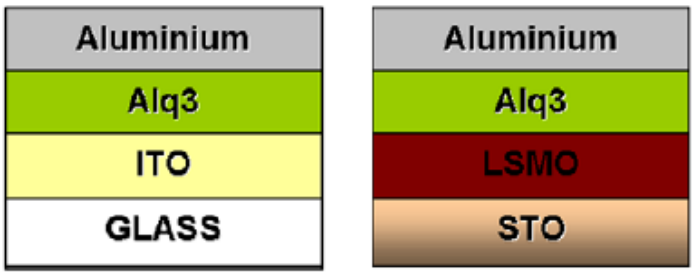

Fig.III.9: Analyzed device structures. A cross configuration of electric contacts has been adopted (plate plane capacitors).

3.2.b) Comparison between ITO/Alq_3 and LSMO/Alq_3 interfaces: role of the manganite on magnetoresistive effect.

The room temperature ac measurements have been performed using a low amplitude varying field (100 mV), that is in the well known Injection Limited Current regime where usually magnetoresistance phenomena (spin injection) are investigated. In this way, the current flowing into the device is completely controlled by the injection mechanisms[109]. Room temperature real and imaginary parts (R(f) and X(f), respectively) of the complex impedance Z(f)=R(f)+jX(f) for two typical ITO/Alq3/Al and LSMO/ALq3/Al structures are shown in Figs. 10, 11, respectively. In Fig. 9 a log-log Nyqvist plot [-X(f) vs. R(f)] is reported as inset.

Before to enter into the analytic details of the recorded spectra, an unusual aspect related to the measurement of both Alq_3 dielectric constant at lower frequencies and low frequency conductance has to be underlined. In fact, the analyzed LSMO and the ITO based samples show different values of dielectric constant (for ITO devices ε_r falls in the range 1.9-2.1, while for LSMO devices ε_r varies from 3.1 to 4.3), but also different low frequency conductance values. These results, already reported in literature, can be explained on the basis of many possible mechanisms, such as hysteretic

effects, thin aluminum oxide on the cathode, formation of conducting pathways due to aluminum inclusions or trapping charges at the injecting interface. As a matter of fact, despite the above mentioned differences, a common feature characterizes the response recorded on a wide window of frequencies.

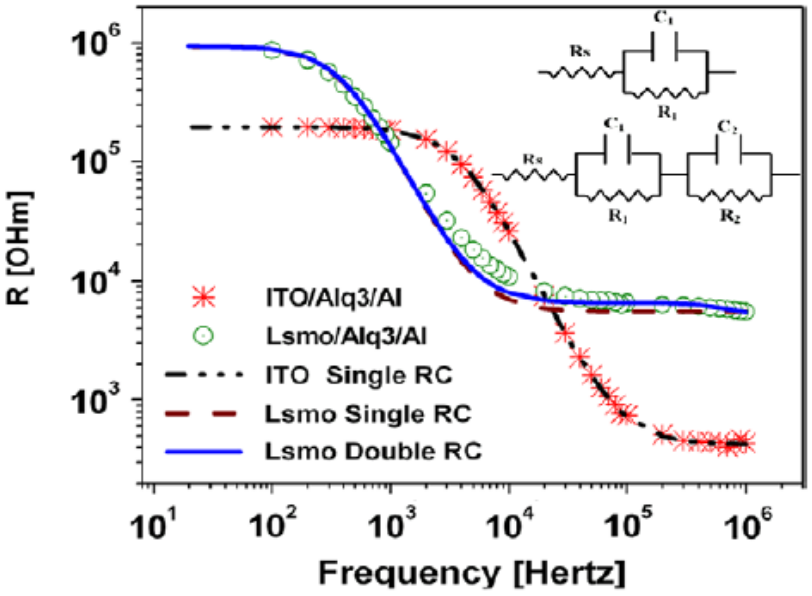

Fig. III.10: Real part of complex impedance for ITO and LSMO based devices. In the plot are reported also the fitting curves obtained using the equivalent circuits in parallel mode representation [ITO single RC (—– – –), LSMO single RC (– – –) and double RC (———), depicted in the inset].

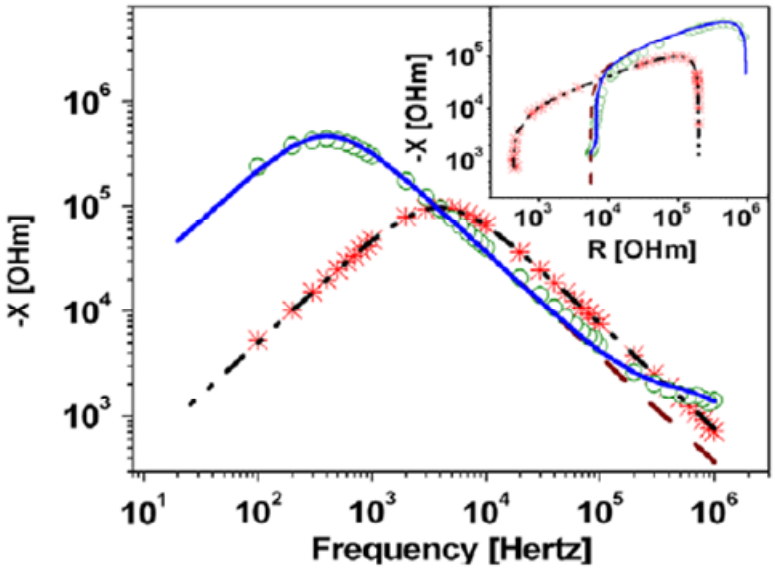

Fig. III.11: Imaginary part of complex impedance for ITO and LSMO based devices and related fitting curves. In the inset a log-log Nyqvist plot is reported.

In fact, the real part R(f) of the complex impedance is frequency independent al lower frequencies for both samples (Fig. 10), then R(f) begins to decrease with frequency. The corresponding -3 dB cut-off frequencies are 400 Hz and 3.5 KHz for LSMO and ITO based devices, respectively. These differences are also reflected in the position of local maxima in imaginary part X(f) of the spectra. In the context of the equivalent circuit reported in the inset of Fig. 10, the non zero R(f) at high frequencies reveals the necessity of adopting a series resistance R_s which accounts of the metallic nature of injecting electrodes. For ITO such resistance has been estimated to be 300 Ω, while for LSMO its value resulted higher (about 5 KΩ). This difference in R_s values can be ascribed, for comparison, to the peculiar characteristic of the junction formed by LSMO and Alq_3. For better enlighten such peculiarity, the equivalent circuits in the inset in Fig. 10 have been considered to fit the experimental impedance measurements. As shown, the ITO device ac response is well fitted by a single circuit, involving a parallel resistor R_1 and a capacitor C_1 with the R_s resistor in series, being such behavior waited on the basis of studies existing in literature. In this case, R_1 (affecting the R(f) value at low frequencies) is about 200 KΩ and the extracted equivalent conductivity (4×10^{-9} S/cm) is very close to the data reported elsewhere[22]. On the contrary, the single RC circuit is not suitable for describing the measurements extracted for LSMO/Alq_3/Al devices. In fact, this structure shows peculiar behavior around 100 KHz, consisting in a slope change above such frequency value. In this case, the employment of an extra R_2C_2 component to the above discussed equivalent circuit improves considerably the fitting procedure (see the continuous fitting line) without involving an interaction with the R_s series. Quantitatively, the extracted resistance R_2 for the analyzed samples is 1.5KΩ, while the extra capacitive element C_2 ranges between 180 pF and 210 pF. By comparison with the

ITO device, it comes out the conclusion that the R_2C_2 component has to be attributed to the specific electrical properties of the interface region between LSMO and Alq_3. So an exhaustive explanation about the origin of this R_2C_2 extra term, accounting of the fact that ITO and LSMO form considerably different interface regions with Alq_3, is required. In this respect, although the values of the work function for both the material are reported to be in practice equal (4.8-4.9eV), actually, as reported in literature[110], X-ray (XPS) and ultraviolet (UPS) photoemission spectroscopy have evidenced the occurrence of a significant vacuum level shift, equal to 0.9 eV, between LSMO and Alq_3. This evidence indicates the presence of a strong interface dipole at LSMO/Alq_3 interface. ITO/Alq_3 instead show a much lower dipole strength, that is a mismatching of only 0.1 eV, with respect LSMO based interfaces. The physical origin of interface dipoles is still under debate; many intrinsic factors such as charge transfer, orientation of permanent dipoles and band bending, have been invoked to provide an explanation for this phenomenon[111]. To this regard, as far as Alq_3 is concerned, the specific polar properties of the molecule have usually been cited to justify its widespread capability to produce interface dipoles. But, recent studies have induced to believe that a density of intermediate states, energetically localized between the electrode Fermi level (that is, the work function) and the Alq_3 LUMO, is induced by the presence of the interface local dipoles[112]. This occurrence has been demonstrated to strongly affect the charge injection process in the related devices. In this scenario, the R_2C_2 extra term can be viewed with good reason as the electrical representation of the interface charge distribution and the consequent local field related to the interfacial dipole. This result is of paramount importance, since reflects the powerfulness of ac conductivity measurements as a new way of investigating deeply the physics of hybrid interfaces. Of course, further research is needed to develop this general theoretical framework. Ac measurements performed

as a function of temperature can give indeed a further contribution towards the understanding of the dipole formation. In this respect, the real (Fig.12) and imaginary (Fig.13) parts of the impedance spectra have been recorded at different temperatures between 295 K and 35 K.

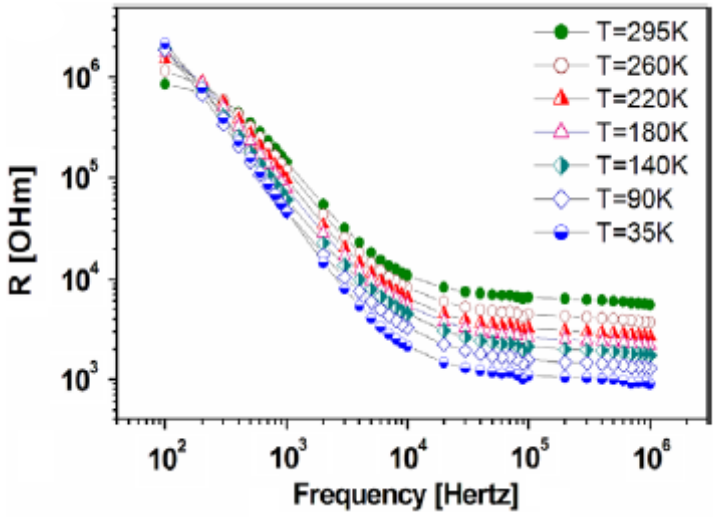

Fig. III.12: Real part of the complex impedance spectra recorded at several fixed temperatures

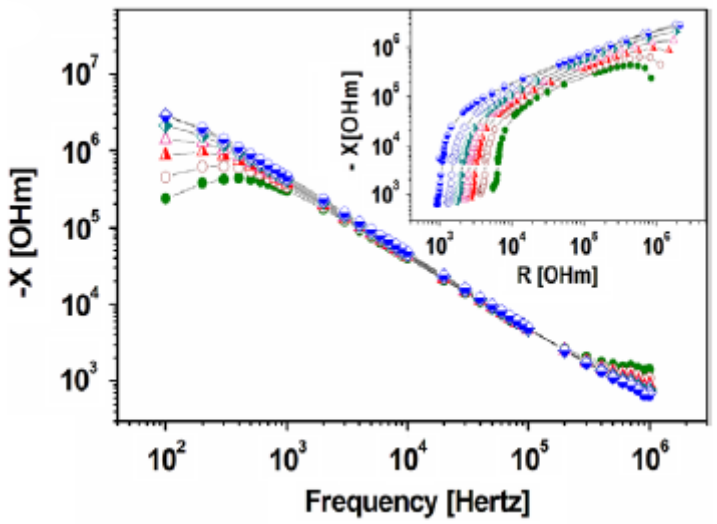

Fig. III.13: Imaginary part of the complex impedance spectra recorded at several fixed temperatures. In the inset the log-log Nyqvist plot is shown.

The different temperature dependences in the low and high frequency range, where the contribution of both series resistance R_s and R_2C_2 component becomes dominant. To clarify the specific temperature dependence of the various components, the experimental curves have been

fitted by the equivalent circuit at any investigated temperature. R_1 and R_2 temperature dependence is shown in Fig. 14, together with the log–log Nyqvist plot of the experimental impedance spectra, between 100 KHz and 1 MHz, and the corresponding fitting curves (inset of Fig. 14). As a result, the temperature dependent measurement indicates an opposite trend for R_1 and R_2. In fact, R_1 follows a semiconducting trend and its value increases up to 5 MΩ at cryogenic temperatures, supporting the idea that such parameter is mainly related to the organic film electrical properties; on the contrary, R_2 temperature dependent behavior is metallic-like and its value is about 400 Ω at 35 K. A complementary behavior is also followed by C_1 and C_2 (the former decreases of 30% from room temperature to 35 K and the latter tends to increase of about 20% in the same temperature range). These results can be framed in the logic of the parallel representation followed during the data analysis; in this context, R_2C_2 can be related to the properties of LSMO/Alq_3 interface.

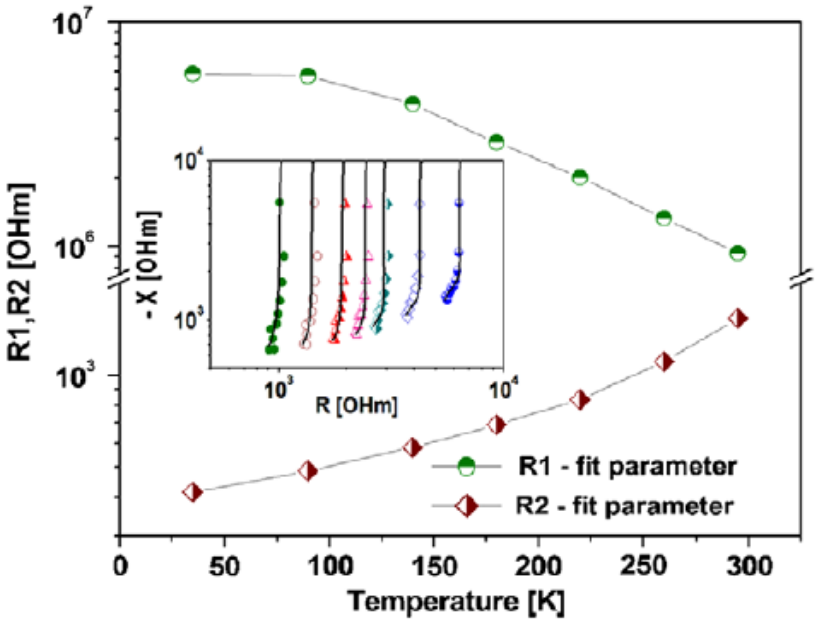

Fig. III.14: Temperature dependence of R_1 and R_2 parameters extracted for LSMO/Alq3/Al devices using the equivalent circuit in the parallel mode representation; the inset displays the log-log Nyqvist plot (symbols) and the relative fitting curves (solid lines).

As a matter of fact, due to the metallic character of LMSO, at lower temperatures a considerably higher injection efficiency is expected. At

higher temperatures, the metallic character of LSMO tends to decrease, as a metal-insulator transition is approached at around 340 K. Focusing the attention on the magnetoresistive effect, MR values decrease drastically with temperature and the phenomenon is explained by invoking the corresponding LSMO superficial magnetization reduction. To this respect, in Fig. 15 a comparison between the measured MR vs. temperature and LSMO temperature dependent superficial magnetization (as reported in literature[113] and commonly accepted by researchers) are reported. It is clear from the comparison that the quantitative agreement between both trends is very poor. In the attempt of overcoming this limitation, since in literature it is reported about a direct proportionality relation between the spin injection efficiency and the interfacial conductivity in manganite/organic systems[114], a phenomenological model where the interface effect is combined with LSMO magnetization has been conceived in order to explain the temperature dependent behavior of MR.

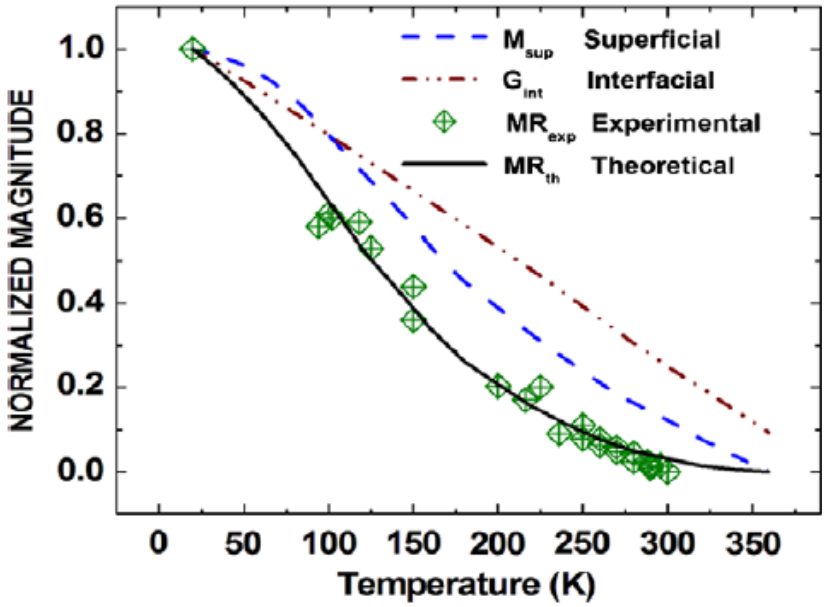

Fig.III.15: Experimental (symbols) MR temperature dependence compared with the theoretical data (solid line) calculated by multiplying superficial magnetization Msup (dashed line, Ref. [28]) with the normalized interfacial conductance G_{int} (dash dot line).

In detail, the temperature dependent magnetoresistance MR_{th} has been directly expressed by $MR_{th} = M_{sup} \times G_{int}$, where M_{sup} is LSMO superficial magnetization and G_{int} is the interfacial conductance given by $1/R_{2N}$. Here, R_{2N} is the LSMO/Alq_3 interfacial resistance normalized at T = 20 K, as extracted from R_2 data in Fig. 14. R_1, instead, is not taken into account in the model, since, as it has demonstrated above, it represents a contribution coming from the bulk of the organic semiconductor. The good quantitative agreement between experimental and predicted MR_{th} data obtained in this case confirms the importance of the interfacial resistance in the interpretation of magnetoresistance data for organic spin valves, even if the model is qualitative and, of course, lacks in containing an exhaustive explanation of the physical features of spin injection from the manganite into the organic semiconductor.

3.3) ac measurement techniques for the characterization of bottom contact OFETs properties.

Despite the range of applicability of dynamic electrical measurements, the analysis of electronic device response is sometimes strongly compromised by the same device architecture. It is widely known that Capacitance-Voltage (C-V) measurements can give a deep insight into the organic semiconductor based devices characterization. In particular, this technique can be employed for providing information on the nature of dielectric/semiconductor interface in thin film transistors, elucidating also some aspects concerning the mechanisms governing the charge transport occurred in the channel of the analyzed devices[115]. This aspect is for sure fundamental, considering that thin film transistors can be viewed as the basic electronic devices, thanks to which it is possible to implement all the basic functions required in the bosom of the Electronics.
Following the method introduced by Gundlach[40], already described in Chapter I (refer to section 1.2.e) for going back over the sense and the application of the model; in particular see eqs. (34) and (38)), for a pentacene-based device can be studied in order to show how it is possible to evaluate both the static contact resistance and the dynamic maximum device operation frequency in a simple, non invasive way. The experimental results, together with the specifications about the analyzed devices, will be reported in the next sections.

3.3.a) Pentacene-based TFTs; device manufacturing and main features.

Pentacene (P5) is an oligomeric material with chemical structure $C_{22}H_{14}$ (see Fig. 16). Due to its physical properties, it can be considered justifiably

as one of the most promising p-type materials for the manufacturing of efficient organic based devices.

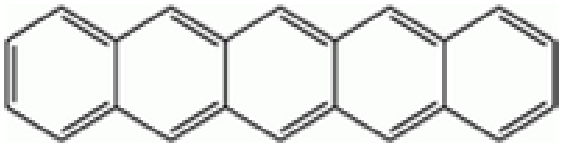

Fig.III. 16: P5 chemical structure.

In particular, as it is evinced by the wide literary production concerning the features of P5, there is a worldwide use of such molecule above all in the field of organic field effect devices[116]. The reason of such use founds in the fact that P5 shows a very high charge carrier mobility, comparable to that obtained with amorphous silicon (α-Si:H), since it is possible to exploit the possibility of controlling its ordered structure via growth processes[117]. For this reason P5 is in principle the main candidate for substituting α-Si:H and other inorganic semiconductors in many commercial applications, not particularly demanding in terms of operating speed, based on the use of TFTs.

In brief, a TFT is a device in which it is possible to modulate the electric current flowing into the device channel from the source electrode towards the drain electrode by means of a third terminal, that is the gate electrode. The gate electrode is in turn separated from the channel device by means of a dielectric layer. In this way, it is possible to use it in its simplest mode as an electronic switch and, implementing this basic function, as the active element on which the binary logic can be found. In detail, there are two types of responses for a TFT, that is the output characteristics (Fig.17.a), obtained by sweeping the channel voltage (V_{DS}, i.e. the voltage applied between the source and drain terminals) at fixed gate voltages (V_G), and the transfer characteristics (Fig.17.b), that is the curves recorded at a fixed channel voltage by sweeping the gate voltage.

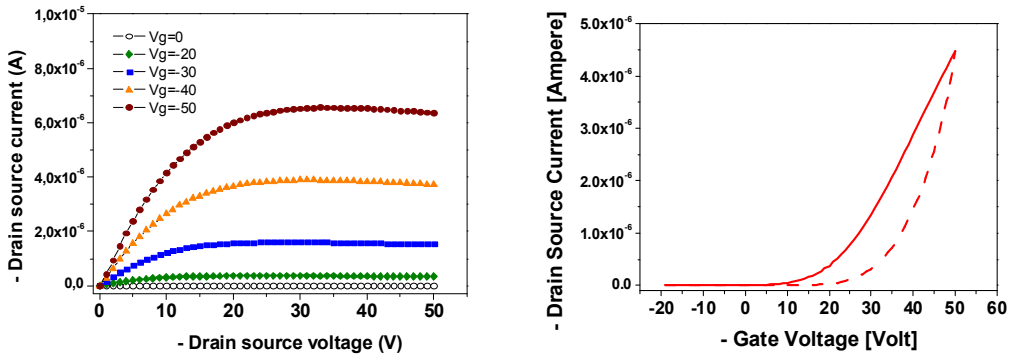

Fig. III.17: Typical output (a) and transfer (b) characteristics.

Anyhow, a more detailed theoretical description of TFTs response, aimed to understand the intimate meaning of such device response, will be given in the next Chapter. In this section, instead, the attention will be focused mainly on the features of the architectures employed for manufacturing the TFTs experimental prototypes, giving some information on the growth parameters and showing also both the dc response and the morphological features of the analyzed devices, without entering deeply into the details of such measurements (constituting the core of the Chapter IV). Indeed, it is worth to be underlined here that the latter aspect, that is the film morphology, has been widely remarked as the crucial topic on which the attention of researchers is mainly focused, since the growth procedure acts on morphology determining the goodness of manufactured devices.

As regards the device architecture, it has been already underlined that an interdigitade configuration of source and drain contacts is suitable for displaying a good device response. In this study, 100 nm thick gold interdigitated contacts have been deposited by lithographic technique on 200 nm thick SiO_2, thermally grown on lightly n-doped 1cm×1cm Si wafers. The nominal surface capacitance of the silicon dioxide is 17.25 nF/cm. The obtained test pattern is composed by four devices on each substrate with two geometries characterized by a channel width W equal to 11,2 mm (devices A and B) and 22,4 mm (devices C and D), while the

channel length is 20 µm or 40µ, respectively, giving thus a W/L ratio constantly equal to 550 (Fig. 18).

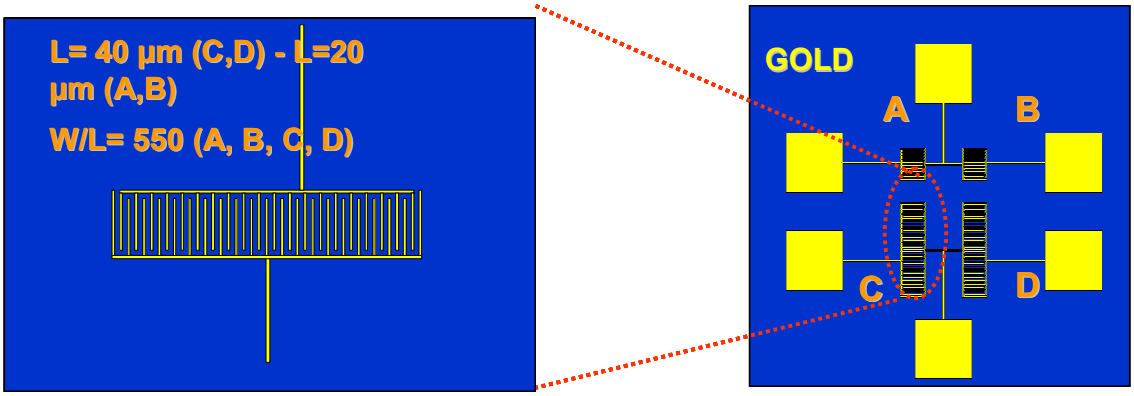

Fig. III.18: Device layout; on the left, the magnification of the interdigitated fingers together with the specifics of the channel devices are reported.

10 nm thick (that is about 6 monolayers, ML) of P5 thin films have been then growth by thermal evaporation at 10^{-8} mbar by means of a Knudsen cell, keeping the substrate at T room, with a deposition rate equal to 10 Å/sec. By using such deposition parameters, a morphology intermediate between a typical two-dimensional layer by layer growth and a three-dimensional grain boundary like structure has been obtained, as confirmed by AFM (Atomic Force Microscope) images (Fig.19.a). A typical transfer characteristics recorded in vacuum is instead reported in Fig. 19.b. Such measurement has been carried out by fixing the V_{DS} voltage at -40 V while the gate voltage has been swept staring from +40V to -40V, then returning to 40 V; such values of transversal and longitudinal fields define a condition well known as saturation regime. Such measurement shows clearly the accumulation of charge carriers and the following current increase in the gate voltage region starting from 0V up to -40V (red circled region in Fig. 19.b). The mean value of the p-type charge carrier mobility extracted in this case is 1.3 $cm^2*V^{-1}*s^{-1}$.

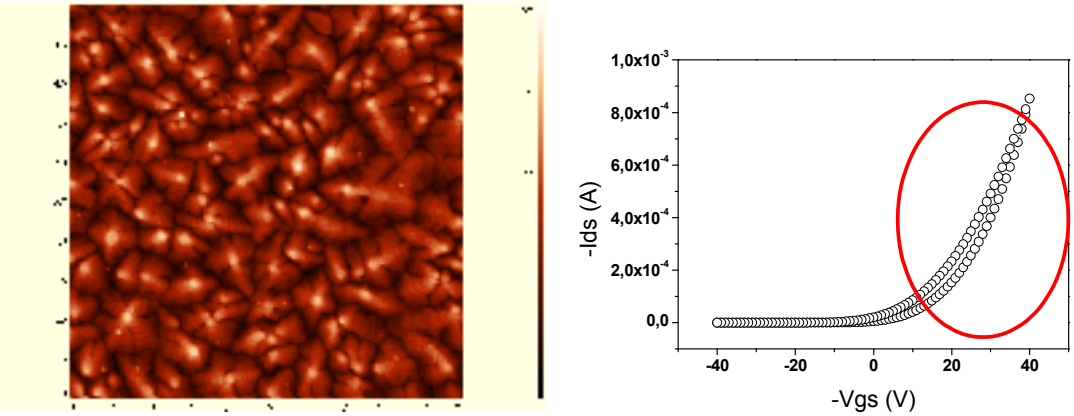

Fig.III.19: (a) AFM image of the 6ML thick P5 film growth at 10Å/sec; (b) transfer characteristics recorded at V_{DS}=-40V by sweeping V_G from +40 V to -40 V. The accumulation of holes is evinced by the increase of current at high negative gate voltage biases.

3.3.b) Experimental results: evaluation of static and dynamic device parameters.

As remarked above, C-V measurements have been performed at room temperature and in vacuum (10^{-4} mbar) on P5 based devices. Such measurements have been carried out by shorting together electrically the drain and source electrodes, choosing two complementary modes of measurement, that is:

- application of an ac small amplitude signal (100 mV) at a fixed frequency (100Hz) with a superimposed dc bias between the gate electrode and the shortened source and drain electrodes.
- application of an ac small amplitude signal (100 mV) at varying frequencies with a superimposed dc bias at different fixed values, starting from 0V (where the device is turned off since no accumulation takes place) up to -40 V (in the region in which accumulation is complete and the device is turned on, as indicated in fig 19.b).

The experimental curves collected by means of the above strategies are reported in Fig. 20 and Fig. 21, respectively.

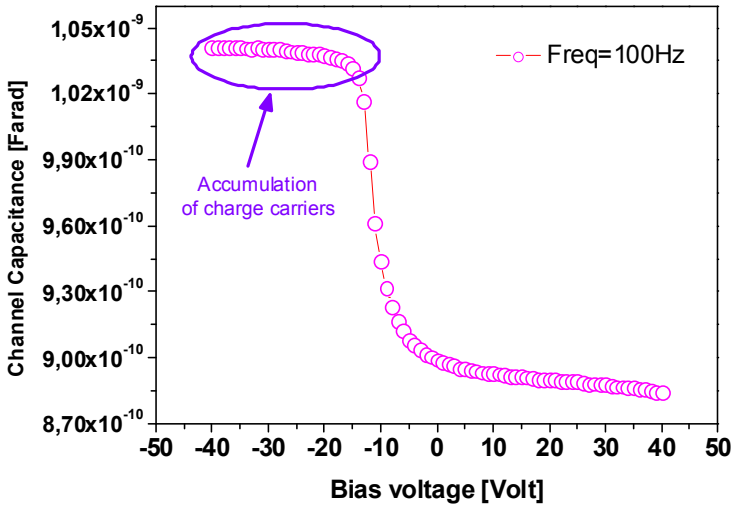

Fig.III.20: C-V measurement performed on P5 based device; the charge accumulation is displayed at high gate voltages by an increase of channel capacitance due to the field effect. The relative saturation indicates that the occurrence of the charge accumulation has been completed.

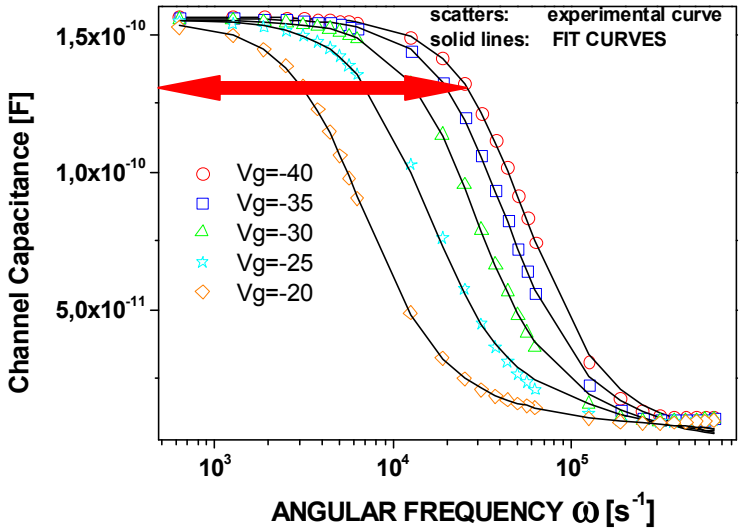

Fig.III.21: Absolute channel capacitance vs. frequency at fixed dc biases (solid symbols) and fitting curves (lines) performed by using the finer TL model (Mod 2 considers also the contact resistances). By increasing the dc gate voltage bias, the dynamics describing the building of the accumulation layer can be monitored. The red arrow indicates the width of the region of charge accumulation.

Focusing the attention on Fig. 20, it is evident that the dynamics of charge accumulation can be monitored by using C-V measurements. In fact, at

100 Hz (which is generally a frequency corresponding to a quasi static condition for many organic disordered materials) the increase of gate voltage towards high negative values is expected to be responsible of p-type charge carriers accumulation in the device channel. Since source and drain electrodes are electrically shorted, but separated by the channel length L, it is possible to see the building of charge carriers in the same channel. In detail, when the charge carriers accumulate in the channel, the initial device structure constituted by two similar capacitors linked in parallel, each of them denoted as $C_{electr.}$, becomes an unique capacitor with a top plate characterized by a surface equal to the area of the active device (that is the area of the electrodes plus the area W*L of the channel). As regards the nature of $C_{electr.}$, they are substantially plate plane structures where the top plate is constituted by the surface of one channel electrode, source or drain indifferently, and the bottom plate by the gate electrode, being finally the resulting capacitor filled with the silicon dioxide. So, in the context depicted above, the increase of gate voltage bias corresponds to the increase of channel capacitance, more precisely to the difference between the capacitance measured when the device is in accumulation mode ($C_{accum.}$) and the capacitance measured for the depleted device (which is constantly equal to the parallel between two similar capacitors $C_{electr.}$, that is $C_{electr.}/2$). The saturation at high negative gate voltages indicates that the accumulation process is completely occurred. Of course, by evaluating the difference $C_{accum.} - (C_{elect}/2)$ it is possible to assess the density of accumulated charge carriers, that is the sheet charge density. In this way it is possible to evaluate in a precise way, excluding many sources of error, the actual charge carrier mobility μ from the transfer characteristics, being μ the most important static parameter characterizing a field effect device. The measurement displayed in Fig. 21 is instead useful for implementing the model introduced by Gundlach. In fact, the frequency dispersion at high frequencies predicted by Gundlach is

evidenced in this measurement. In detail, such frequency dispersion is deduced by the observation of a crossover between the low frequency region in which charge accumulation takes place and the high frequency region where the accumulation of carriers is not sustained by the quick variations of the gate field. So, such tool can be viewed as a criterion for monitoring in a precise way the dynamics of charge accumulation. At first blush, the cut-off frequency at which the crossover occurs can be calculated by estimating the point where the straight line approximating the low frequency plateau runs across the line approximating the high frequency dropping of capacitance (dispersion zone). By a fitting procedure, the cut-off angular frequency at V_G -40V has been evaluated to be equal to $1.9*10^4$ s^{-1}, corresponding to a frequency of 3KHz.

It is clear that the evaluation of the cut-off frequency in the accumulation mode furnishes a criterion for assessing a very important dynamic parameter for OFETs, that is the device operation frequency. This dynamic parameter is of paramount importance in many basic electronic applications, since it is required that an electronic device based on organics has to be able to work at certain frequencies in order to rectify ac signals for many device applications (for example radiofrequency identification tags, RFIDs). The powerfulness of C-V measurements is then crucial, since the evaluation of the limits showed by organics is still an open issue in the research and development of organic based devices. Of course, as indicated in discussing the TL model, ac measurements on bottom contact devices allows to evaluate also the contribution given by the contact resistance to the overall device channel resistance. In this respect, the TL model indicated as MOD 2 in Fig. 16 takes into account the capacitive and resistive contributions of the contacts. The overall channel resistance calculated by a transfer characteristics recorded at V_{DS}=-1V is reported below (Fig. 22), together with the measurement of the channel capacitance

measured at a gate voltage equal to -40 V and the related fitting curves (Fig. 23).

As stated above, the overall channel resistance evaluated from the recorded transfer characteristics is essentially the expression of two contributions which are indistinguishable in the bosom of the dc measurement. Indeed, the ac measurement is able to separate such contributions. In Table I the fitting parameters extracted by using both MOD 1 and MOD 2 are reported.

	χ^2	R_{ch}	C_i	R_c	C_c
MOD 1	$2.43*10^{-23}$	780KΩ	157pF	×	×
MOD 2	$1.27*10^{-24}$	840KΩ	156pF	170KΩ	1pF

Tab. III.2: Fitting parameters extracted from the C-V curve reported in Fig. 223 using TL MOD 1 and MOD 2. Here, R_{ch} is the channel resistance, C_i is the interfacial capacitance, R_c is the contact resistance and C_c is the contact capacitance.

A comparison between the two models reveal that the second one (MOD 2) well adapts itself to experimental dc results. In fact, the overall channel resistance extracted from transfer characteristics, equal to 1 MΩ, well matches with the overall channel resistance obtained by adding the contact resistance R_c (170 MΩ) to the bare channel resistance R_{ch} (840 MΩ) extracted using MOD 2. Moreover, also the contribution of contact capacitance has been obtained from experimental data. In this case it is clear that the contribution of the contact capacitance can be neglected, since such capacitance contribution to the overall interfacial capacitance is less that 1%.

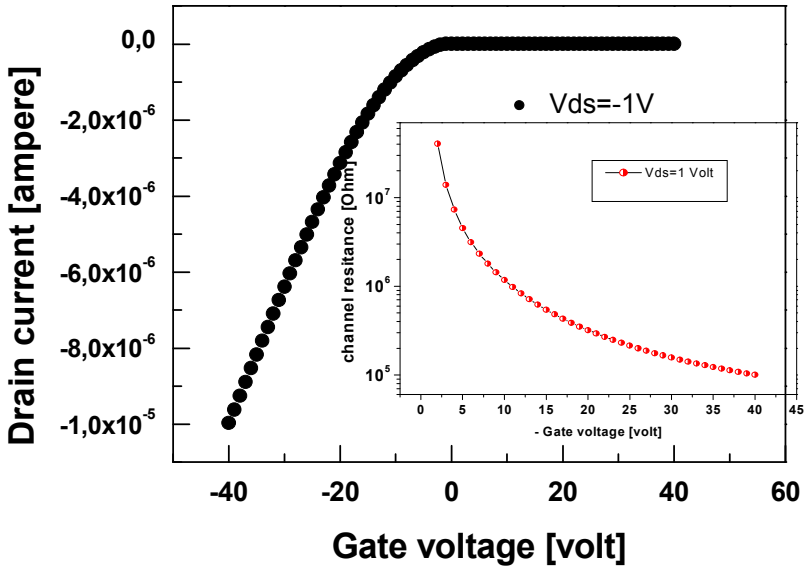

Fig.III.22: Transfer characteristics recorded in vacuum by sweeping the gate voltage from + 40V to - 40 V with V_{DS} fixed at -1V. In the inset the overall channel resistance, equal to 100 KΩ, calculated from the transfer characteristics using the Ohm's law, is reported.

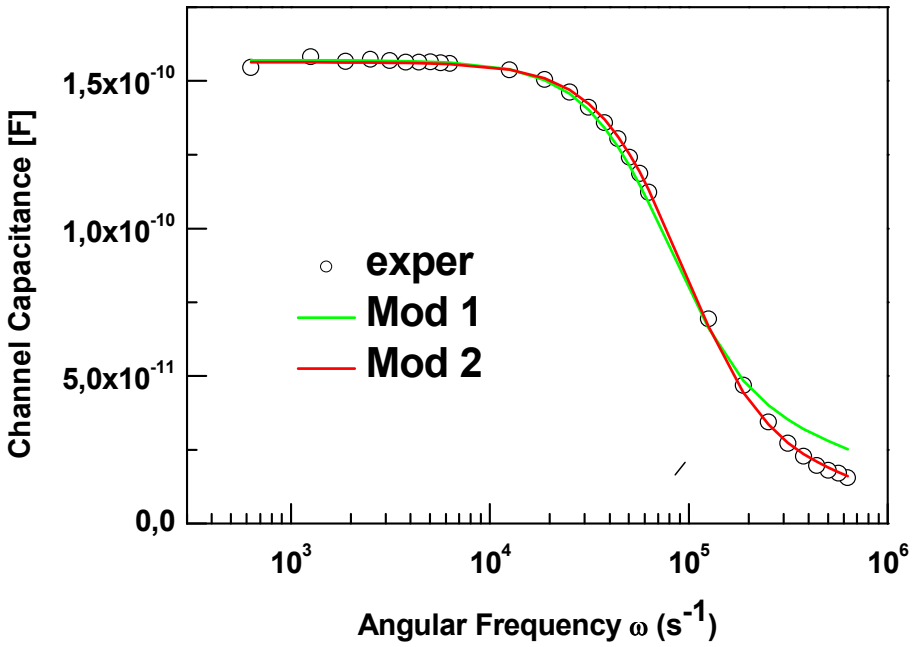

Fig. III.23: Channel capacitance vs. angular frequency at a gate voltage bias equal to -40 V. The fitting curves (MOD1 and MOD 2) are reported a s solid lines.

Chapter IV

Dynamic study of stress phenomena in organic based Thin Film Transistors (TFT).

4.1) Introduction on bias stress phenomenology: shift of threshold voltage.

A very common feature of organic based materials and related devices is constituted by the presence of both intrinsic[118] and extrinsic[119] defects. Such defects arise in first approximation from the intimate nature of energetic interactions among the basic constituents of the materials. So, the resulting features of materials concretize themselves in a structural 'intrinsic' disorder and favor the inclusion of 'extrinsic' impurities both in the bulk of materials and at the different device interfaces. Of course, the presence of defects reflects on materials physical properties, with a special reference to the electric ones. In fact, the flow of electrical current is dramatically influenced by charge carriers trapping mechanisms[120]. The phenomenology of trapping mechanisms manifests in some peculiar features that can be traced back to one main basic effect: the arising of hysteresis in the I-V characteristics recorded upon the application of a cyclic voltage scan sweep[121]. In terms of device applications, on one hand such effects can be often exploited in the context of sensoristics but, on the other hand, they can also affect in a negative way the device stability. In particular, the stability of OFETs is a crucial aspect for the standardization of device operations[122]. The trap states, instead, affect such stability by provoking the emergence of a peculiar phenomenon, known as bias stress, very common for amorphous and polycrystalline semiconductors[123,124].

Bias stress corresponds to an electrical instability manifested by a decrease in time of the transfer current or, in an alternative view, by the shift of threshold voltage, ΔV_{th}, towards positive values in case of hole transport (where V_{th} is in practice the gate voltage at which the field-induced mobility controls the channel current) upon prolonged or repeated application of the gate bias V_G[122]. The physical origin of bias stress can be found in the above mentioned trap states energetically located near the

conducting HOMO and LUMO levels (Fig. 1). The resulting density of states (DOS) is thus affected by the presence of some intrinsic and extrinsic trap states in its tail. The traps described above usually do not contribute to the transport; in fact the extrinsic localized trap states differ from the majority of intrinsic hopping states of amorphous materials for the fact that the first ones require a substantially larger energy to release charge carrier to the intrinsic DOS[125].

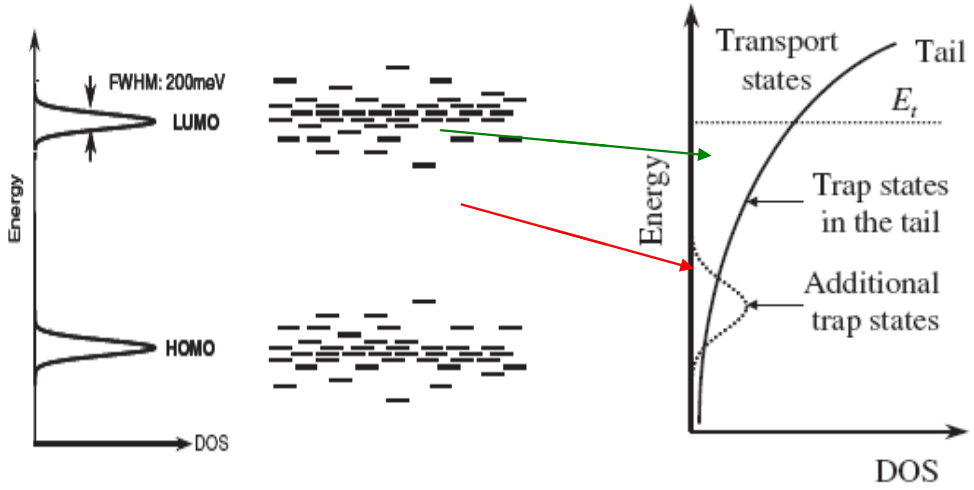

Fig.IV.16: Trap states localized near the HOMO and LUMO levels in the context of a typical energetic diagram of organic materials (left) and effect of trap states on the relative density of states (DOS).

As far as the shift of threshold voltage towards higher values is concerned, its origin lies in the emergence of an electric field of trapped charges which must be compensated by a gate voltage increase, suitable to build the accumulation layer at the gate dielectric interface. In this respect, it is believed that the nature of traps responsible of threshold voltage shift in organic based devices is mainly extrinsic or, at least, can be linked to the presence of interfacial states, even if it cannot be excluded the role of intrinsic factors such as structural defects[126] (that is morphological features), trapped electrons[127,128] or bipolaron formation[129]. More precisely, it is believed that bias stress in pentacene based devices is addressable to the presence of environmental factors, such as water moisture[130,131] and

oxygen[132,133], which favor the formation of interfacial traps, located at gate dielectric/organic channel interface.

Historically, many works have regarded the study of bias stress performed by monitoring the physical observable ΔV_{th}, in particular by analyzing the shift in the threshold voltage V_{th} from its initial value $V_{th,0}$ as a constant V_G is applied for an increasing time t[134,135]. The method has been developed for explaining the phenomenology of the instabilities showed by devices based on amorphous silicon or polycrystalline inorganic semiconductors[136]. In brief, the threshold shift is linked to the surface density of trapped charges N_{tr}:

$$\Delta V_{th} = \frac{eN_{tr}}{C_{ox}} \quad , \tag{1}$$

where C_{ox} is the dielectric layer capacitance per unit area and e is the elementary electric charge.

The N_{tr} time variation, that is the trap filling rate, is proportional to the free carriers density N_f according to the law:

$$\frac{dV_{th}}{dt} \propto \frac{dN_{tr}}{dt} \propto N_f(t) * \frac{t^{\beta-1}}{\tau^{\beta}} \, , \tag{2}$$

where β is a dispersion parameter and τ is the relaxation time (usually very long for organic based devices). Both these parameters are linked to the features of the traps distribution; in particular β will turn out to be a stretching factor depending on materials, temperature and processing conditions, while τ represents in practice the trapping time constant[137]. By solving eq. (2) and imposing that V_{th} at infinite stress time equals the applied gate bias, the expression of threshold voltage is obtained in form of a stretched exponential time-dependent evolution[134,135,136]:

$$\frac{\Delta V_{th}}{(V_G - V_{th,0})} = 1 - \frac{N_f(t)}{N_f(0)} = 1 - \exp\left[-\left(\frac{t}{\tau}\right)^{\beta}\right], \tag{3}$$

where $V_{th,0}$ is the initial value of V_{th}.

So, it is clear that eq. (3) arises from the hypothesis that the threshold voltage shift is contributed by the charge carriers trapped with an exponential distribution of traps, spatially located at the semiconductor-dielectric interface. In particular, in calculating the expression (3), it is substantially assumed that both intrinsic states and extrinsic traps are distributed with a stretched exponential DOS of different widths.

Operatively, the experiments are generally performed by monitoring the time evolution of the current flowing into the OFET channel upon the device is polarized by fixing the operating point, that is both the gate and the channel voltages (Fig. 2.a), or by performing cyclically the transfer characteristics in a wide temporal range, monitoring thus the evolution of V_{th} shift directly from the recorded curves (Fig. 2.b).

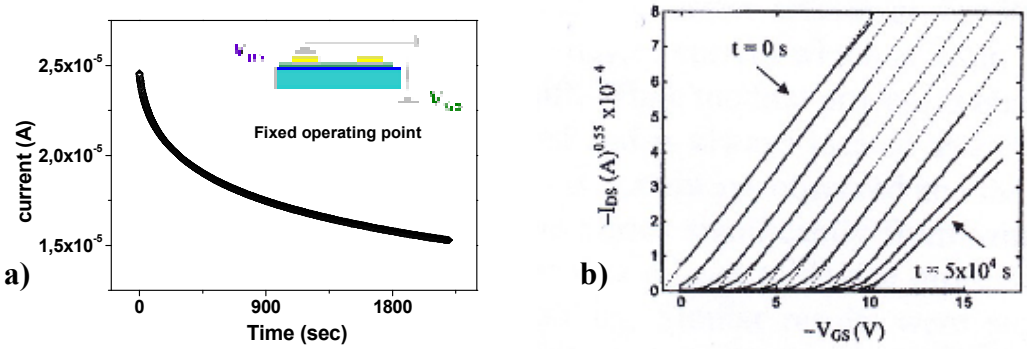

Fig.IV.2: a) channel current vs. time at an arbitrary fixed operating point; b) shift in time of transfer characteristics upon stress mechanisms.

It is simple to convince oneself that the shift of threshold voltage and the time-decaying current are two alternative ways for displaying the same effect[138]. In fact, the expression of the transient channel current (Fig. 2.a) is obtained by the expression of the transfer characteristics in linear regime as:

$$-I_d(t) = \mu \frac{W}{L} C_{ox} \left[V_G - V_{th,0} - \Delta V_{th}(t) - \frac{V_{DS}}{2} \right] V_{DS}, \qquad (4)$$

where is the channel voltage, W and L are the channel width and length, respectively and μ is the field effect mobility, where the decreasing in time

can be attributed to the increasing in time of the absolute value of V_{th}, that is the only time-varying parameter in the expression of the device channel current.

If the term ΔV_{th} in eq.(4) is explicated using eq.(3), the transient current then becomes:

$$-I_D(t) = I' + I_0 \exp\left[\left(\frac{t}{\tau}\right)^{\beta}\right], \tag{5}$$

with:

$$I' = \mu\left(\frac{W}{L}\right)C_{ox}\left[-\frac{V_{DS}}{2}\right]V_{DS},$$
$$I_0 = \mu\frac{W}{L}C_{ox}\left(V_G - V_{th,0}\right)V_{DS}. \tag{6}$$

The measurement of $\Delta V_{th}(t)$ through the static approach above described is for sure invasive, as it requires a long time scale needed for stressing the device by the application of a constant, high, gate bias. The static electric fields applied exceed 10^4 V/cm for typical device layout with tens micrometer channel and hundred nm dielectric layer thickness. These high field values may affect the energy of intrinsic trap states are located at the structural defects, i.e. at the grain boundaries[139], causing the apparent decay of the charge mobility and leading to an irreversible degradation of the device performance. Less invasive schemes of measurement operating on shorter or multiple time scales would be desirable for the systematic investigation of charge trapping and the related assessment of device stability. In this respect, a dynamic approach consisting in correlating the charge carrier trapping with the emergence of hysteretic phenomena occurred in the measured transfer characteristics seems to be adequate. In the next section such criterion will be treated in all its implications in the case of P5 based TFTs, showing also its experimentally favorable features, consisting both in the overcoming of the limitations induced by static field device operations and in the possibility of monitoring the consequences of

trapping features on very short time scales compared to those involved in trapping mechanisms[140]. Above all, in this way the device stress will be observed directly from the features showed by the typical curves used for characterizing the device properties, that is the transfer characteristics. Moreover, this aspect can impart further advantages in terms of the comprehension of the role played by trapping mechanisms on other important device parameters such as the mobility, since in this way it is possible to relate the features of hysteretic phenomena to the overall device operative response.

4.2) Hysteresis in transfer characteristics: a novel parameter for the study of charge trapping phenomena at gate dielectric/organic semiconductor interface.

The staring point of the dynamic study of trapping phenomena in TFTs based on oligomeric materials such as pentacene is the emergence of hysteretic phenomena in transfer characteristics[141]. In particular, the hysteretic behavior consists in a decrease of the drain current I_D during the scan sweep of V_G from the 'on state' to the 'off state' (backward scan) with respect to the corresponding values in the forward scan (Fig. 3).
A detailed analysis of the curves recorded in Fig. 3 indicates some interesting topics. In particular, two aspects attract immediately the attention:

- the arising of the hysteresis in transfer characteristics; in detail, the magnitude of the current showed by curve recorded in forward scan sweep, corresponding to the device turning on (that is, from +40V, where a complete depletion of the channel device is found, to -40V, in the heart of the accumulation regime), exceeds its magnitude obtained in backward scan sweep (corresponding to the turning off of the device). Generally, this occurrence appears for high trapping rates compared to the gate voltage scan rate used for the measurement[142,143].
- the effect of environmental conditions reflect both on the hysteresis and maximum output current magnitude [I_D(-40V)], being the hysteresis more pronounced in air and the output current higher in vacuum.

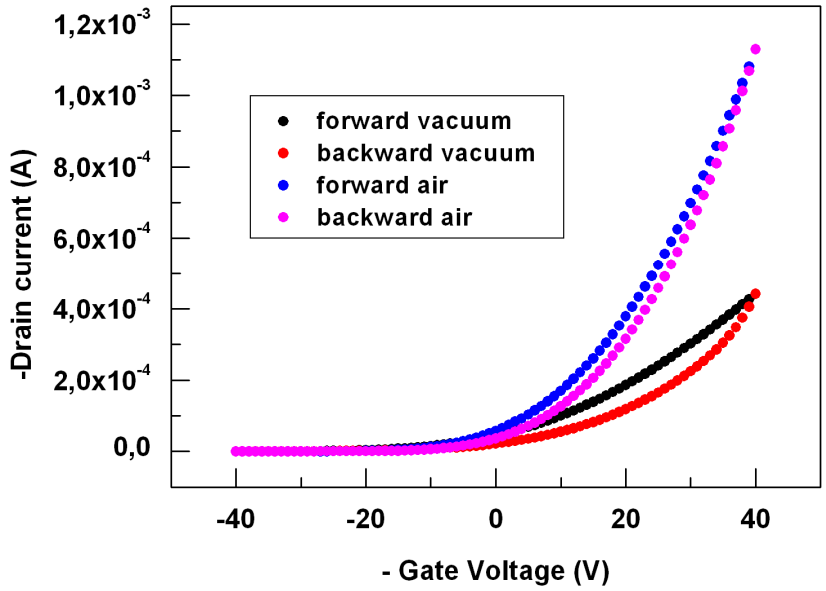

Fig.IV.3: Transfer characteristics of a P5-based TFT recorded in air and in vacuum by sweeping the gate voltage in forward scan (black and blue symbols) and backward scan (red and magenta symbols) at a fixed drain voltage (-20V).

As commonly retained with good reason by researchers, these topics represent an evidence of the occurrence of trapping phenomena in OTFTs. In fact, it is clear that the environmental conditions strongly affect the device response, as expected on the basis of the contents reported by many studies regarding the bias stress phenomenology. In particular, as stated above, humidity and oxygen contained in air create some impurities at the the conducting channel/gate dielectric interface [130,131,132,133].

As a matter of fact, it is obvious that device response is able to reveal directly the presence of charge trapping through the monitoring of the hysteresis arisen in presence of air. In this respect, the framework of the analysis developed for the characterization of trapping mechanisms in P5 based TFTs starts from the transfer characteristics in linear and saturation regimes, given by the following expression, respectively:

$$\begin{cases} I_D(t) = \dfrac{W}{L} \cdot \mu_0 \cdot C_{ox} \cdot V_D \cdot \left[V_G(t) - V_{th}\right] & for \ \ |V_D| < |V_G - V_{th}| \\ I_D(t) = \dfrac{W}{2L} \cdot \mu_0 \cdot C_{ox} \cdot \left[V_G(t) - V_{th}\right]^2 & for \ \ |V_D| \geq |V_G - V_{th}| \end{cases} \quad (7)$$

The various terms in eq. (7) have been already defined previously. Such exprssions are obtained upon application of a time varying gate sweep $V_G(t)$. In particular, $V_G(t)$ is a time-dependent triangular wave in the range $[-V_{max}; V_{max}]$. Therefore, the gate sweep introduces a time scale $t=|V_G/a|$ where the scan rate a is expressed in volts per second. Considering holes as carriers, in the first half period T/2, the forward scan goes from $V_G = 0$ to $V_G = -V_{max}$, and the backward scan from $V_G = -V_{max}$ to $V_G = 0$. The transistor must be in 'on state' at $V_G = -V_{max}$. The gate voltage sweep and, consequently, the current I_D both show a discontinuity in their time derivative at $t=T/4= V_{max}/a$ i.e. when $V_G = -V_{max}$. V_{max} can be termed for the sake of simplicity as the 'turning point'.

Here, the hysteresis appears in the neighborhood of the turning point at the beginning of the backward scan due to the presence of long-lifetime traps[21]. The outcome is an effective time-dependent current opposing the current eq. (7) which flows in the OFET channel in absence of trapping mechanisms. The time-evolution of I_D in the linear regime becomes in presence of trapping mechanisms[17]:

$$\frac{\partial I_D(t)}{\partial t} = \frac{W}{L} \cdot \mu_0 \cdot C_{ox} \cdot V_D \frac{\partial V_G(t)}{\partial t} - k \cdot \frac{t^{\beta-1}}{\tau^{\beta}} \cdot I_D(t), \qquad (8)$$

where the time scale t is smaller than τ, and the second term to the right hand side (which translates into eq.(2)) represents the contribution to the observed current due to a trapping mechanism arisen from a stretched-exponential distribution of traps. Here, τ and β are defined in the expressions (2) and (3), while the constant k scales according to the density of trap states[137]. Although the assumption of a specific trapping mechanism is not needed for the following discussion, the exponential distribution of traps has been chosen as a case model.

In the neighborhood of V_G=-V_{max}, $\left.\frac{\partial V_G(t)}{\partial t}\right|_{\frac{T^-}{4}} = -a$ and $\left.\frac{\partial V_G(t)}{\partial t}\right|_{\frac{T^+}{4}} = a$.

The chain rule relates the time-evolution eq. (8) to the transfer characteristics as:

$$-a\left.\frac{\partial I_D(t)}{\partial V_G}\right|_{-V_{\max}^-} = \left.\frac{\partial I_D(t)}{\partial t}\right|_{\frac{T^-}{4}}, \tag{9a}$$

$$a\left.\frac{\partial I_D(t)}{\partial V_G}\right|_{-V_{\max}^+} = \left.\frac{\partial I_D(t)}{\partial t}\right|_{\frac{T^+}{4}}. \tag{9b}$$

Thus, the difference in the slope of the transfer characteristics at the discontinuity can be ascribed only to the trapping term in equation (8):

$$\begin{aligned}\Delta m &= \left.\frac{\Delta I}{\Delta V_G}\right|_{-V_{\max}^-} - \left.\frac{\Delta I}{\Delta V_G}\right|_{-V_{\max}^+} = \frac{2kt^{\beta-1}}{a\tau^{\beta}} I_d(t)\Big|_{\frac{V_{\max}}{a}} = \\ &= 2k\frac{V_{\max}^{\beta}}{a^{\beta}\tau^{\beta}}\frac{I_d(V_{\max}/a)}{V_{\max}}.\end{aligned} \tag{10}$$

$$\frac{V_{\max}}{I_d(V_{\max}/a)}\Delta m = \Delta\left.\frac{\partial \ln I_d}{\partial \ln V_g}\right|_{V_{\max}} = 2k\frac{V_{\max}^{\beta}}{a^{\beta}\tau^{\beta}}. \tag{11}$$

Eq. (10) links the hysteresis to the maximum gate voltage $V_{max,}$ the scan rate a and the trapping time scale τ. The transconductance $I_d(V_{max}/a)/V_{max}$ at the turning point disappears in the logarithmic derivative [eq. (11)], so in this way an adimensional Δm parameter can be obtained.

As far as the sense of eq. (10) is concerned, first of all it is clear that it predicts a linear dependence of Δm vs $I_{D,max} = I_D(V_{max})$ in the case of trapping by an exponential distribution of traps. The current dependence in eq. (10) allows one to sort out possible mechanisms with different exponents, e.g. bipolarons recombination as in ref. 11. It is important to remark here that hysteresis is not exhibited when the gate voltage V_G is smaller in absolute value than $V_{th,0}$. So the extrapolation of eq. (10) versus

V_G=-V_{max} to Δm=0 yields V_G=$V_{th,0}$. Moreover, since Δm depends on V_{max} both in the power law term and the current, in order to extract the trapping parameters β and k/τ^{β} , it is preferable to fit the differential logarithmic derivative versus V_{max} in eq. (11).

To summarize, the above defined novel hysteresis parameter Δm contains the information about the trapping mechanism, and can be extracted from the analysis of transfer curves at the turning point, as shown in the next section. The innovative character of such tool is constituted by the fact that the time scale of the operation, which is set by the choose of scan speed a as V_{max}/a, is much faster than the time scales used in the studies with static electric fields, thus allowing one to minimize the stress of the device induced by undesired phenomena. Finally, the dynamic character of the measurement aimed to predict the dependence of Δm on V_{max} depends on the way in which the experiment is performed. In fact, the combination between the chosen fast time scale and the reiteration of the triangular gate voltage scan sweep over subsequent forward-backward scan cycles are equivalent to a sort of ac measurement obtained using a triangular waveform V_G scan sweep which spans shorter temporal scales with respect to the trapping time scale τ.

4.2.a) Dynamic analysis of stress phenomena in pentacene TFTs.

The interest of researcher on organic materials employed for the manufacturing of FET devices is mainly addressed to pentacene due to its promising properties in terms of device performances[144,145]. Unfortunately, pentacene is also very sensitive to environmental conditions, showing generally a very strong hysteretic behavior. In this respect, pentacene represents a good reference material, so it represents for sure the ideal candidate for testing the validity of equation (10) on pentacene based

devices. The experimental procedure has been carried out in trhe following way.

P5 based TFT devices have been obtained by evaporating about 6 ML (10 nm nominal thickness) of pentacene on Si/SiO_2 substrates at a rate 1 ML (1.5 nm)/min, keeping the substrate at room temperature during the deposition. Test pattern devices are made with gold/titanium (Au/Ti) interdigitated contacts whose W/L ratio is 2000 and channel length L equal to 20 μm. Transfer characteristics have been measured at room temperature in linear regime, with V_D = -20 V. Sequential gate sweeps V_G have been carried out by varying the gate voltage in the range $[-V_{max};+V_{max}]$ and increasing cyclically V_{max} by 5V step from 20 V to 50 V. In this way, a triangular waveform V_G scan, characterized by the increasing of its amplitude (equal to V_{max}) by the amount equal to 5 V after each period T, has been employed. The environmental conditions have been then controlled by introducing a moisture of air and 30% of relative humidity (RH) in the probing chamber, previously kept at a baseline pressure of 10^{-5} mbar.

Before proceeding with the analysis of the experimental results, it is noteworthy to underline here the importance of considering the transfer characteristics in linear regime, since in this case it is possible to avoid the 'pinch off' condition, allowing thus an uniform enrichment of charge carriers induced by the gate voltage along the channel length. In this way, the field effect technique favors an uniform probing of traps near the organic/dielectric interface.

In Fig. 4 a detail of the experimental transfer characteristics of a pentacene OFET in the proximity of V_G=-30 V is showed. A linear approximation has been used here to fit the forward and backward scans and extract the hysteresis parameter as the differential slope Δm the at turning point V_G=-V_{max}.

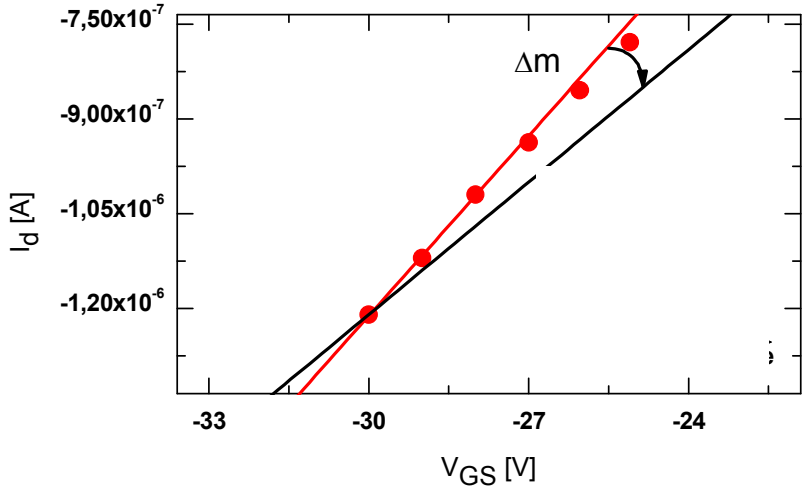

Fig.IV.4: Detail of the transfer characteristic for a pentacene based thin-film transistor measured in forward (■) and backward (●) scan in the neighborhood of V_G =-30 V . The gate voltage scan rate is a=1 V*sec^{-1}. The extracted differential slope of the transfer characteristics is Δm=2.5*10^{-8} Siemens.

In Fig. 5 the series of transfer characteristics measured with a=0.1 Vsec^{-1} is shown. The differential slope Δm increases with increasing V_{max}, as shown in the inset. The apparent trend can be fit to a power law with exponent equal to 0.75±0.05. The onset of the observed hysteresis (i.e. Δm=0) yields $V_{th,0}$=-17.9±0.7 V. Figure 5a shows the trend of Δm as a function of $I_{D,max}$. The trend is almost linear (a free-parameter power law fit vs $I_{D,max}$ yields an exponent equal to 0.94) and can be fit by a straight line Δm (S) ≈ 0.112±0.002 $I_{D,max}$ (A). In Fig. 5b the difference in the logarithmic derivative eq. (11) versus V_{max} is plotted. The trend is linear (β≈1), suggesting a mechanism consistent with an exponential distribution of traps[123]. Te extracted β value does not match the value (β≈0.4) which has been obtained monitoring bias stress[133]. Using β≈1 in the fitting pre-factor in eq. (11), it turns out that the effective trapping rate is $k/\tau \approx 6 \cdot 10^{-3}$ s^{-1}. The 10^2-10^3 s time scale is in good agreement with the trapping time scale (10^3 s) estimated in ref. 123, and one order of magnitude shorter than the time scale reported in ref. 133. This evidence could be viewed as a

consequence of the humidity-controlled conditions employed in performing the experiment[123].

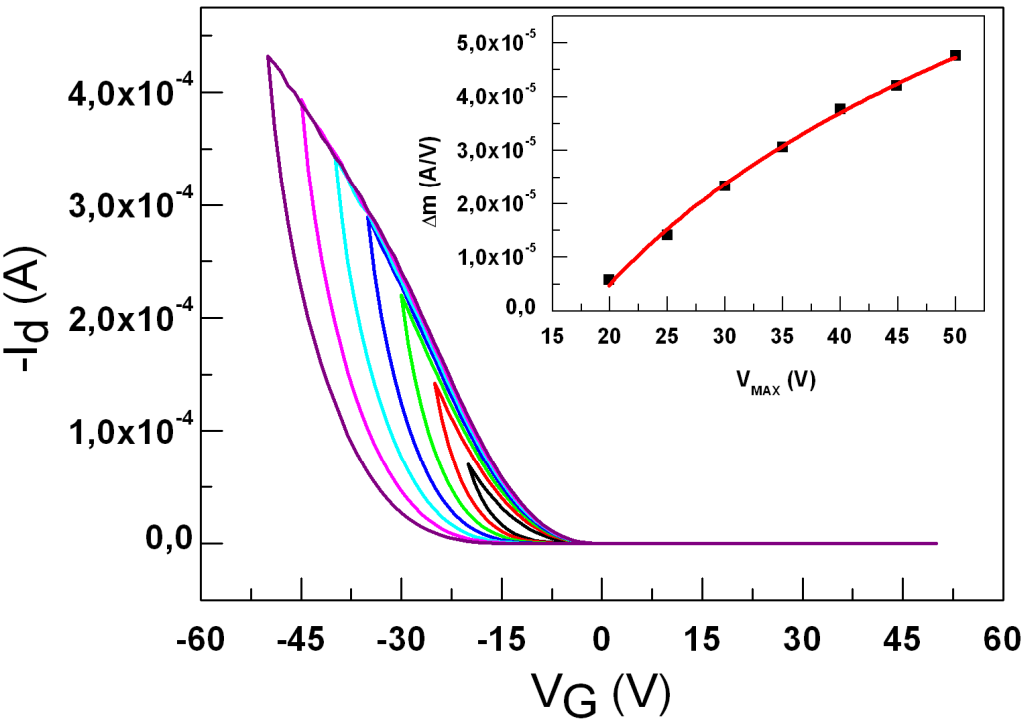

Fig.IV.5: Transfer characteristics of pentacene OFET exhibiting hysteresis. They are acquired with V_D=-20 V and gate voltage sweep V_G ranging from [-V_{max};+V_{max}]. Different hysteresis curves correspond to gate sweeps with V_{max} increasing from 20 V to 50 V by 5V step. The inset shows the trend of extracted Δm vs V_{max}. Continuous red line is the power law fit Δm (A/V)=3.5 (±0.7)·10^{-6} · (Vmax -17.9(±0.7))$^{0.75(\pm0.05}$ (V).

The experimental results show that, in the case of pentacene, the features of the distribution of traps inferred from the combination of eq. (10) and (11) are consistent with an exponential distribution of traps[123]. In fact, β=1 implies an exponential time-decay of the current from eq. (8) according to the following expression, obtained by performing the integral of the eq.(8):

$$I_D(t) = I_D(0)\exp[-(k/\tau)t] + \\ + \frac{W}{L}\cdot\mu_0\cdot C_{ox}\cdot V_D\, a\frac{\tau}{k}\left[1-\exp[-(k/\tau)t]\right]\cdot \qquad (12)$$

Here, the first term in eq. (9) is the solution of the homogeneous equation, the second is instead the convolution of the corresponding Green's function.

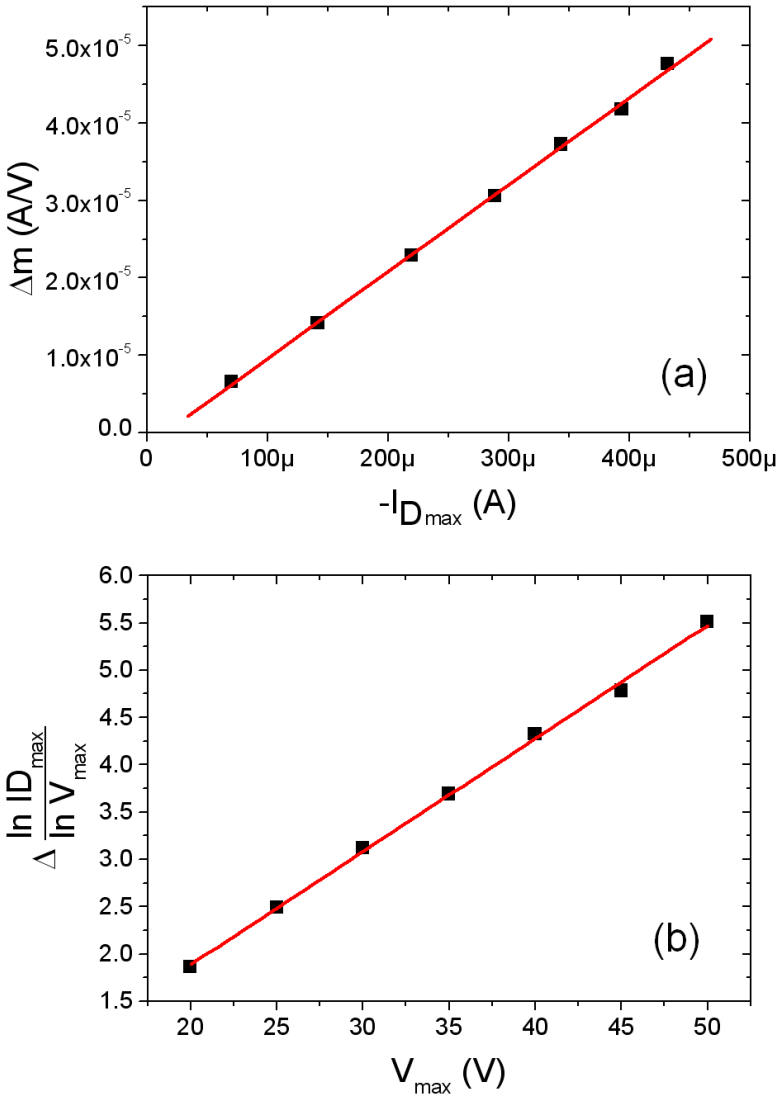

Fig.IV.6: (a) Hysteresis parameter Δm vs $I_{D,max}$ extracted from the transfer characteristics in Fig. 2. Best fit (red line) is Δm≈0.112 (±0.002) (V^{-1}) I_{Dmax} (A). (b) differential logarithmic derivative at the turning point vs V_{max}. Best fit (red line) is y≈0.120 (±0.002) (V^{-1}) V_{max} (V).

The decay rate is intrinsic to the trapping mechanism, whereas the pre-exponential factor is modulated by the gate scan rate a. considering the boundary condition in the expression of transfer characteristics in linear regime (eq. (7)), the current $I_D(0)$ can be written as:

$$I_D(0) = -\frac{W}{L} \cdot \mu_0 \cdot C_{ox} \cdot V_D V_{th,o} \,. \qquad (13)$$

In the short time limit of our experiment, eq. (12) yields:

$$I_D(t) \approx \frac{W}{L} \cdot \mu_0 \cdot C_{ox} \cdot V_D \left[at - V_{th,0} \right] = \frac{W}{L} \cdot \mu_0 \cdot C_{ox} \cdot V_D \left[V_G(t) - V_{th,0} \right] . \qquad (14)$$

By defining $\tau' = \tau / k$, eq. 12 becomes:

$$I_D(t) = \frac{W}{L} \cdot \mu_0 \cdot C_{ox} \cdot V_D \left(- a\tau' - V_{th,0} \right) \exp[-(t/\tau')] + \\ + \frac{W}{L} \cdot \mu_0 \cdot C_{ox} \cdot V_D \, a\tau \left[1 - \exp[-(t/\tau')] \right] \,. \qquad (15)$$

The steady state limit of eq. (15) $I_D(t \to \infty) \approx \frac{W}{L} \cdot \mu_0 \cdot C_{ox} \cdot V_D \, a\tau'$ implies that the current contributed only by free-carriers at equilibrium with trapped carriers. This steady-state limit, which can be tuned by means of a, is not probed in this experiment. However, eq. (12) can be exploited to estimate τ' assuming that the mechanism of trapping is time-invariant. In the case of a DC gate bias (corresponding to the limit $a \to 0$, the phenomenology of bias stress is recovered[14]:

$$I_D(t) = \frac{W}{L} \cdot \mu_0 \cdot C_{ox} \cdot V_D \left(- V_{th,0} \right) \exp[-(t/\tau')] \,. \qquad (16)$$

All these topics indicate furthermore the powerfulness of the methodology developed for the study of Δm parameter, since it is clear that the framework on which the eqs. (10) and (11) have been developed contains implicitly information on the features of both trapping phenomenon showed in the dc limit $a \to 0$ (where no triangular sweep takes place but the analysis of the time-decaying I_D current is performed at a fixed operation point) and equilibrium conditions obtained in the steady state limit $t \to \infty$.

In truth, a very interesting indication given by the dynamic analysis of hysteretic phenomena in transfer characteristics regards the possibility of carrying out a sorting of trap states, that is a probing of traps energetically

shallower. More precisely, β=1 has been already ascribed to the different short time scales assumed in the analysis of Δm. To illustrate this aspect it has to be emphasized that the experiment aimed to probe the effect of bias stress is more than an order of magnitude faster than the measurements performed to fit the stretched exponential decay[123]. On this short time scale the relaxation of the carriers into traps is far from equilibrium and it is unlikely that the full range of the trap distribution gets populated. Instead, shallower barriers dominate the kinetics on short time scales as they can be overcome faster. As a consequence, the probed trap distribution becomes narrower and β approaches 1. In this respect, it is clear that in order to probe also the effect deeper trapping states it could be possible to cover a broader distribution of trap states by varying opportunely the time scale. This aspect could furthermore indicate that the nature of trap states probed in the experiment not necessarily has to be related to extrinsic traps. Before to discuss this eventuality, it seems to be necessary to stress another important aspect concerning the kinetics of the experiment. In this respect, even if the exponential distribution of traps has not to be necessarily consistent with stress measurements occurring at long time scale, it is possible to recover the same the stretched exponential relaxation to steady state with experiment performed on short time scales (that is without recurring to long time scales, since in this case the intimate sense of this tool, consisting in the monitoring of trapping mechanisms on shorter timescales compared to those involved in the same mechanisms, can be lost). In detail, this can be made by considering $V_G = -\Delta V_{max} = -|-V_{max}-V_{th,0}|$ with $V_{th,0}$=-17.9 V from eq. (3) in place of $V_G=-V_{max}$. In Fig. 7 the differential logarithimic derivative of I_D current calculated at the turning point (differential transconductance at V_{max}) versus ΔV_{max} for two different scan rates a is shown.

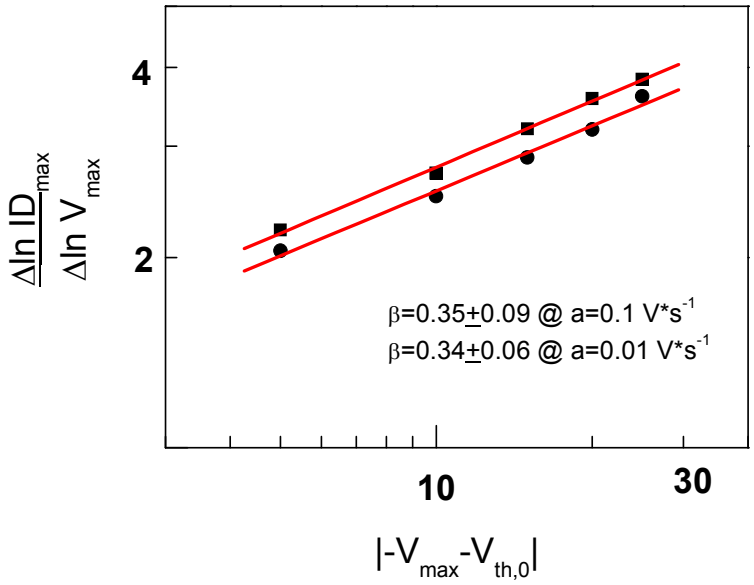

Fig.IV.7: Differential logarithmic transconductance at the turning point vs. ΔV_{max} for scan rate a equal to 0.1 V*sec^{-1} (■) and 0.01 V*sec^{-1} (●). The red lines denote the fitting curves.

The trend exhibited is clearly power law with a best fit exponent equal to 0.35 which is apparently consistent with the stretched exponential distribution of traps[137,140]. At this purpose it has to be pointed out that the recovery of the stretched exponential distribution is attributable to the fact that the offset gate voltage ΔV_{max} represents here the effective population of free carriers, no longer the short time scale of the measurement, as happens in eq. (10) and (11), where the dynamic of trapping is still largely operative.

Finally, the other very important feature emerging from the experiment regards again the extracted value for the parameter β (~1). In fact, as concerns the mentioned nature of the probed traps, β=1 has been ascribed to shallow traps which can be related reasonably to the morphological features of pentacene based device channel. Regarding the effects related to the morphology, one has to consider that OTFTs operate usually on an ultra-thin film (a few monolayer thick)[146], so the accumulation layer

coincides with a large fraction of the film thickness[147,148]. The incomplete coverage of the stacking layers in pentacene results into topographical fluctuations[146,149,150] which enhance the surface area and make accessible to water molecules terrace edges, vacancies, boundaries and dielectric interface. It was recently demonstrated that domain boundaries in pentacene FETs during operations exhibit a different energy distribution with respect to the adjacent pentacene domains[151]. This makes the grain boundaries possible sites for charge carrier trapping.

4.3) A working cause: morphological effects on OFETs properties.

During the discussion emerged in the previous section, a reference to the possibility that the morphological features of pentacene thin films might affect the trapping mechanisms could be deduced. In particular, from the consideration developed in margin of the possible nature of trap states (regarding in detail the trap-depth distribution), it is not precluded that intrinsic trapping mechanisms can affect the overall device response in absence of those environmental conditions responsible of the bias stress phenomena and related hysteretic behavior. In this respect, no direct experimental evidence addressing the bias stress phenomenology to a sort of zero-order trapping mechanism due to intrinsic traps, that is to the intimate nature of the device organic active layers, is showed in literature. In this respect, an analysis of hysteretic behavior in function of the morphological features could be appropriate in order to single out the eventual role of morphology in the bosom of charge trapping mechanisms affecting the performances of organic based devices. This aspect could play a crucial role, since it could supply a criterion suitable for the control of the device stability. Such control can be practiced through a the reduction of sites responsible of trapping operated via the control of film morphology.

Despite the lack of such evidence, it is noteworthy to underline here that several works deal with the morphological effects on charge transport, above all in optics of strategies suitable for the bettering of device performances. This aspect can be however viewed as a starting point o which it is possible to develop instead a tool for studying the morphological influence on charge trapping, rather than on charge transport. Entering into detail of these works, many studies report about the correlation between the morphology and charge transport properties,

indicating in some cases the morphologies that limit an efficient charge transport, while other studies deal with the phase diagram of organics growth with Organic Molecular Beam Deposition (OMBD) technique. In detail, it has been reported for example that there is a correlation between the morphology of a P5 thin film deposited on SiO_2 gate dielectric substrate and the resulting charge carrier mobility μ. In this case μ results to be reduced for a lamellar like morphology for grains, even if any correlation between the grain size and μ has been evidenced[152] although it is commonly believed that grain boundaries have to be regarded as limiting factor for an efficient charge transport[153]. Moreover, also the phase diagram of P5 has been reported[152,154], showing different types of morphologies in function of both the substrate temperature T_{sub} and deposition rate Φ. This aspect represents a milestone for small molecular organics, so the main topic for some groups involved on condensed matter research consists in determining the way in which morphology can be tuned by acting on growth parameters. In truth, very few works deal with the growth of P5 on bare silicon dioxide[154] since the interest of scientists is mainly focused on functionalized substrates. In this respect, functionalization operated via the treatment of both surfaces and injecting electrodes is made mainly for the sake of reaching very promising device performances, but it can act also on thin films morphology. In fact, as concerns the latter case it is possible to act on the surface energy per unit cell, on the interaction between one molecule and the neighboring (001) plane and on the interaction between that molecule and the substrate (all these energies being involved in the final two-dimensional or three-dimensional film morphology), by lowering Φ (i.e. the flux of evaporated molecules) and by increasing at the same time the substrate temperature T_{sub} (corresponding to a decreasing of supersaturation, that is the difference in chemical potential between a molecule in the vapor and a molecule in a bulk crystal), or by functionalizing the substrate. In this respect, it has been

reported that that the higher the supersaturation, i.e., the more energy the system loses during energy minimization by incorporating a molecule into the centre of nucleation during the growth, the fewer molecules are required to form a stable nucleus. So at high supersaturation a stable nucleus will only be one monolayer high and the resulting morphology can be layer-by-layer like[154].

Actually, it seems that the indications furnished by the above mentioned works are often not exhaustive, sometimes even controversial. Just as an example of such assertion, even if it has been reported that the chemical treatment of Si wafers, aimed to obtain both reduced and oxidized surfaces, favors a good nucleation, so that the growth is governed by substrate diffusion, rather than by the inhomogenities (i.e. impurities, roughness), there are some works dealing with SiO_2 or Si_3N_4 (silicon nitride) substrates, with or without a octadecyclltrchlorosilane (OTS) functionalization, in which the growth is mainly governed by substrate temperature instead of the same functionalization[155]. Moreover, in this latter case, only a little difference in bias stress phenomenon has been singled out for the two different dielectrics, addressing the threshold voltage shift to a reversible structural change in P5 (consisting in the creation of deep localized states). So, in this respect no evidence of morphological effects on device stability has been highlighted, in attestation of a remarkable difficulty in addressing experimentally the stress phenomena to the morphological effects.

The above introduced scenario can be explained by the fact that film growth is intrinsically a process away from thermodynamic equilibrium conditions. In fact, only those systems which are close to equilibrium, i.e. high substrate temperature and low deposition flux, can be properly described by a thermodynamic approach. To account for growth scenarios arising from systems far from equilibrium (low substrate temperatures and high deposition rates), kinetic aspects such as adsorption, desorption, interlayer and intralayer diffusions or nucleation have to be

considered[156,157], whereas each of these processes has different activation barriers and the final film morphology is determined by the hierarchy of their barriers, together with the deposition rate and substrate temperature.
On the basis of all the above introduced aspects, it is clear that the understanding of information aimed to draw the line at the growth process (useful, as told above, as starting point for the clarification of the eventual morphological role in the bosom of the device instabilities) requires the utilization of conventional untreated substrates, allowing thus the building of strategies aimed to the overcome of device limiting factors.

4.3.a) Theoretical features of Organic Molecular Beam Deposition (OMBD).

In this section a brief summary of the theoretical background of film growth is presented in order to better clarify the general topics developed above. The film growth is very broad and has been studied under different approaches, since the vacuum deposition techniques play a crucial role in terms of the technological interest in thin films. The theoretical studies and the practical approaches towards the features of organic film growth are undoubtedly crucial for the understanding of thin film properties. Prior to develop the theory concerning the morphological features of organic thin films growth by OMBD, an introduction to such technique is need. Here, just a preliminary compendium of the main technique adopted for the deposition of small molecules and its general technical implications follows.
OMBD technique is universally employed due to the high degree of control that it offers in terms of:

- environmental cleanliness, governed by the very low pressure in the chamber (generally 10^{-6}-10^{-8} mbar);

- film thickness, through the control of growth rate, being this aspect useful above all in the case of sub-monolayer growth;
- deposition parameters such as substrate temperature and evaporation rate, useful for the control of the resulting film morphology[158].

The deposition technique, based on the concept of organic powder sublimation, consists in an exposure of the substrate to a vapor flow of the desired molecules generated by a Knudsen cell.

The Knudsen cell consists in a crucible equipped with a heating filament opportunely thermally shielded, a temperature sensor (generally a thermocouple) used for monitoring the temperature of the cell and a blocking shutter. The orifice of the cell is quite restricted, since in this way the effusion rate depends strictly on the vapor pressure of the evaporating powder, not on its quantity. In this way, by fixing the temperature of the cell, the deposition rate is constant. Moreover, the Knudsen cell allows to regulate the evaporation flow by acting on the crucible temperature, ranging the deposition speed, achieved by means of the Knudsen cell, from 10^{-3} Å/sec to 10^{2} Å/sec. For this reason the evaporation technique is certainly versatile, since it allows to assure both a sufficiently slow and a flash evaporation. This aspect is of paramount importance. In fact, as stated above, a slow deposition favors the control of both the film morphology and, as a consequence, the control of the film properties, while a flesh evaporation is suitable for the contemporary deposition of different materials. In both cases the technique can be exploited for assembling electronic devices completely in situ.

As concerns the theoretical approaches describing the evolution of the film morphology upon film growth, there are three basic scenarios that have to be considered (Fig.8):

- “layer-by-layer” or “Frank-Van der Merwe” growth; the growth of

upper layers starts after the growth of underlying layers is completed[159].

- "island" or "Vollmer-Weber" growth; the deposited material assembles in shape of islands[160].
- "layer-plus-island" or "Stranski-Krastanov" growth; initially a layer-by-layer growth takes places until a critical thickness is reached, above which the island growth starts[161].

Among the approaches used for describing these three modes, there is one due to Bauer[162] which involves the three macroscopic surface tensions of the interfaces in play, that is the overlayer-vacuum interface (γ_0), the overlayer-substrate interface (γ_i), and the substrate-vacuum interface (γ_s). If the surface tensions fulfill the condition $\gamma_o + \gamma_i \leq \gamma_s$, the system is energetically favored if the overlayer completely covers the surface, consequently leading to a layer-by-layer growth. It is worth to reaffirm here that this condition is retained by most researchers as the favorable one in terms of an efficient charge transport, since it foresees the absence of structural defects such as the grain boundaries. If this is not the case, the substrate will be only partially covered, leading to an island growth. Stranski-Krastanov growth takes place if the above condition is initially fulfilled below a critical thickness, thus following a layer-by-layer growth behavior. This growth scenario is often found in heteroepitaxial growth due to the formation of a strained overlayer. The strain accumulated in the overlayer can be considered to contribute to γ_i providing then a monotonic increase of energy with increasing film thickness. Thus, at a critical thickness an unstable situation is reached ($\gamma_o + \gamma_i > \gamma_s$) and the film morphology from a layer-by-layer growth switches to an island-like one (Fig. 8).

Fig. IV.8: Schematic representation of the three different film growth scenarios.

4.3.b) Morphological study of pentacene grown on SiO_2 substrates and correlation with TFTs transport properties.

The study of oligomeric thin films with morphologies tailored by acting on deposition parameters to specific requirements represents a central issue for the comprehension of device response. As stated above, due to the dynamic character of the growth process, the achievement of results indicating the recipe to follow for having a complete control of film morphology, appears at least unlikely. In this respect, in order to fix a principle as close to the ideal case as possible, it could be appropriate to start from very common conditions, such as:

- the use of conventional thermal SiO_2 substrates on which only a standard cleaning procedure is adopted, without recurring to any surface treatment;
- the appropriate respect of time allotment elapsing among the sequential steps involved in the film manufacturing process.

For this reason, in this section a study regarding the morphological features of pentacene thin films grown on SiO_2 substrates and the correlation with the relative TFTs transport properties will be shown in the respect of the above conditions. To this end, a series of samples consisting in pentacene based TFTs has been prepared and characterized both electrically and morphologically. In detail, 6ML of pentacene have been deposited by

OMBD on thermal SiO_2 substrates with lithographed interdigitaded test patterns (already described in Chapter III), cleaned as follows: immersion in acetone vapors in order to remove the polymeric layer used for preserving the dielectric surface, then processing by a piraña etching for 15 minutes (1:2 solution of sulfuric acid H_2SO_4 in hydrogen peroxide H_2O_2 for removing the) in order to remove residual polymeric coating and, finally, immersion for 5 seconds in a 4% based fluoridric acid (HF) solution in order to reduce the roughness of the starting substrates (which have been checked in some cases to be comparable with the height of 1ML of pentacene).

The film deposition has been carried out by keeping the substrate temperature fixed at 60 °C, since several reports have used such temperature as the optimized substrate temperature for pentacene growth[163,164] . The deposition rate has been ranged from 0.03 Å/sec (0.12 ML/min) to 3 Å/sec (12 ML/min).

The morphology of the manufactured films has been characterized by collecting sample images using an Atomic Force Microscope and processing then such images by a Gwyddion modular program for scanning probe microscopy data visualization and analysis. A complete description of morphological features has been provided by the Power Spectral Density Fourier (PSDF) of the surface topography. PSD consists in a decomposition of the surface profile of collected images into its spatial wavelengths, operated by performing the Fourier transform of such profile. The PSD plot of a surface reveals then the presence of periodic structures in that surface, so it is able to quantify the correlation length ξ of the obtained morphological structures, that is the size of each grain or island composing the film which, in turn, can be identified with the mean distance between two adjacent nucleation sites. Finally, the analysis of the electrical response has been carried out by recording the transfer characteristics of the manufactured devices, extracting then some device

parameters such as μ and V_{th} and correlating them to the obtained morphological features (the latter parameter will be treated in section 4.3.c)).

The experimental results have indicated some interesting features. In Figs. 9, 10 and 11 AFM images and related PSDFs are reported for three different deposition rates.

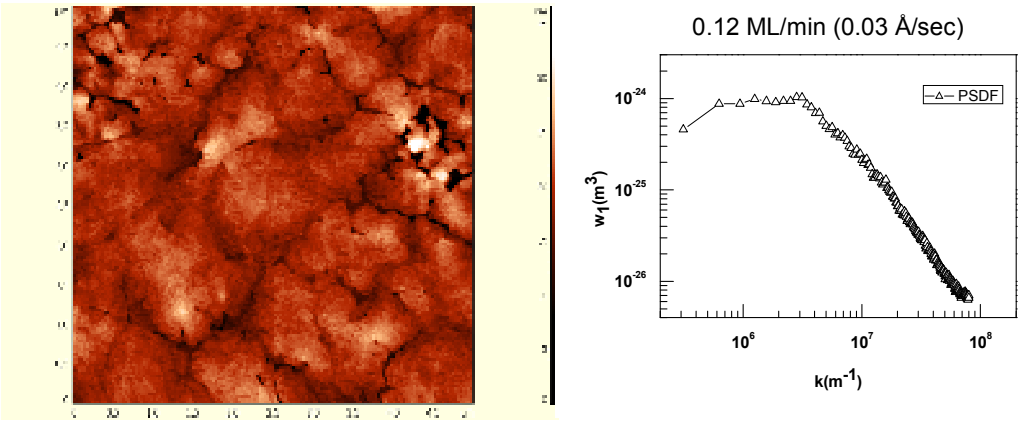

Fig.IV.17: AFM image and PSDF of a P5 sample growth at 0.03Å/sec and fixing the substrate temperature at 60°C.

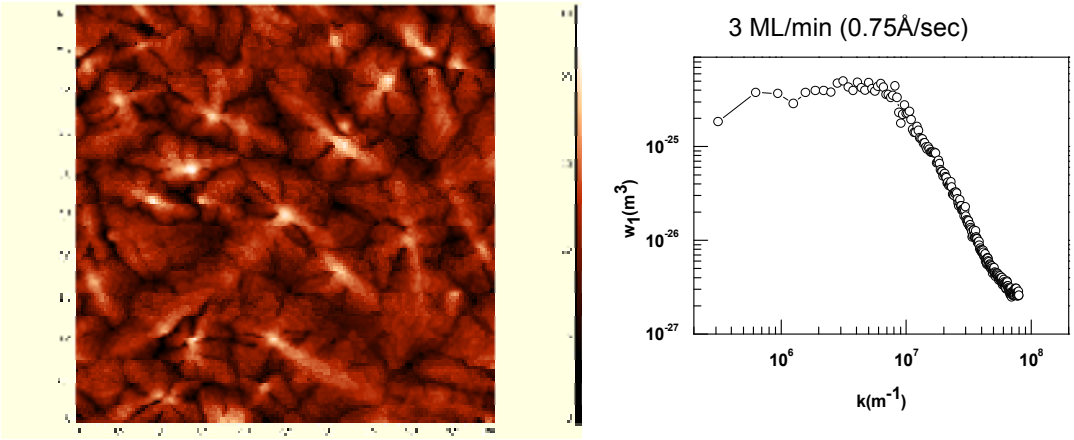

Fig.IV.10: AFM image and PSDF of a P5 sample growth at 0.75 Å/sec and fixing the substrate temperature at 60°C.

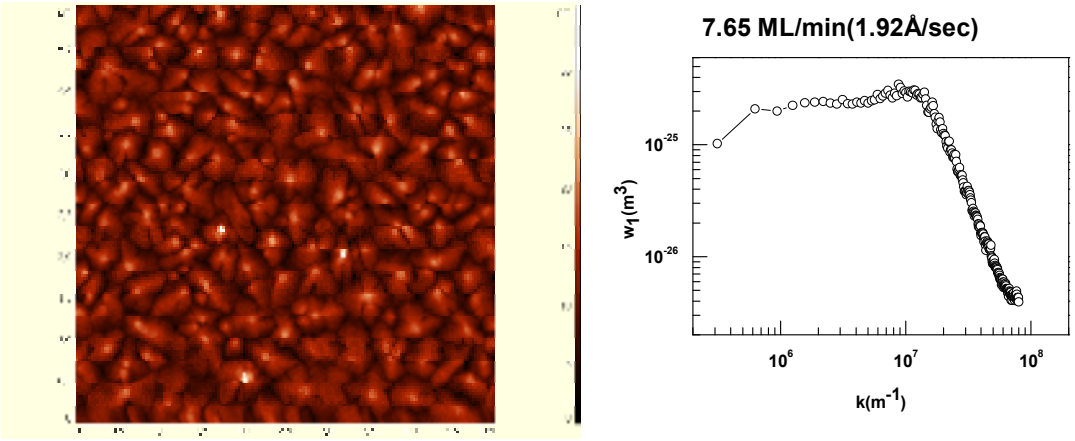

Fig.IV.11: AFM image and PSDF of a P5 sample growth at 1.92 Å/sec and fixing the substrate temperature at 60°C.

These results indicate that each of the above collected images corresponds to one characteristic morphology. In detail, three main categories of film morphology can be deduced:

- at lower deposition rates, up to 0.12 Å/sec, it is found a giant grain morphology, that is a morphology tending to the layer by layer one, where terraces with ξ>1μm are singled out; in this case it is worth to note that the chosen scan scale for the collection of AFM images is comparable with the correlation length;
- for deposition rates ranging from 0.12 Å/sec to 0.75 Å/sec dendritic grains with ξ ranging between 0.5 μm and 1 μm has been found;
- for higher deposition rates a mixed morphology whit small grains and dendrites, characterized by a correlation length less then 0.5 μm, has been found.

The collection of the observed behaviors can be well displayed in a plot of correlation length versus deposition rate (Fig.12). As a result, in this case it is clear that the correlation length ξ decreases by increasing the deposition rate Φ following a trend already stated in the case of Alq_3 growth[165]. In this case, by a fitting procedure, it follows:

$$\xi \approx \Phi^{-0.2}. \qquad (17)$$

The trend showed in Fig.12 is however non perfectly monotonic due to some possible fluctuations on deposition parameters introduced in phase of synthesis. This evidence for sure confirms that the control of growth is a crucial topic for obtaining at least reproducible results.

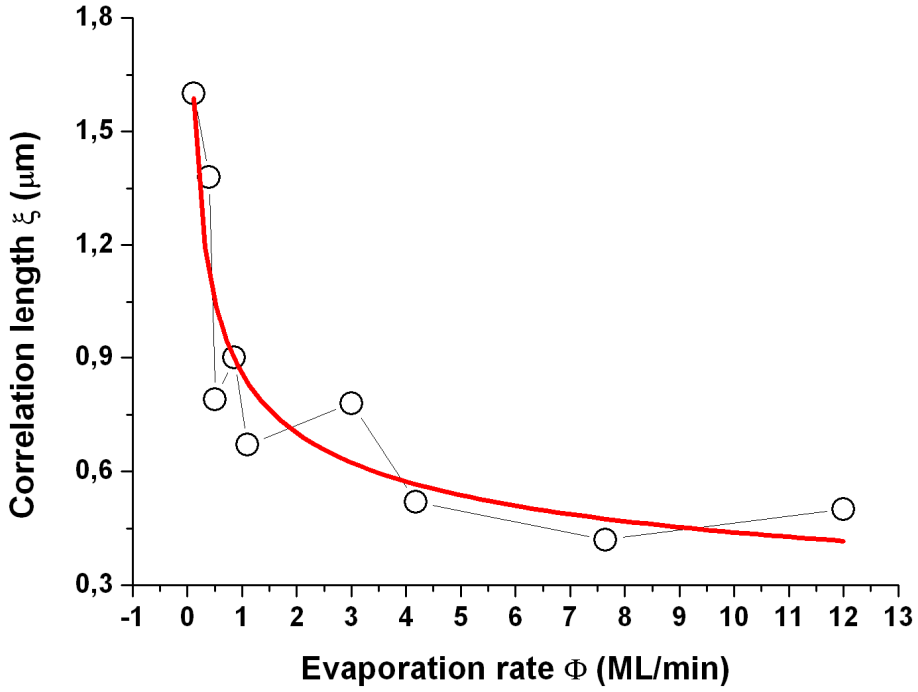

Fig.IV.12: Correlation length vs. deposition rate (expressed in ML/min) .

The electrical characterization has been performed instead by recording both in vacuum (10^{-5}mbar) and in air the transfer characteristics in saturation regime, that is by fixing the channel voltage at -40V and by sweeping the gate voltage from 40V to -40V, returning then to 40V.

The field effect mobility and the threshold voltage have been extracted from the measured transfer characteristics. The typical transfer characteristics recorded for the sample growth at 0.75 Å/sec is reported in Fig. 13.

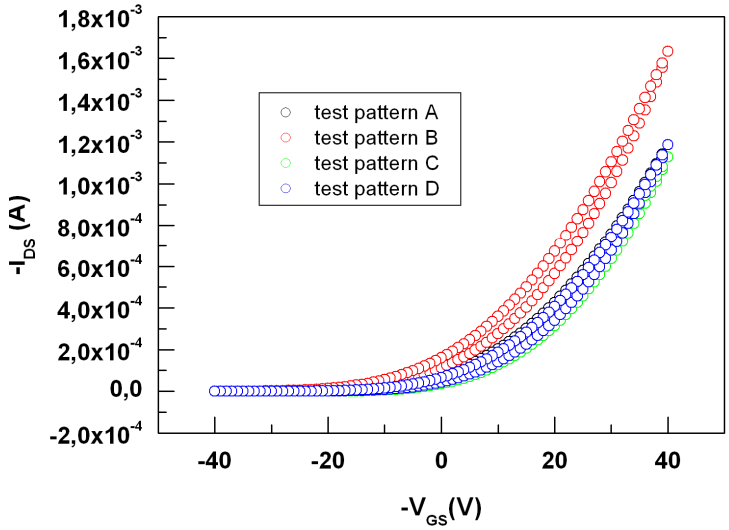

Fig.IV.13: Typical transfer characteristics recorded for the sample grown at 0.75 Å/sec. As it is shown, the different test patterns, characterized by the same geometrical factor, show a current with a nearly equal current. Such evidence implies a scarce effect of contact resistances in the measured devices.

Both the morphological and transport parameters extracted are summarized in table I.

In Fig. 14 the mobility values reported in tab.I versus the deposition rate have been plotted for all the analyzed samples. It is clear that the mobility tends to increase with Φ, showing a peak at 0.75 Å/sec which corresponds to the a perfect dendritic morphology, while the mobility for small grains still remains higher with respect its values extracted for samples with a terrace-like morphology.

Deposition rate	**Morphology**	**Correlation length (µm)**	**Mobility (cm2*V-1*s-1)**
0.12 ML /min (0.03)Å/sec	Giant grain (terrace)	1.6	0.0065
0.4 ML/min (0.1) Å/sec	Giant grain (terrace)	1.38	0.048
0.5 ML/min (0,125) Å/s	Dendritic	0.79	0.0305
0.86 ML/min (0,215) Å/s	Dendritic	0.9	0.0315
1,1ML/min (0.275) Å/s	Dendritic	0.67	0.0445
3ML/min (0.75 Å/s)	Dendritic	0.8	0.13
4.18ML/min (1.04 Å/s)	Grains/dendritic	0.52	0,12
7.65 ML/min (1.92 Å/s)	Grains/dendritic	0.42	0,1015
12ML/min (3 Å/s)	Grains/dendritic	0.54	0,07

Tab. IV.1: Morphologicl and transport parameters extracted by the performed measurements.

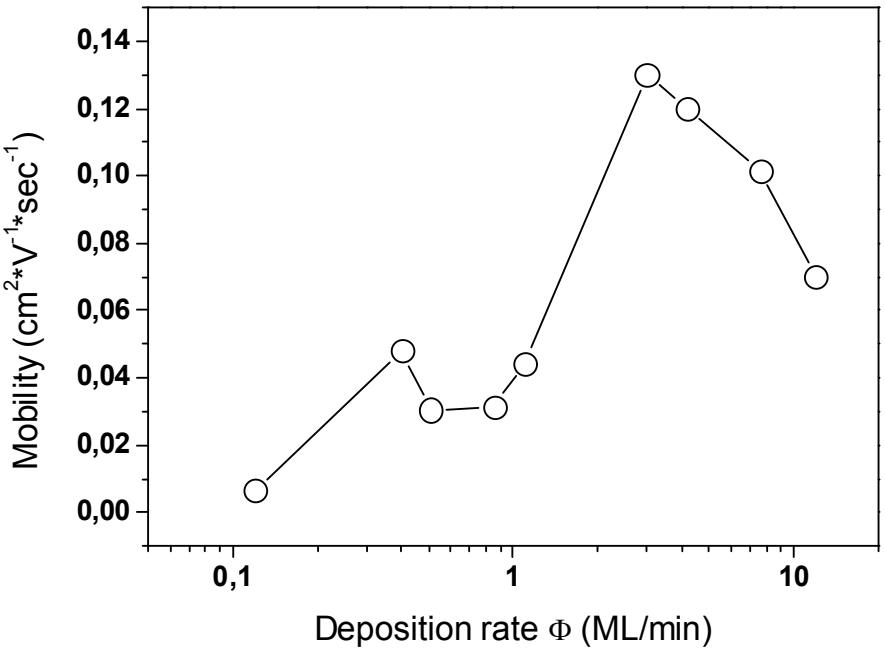

Fig.IV.14: Mobility vs. deposition rate for the analyzed samples.

Of course the choice of Φ as independent variable is dictated by the non monotonic behavior of ξ versus the same Φ. But, it is a matter of fact that μ increases for high deposition rates and, correspondingly, for low correlation lengths. In this case, the upper limit 0.75 Å/sec for T_{sub} equal to 60 °C has been reported to be correspondent to morphological transition between a three-dimensional and a two-dimensional morphology[154]. The low mobility values recorded for apparently two-dimensional films seems to be in contrast with the results waited in the case of well interconnected films. In truth, the morphology obtained at lower deposition rates shows some discontinuities corresponding to the break of film continuity (in particular, some profound creeks and substrate regions showing defects (voids) have been evidenced in this case).

4.3.c) Future developments: trapping phenomena versus morphology.

As regards the threshold voltage V_{th}, its behavior with respect Φ (Fig. 15) indicates that V_{th} undergoes a transition to negative values at high deposition rate/low correlation length.

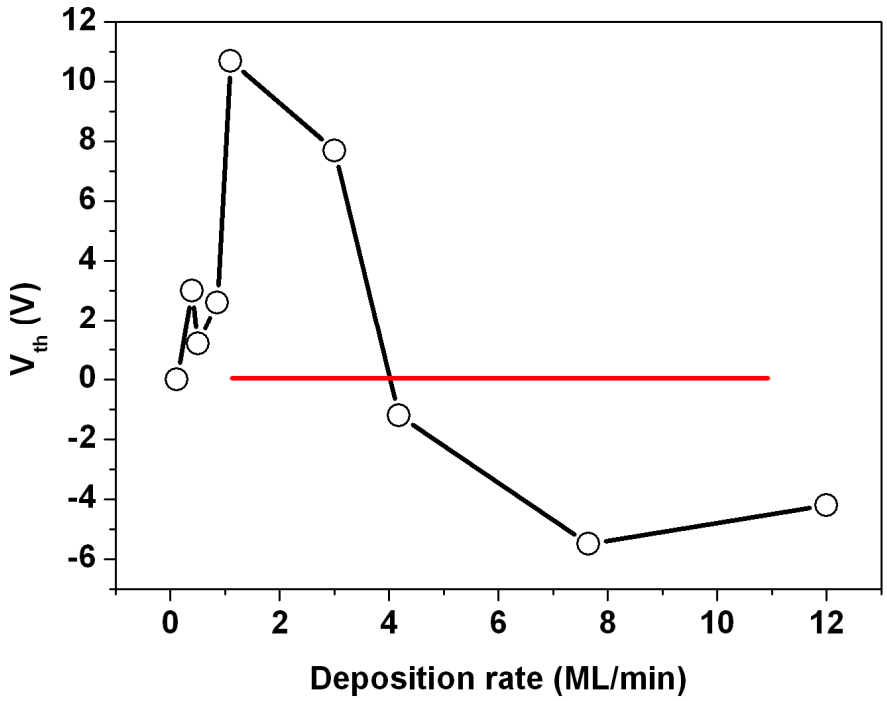

Fig.IV.15: Threshold voltage vs. correlation lengths plot; the red line corresponds to V_{th}=0.

This aspect may be interpreted as an evidence of the morphological influence on charge transport. In brief, remembering that for hole transport materials the bias stress and the charge trapping correspond to a shift of threshold voltage towards positive values, in correspondence of the transition of threshold voltage towards negative values occurred at high deposition rates (or low correlation lengths) the mobility is high and the hysteresis in transfer characteristics measured in air tends to decrease. In this latter case, the lowering of Δm parameter versus ξ is not shown here since its behavior is almost fluctuating, due to the fluctuations induced by deposition procedure on this Φ dependent variable. Nonetheless, an indication of a clear increase of such parameter with the increasing correlation lengths can be evidenced (the lower and the higher adimensional differential logarithmic transconductance defined in eq. (10)

in this case differ one another by a factor 5), together with its saturation at giant grain-like morphology (ξ>1μm).

Of course, these preliminary results, together with other studies regarding the shift of threshold voltage in sexithiophene (T6) based TFTs (where the classical technique, that is the evaluation of ΔV_{th}, has been employed), indicate that morphology can influence the trapping mechanisms. In particular, TFTs based on more and more thick T6 films, in which the accumulation layer is therefore protected from a direct contact with environmental humidity by the upper layers, it has been observed that these upper layers can influence the trapping, since the parameter β scales by increasing the film thickness. So, again a morphological feature consisting in this case in the presence of several interfaces separating the various T6 layers plays an active role in device stability. Nonetheless, the parameter Δm seems to be very sensitive to the environmental changes, so it is for sure a promising and practical tool for clarifying some aspects concerning the phenomenology of unstable devices. Of course, further studies in which a high control of morphology has to be kept in consideration are needed for comprehending better the practical effects played by these important phenomena, also in the optics of their fascinating intimate meaning. In fact, many other basic mechanisms affecting device performances can be framed in a clearer context if investigated separately and correlated to the overall device response.

Conclusions.

To summarize, in this thesis some protocols of dynamic electrical measurements have been introduced to characterize organic materials and related devices. In this way, the peculiar transport and structural material properties, their effect on device performances, the study of the typical device parameters and the contribution of interfaces composing the same devices on their response, have been studied by these tools, very suitable for assessing the role played by the local effects on the recorded overall electrical response. The analysis based on these protocols allows to probe these effects in a non invasive and precise way.

Although the protocols of dynamic techniques of electrical characterization have been extensively applied for the analysis of standard electronic devices, their extension to the case of devices based on novel, unusual materials is not so obvious, as happens instead for dc measurements.

The very important feature of dynamic measurements is the capability of discriminating the nature of those mechanisms that concur cooperatively to a given particular property of the analyzed materials and devices, being this aspect very important in the case of disordered materials. For this reason, the comprehension of some tools of dynamic electrical characterization and the following adaptation of these protocols of measurements to the case of organic semiconductors and dielectrics, both represent the central core of the present work of thesis.

In accordance with the proposal just above indicated, the physical and mechanical properties of organic conductive and dielectric materials, the working mechanisms of organic based devices and the negative effects of both extrinsic and intrinsic factors on device response have been widely treated recurring to both conventional (Impedance Spectroscopy, C-V measurements) and novel dynamic electrical measurements.

In this respect, the analysis carried out via conventional techniques on bare materials has regarded:

- the local character of charge carrier transport in semiconducting polithiophenes, carried out via IS by comparing the experimental results with the predictions of the Universal Dielectric response model, showing that the quantum mechanical tunneling are relevant at lower temperatures and the thermally activated hopping mechanisms between localized states dominate the charge transport at higher temperatures;
- the study of the glassy phase transition of silicon based dielectrics (PDMS) and porous, hydrophilic polysilsequioxanic materials (POSS) performed by means of IS (which is a non invasive and very sensitive criterion), that is by monitoring the relaxation phenomena produced by the phase transitions. In this case, the glass transition temperature of PDMS extracted by the electric criterion is in good agreement with literature data, while the value extracted for POSS represents the first experimental datum for such parameter, not yet reported in literature.

However, the study of device properties has then regarded:

- the effect of glass transition on humidity sensors fabricated using the POSS based materials deposited on interdigitated electrodes, being in this case the basic mechanism used for the description of device operation properties well supported by such transition;
- the optical failure occurring in one of the most conventional organic light emitting devices (whose structure is ITO/TPD/Alq_3/Al) due to a glass transition occurred in one of the two organics (the TPD) employed as device active layers, which is provoked on its turn by a field induced local thermal heating;
- the role of the interfaces between the manganite (LSMO) based injecting electrode and the organic material (Alq_3) in terms of the

promising magnetoresistive effects showed by such interface in spintronic devices. In detail, the contribution of the LSMO/Alq_3 interface has been visualized in the well known equivalent circuit representation as an extra RC parallel element. Such element has allowed to explain the high magnetoresistive effect, in the context of a qualitative model, generally showed by the valves at lower temperatures;

- The employment of C-V techniques, widely used for the characterization of conventional TFTs, has been exploited instead for assessing in a precise way both the static and dynamic parameters of pentacene based TFTs. In particular, the contact resistances R_c, usually very considerable in the case of OTFTs, and the maximum operation frequency ν_{max} of such devices have been extracted in the context of a transmission line model. In detail the evolution of the material capacitance in function of a dc gate bias and the frequency dependent capacitance for gate voltages at which the TFT is in accumulation mode have been monitored and correlated to R_c and ν_{max}, respectively.

Since the role of TFTs in the bosom of organic electronics is relevant, beyond the choice of standard dynamic measurements for evaluating the intrinsic device parameters and their weight in the economy of the overall response, a novel dynamic method has been employed also for the study of device degradation mechanisms, that is the stress phenomena upon the device polarization. In detail, a dynamic approach consisting in correlating the charge carrier trapping (responsible of the bias stress) with the emergence of hysteretic phenomena occurred in the measured device transfer characteristics, has been exploited at this purpose. The strong points of such criterion are represented both by the possibility of reducing the temporal duration of the experiment (reducing in this way also eventual parasitic effects) and by the possibility of introducing a very sensitive

parameter related to the hysteresis. This latter aspect, in particular, has opened the way towards the study of the possible action of intrinsic effects on stress phenomena that can be related to the morphological features. In this respect, the effect of the morphological features (grains, terraces) on device parameters (mobility and threshold voltage) have been performed in order to fix a landmark on which it is possible to develop the study of the stress induced by the film morphology. The analysis indicates the strong dependence of the device response on a morphological parameter, the correlation length (which can be identified with the mean distance between two adjacent nucleation sites).

References.

[1] J. Mc Ginness; Science **177**, 896 (1972).

[2] J. McGinness, P. Corry, and P. Proctor; Science, **183**, 853 (1974).

[3] http://www.nobelprize.org/chemistry/laureates/2000/chemadv.pdf

[4] J. H. Burroughes, D. D. C. Bradley, A. R. Brown, R. N. Marks, K. Mackay, R. H. Friend, P. L. Burn, A. B. Holmes; Nature **347**, 539 (1990).

[5] G.Horowitz, D. Fichou, X. Peng, Z. Xu, F. Garnier ; Solid State Commun. **72,** 381 (1989).

[6] A.Tsumura, H. Koezuka, and T. Ando; Appl. Phys. Lett. **49**, 1210 (1986).

[7] E. Bystrenova, M. Jelitai, I. Tonazzini, A. Lazar, M. Huth, P. Stoliar, C. Dionigi, M. G. Cacace, B. Nickel, E. Madarasz, F. Biscarini; Adv. Funct. Mater. **18**, 1751 (2008).

[8] Y. Yamamoto, K. Yoshino and Y. Inuishi; J. Phys. Soc. Jpn. **47**, 1887 (1979).

[9] N.F. Mott; Phyl. Mag. **19**, 835 (1969).

[10] M. C. J. M. Vissenberg, M. Matters; Phys. Rev. B **57**, 12 964 (1998).

[11] A. Brown, C. Jarrett, D. de Leeuw, and M. Matters; Synth. Met. **88**, 37 (1997).

[12] M. Barra, M. Biasiucci, A. Cassinese, P. D'Angelo, A.C. Barone, A. Carella and A. Roviello; J. Appl. Phys. **102**, 093712 (2007).

[13] A.I Laktos and J. Mort; Phys. Rev. Lett. **21**, 1444 (1968).

[14] S.M. Sze; Physics of semiconductor devices; Ed. John Wiley & Sons; New York (1981).

[15] H. Ishii, K. Sugiyama, E. Ito, K. Seki; Adv. Mater. **11**, 605 (1999).

[16] H. Ishii , N. Hayashi , E. Ito , Y. Washizu , K. Sugi , Y. Kimura , M. Niwano , Y. Ouchi , K. Seki, Phys. Status solidi (a) **201**, 1075 (2004).

[17] K.L. Jensen, J. Vac. Sci. Tech. B **21**, 1528 (2003).

[18] H.K. Henisch, Metal Rectifiers, Oxford University Press, New York, 1949.

[19] N.F. Mott and R.W. Gurney, Electronic Processes in Ionic Crystals, Oxford Press (1940).

[20] A. Carbone, B. K. Kotowska, D. Kotowski; Phys. Rev. Lett. **95**, 236601 (2005).

[21] S. Berleb and W. Brütting, Phys. Rev. Lett. **89**, 286601 (2002).

[22] H.C.F. Martens, H.B. Borm and P.W.M. Blom, Phys. Rev. B **60**, 8489 (1999).

[23] Petty M.C.; Pearson C.; Monkman A.P.; Casalini R.; Capaccioli S.; Nagel J., Colloids and Surfaces A: Physicochemical and Engineering Aspects **171**, 159 (2000).

[24] M. Glatthaar , N. Mingirulli , B. Zimmermann , T. Ziegler , R. Kern , M. Niggemann , A. Hinsch , A. Gombert; Phys. Satus Solidi (a) **202**, 125 (2005).

[25] J.K. Vij, W.G. Scaife, J.H. Calderwood; J. Phys. D: Appl. Phys. **11,** 545 (1978).

[26] R. Kronig, J. Opt. Soc. Am. **12**, 547 (1926).

[27] H.A. Kramers, Congresso Internazionale di Fisici Como (Zanichelli, Bologna, 1927).

[28] The current produced by a varying voltage $V(t) = V_0 e^{j\omega t}$ applied to a material sandwiched between two plane plates (capacitor with surface and distance of plates equal to S and d, respectively), will be given by $I = \varepsilon^* C_0 \left(\frac{dV}{dt} \right) = j\omega\varepsilon^* C_0 V = \omega C_0 (\varepsilon' - \varepsilon'') V$ (where the expressions $\varepsilon^*(\omega) = \varepsilon'(\omega) - j\varepsilon''(\omega)$ and $C = (\varepsilon^* C_0) = \frac{Q}{dV}$ have been used). So, extending the Ohm's law to the ac case, both a capacitive component I_C (given by $I_C = j\omega C_0 \varepsilon' V$ with a phase shift of 90° with respect the applied voltage) and a resistive component I_R (given by $I_R = \omega C_0 \varepsilon'' V$, in phase with the varying voltage) of the current will be produced inside the material. Therefore, by exploiting Ohm's law, it is possible to obtain: $\frac{I_R}{V} = G = \sigma \left(\frac{S}{d} \right) = C_0 \omega \varepsilon'' = \varepsilon \left(\frac{S}{d} \right) \omega \varepsilon''$, where $\varepsilon = \varepsilon_0 \varepsilon_r$ is the 'dielectric constant' of the analyzed medium. So, it can be easily deduced that $\varepsilon'' = \frac{\sigma}{\varepsilon\omega}$.

[29] A.K. Jonscher; Nature **267,** 673 (1977).

[30] S. R. Elliott; Adv. Phys. **36**, 135 (1987).

[31] I.G. Austin and N.F. Mott; Adv. Phys. **18**, 41 (1969).

[32] R.C. Hughes; Phys. Rev. B **15**, 2012 (1977)

[33] S.R. Elliot; Phyl.Mag.B **37**, 553 (1978)

[34] N.F. Mott and E.A. Davis; Electronic processes in non-crystalline materials, Clarendon Press, Oxford, 1971.

[35] C.G. Kuper and G.D. Whitfield; Polarons and Excitons, Oliver and Boyd, Edinburgh, 1963.

[36] V. Bobnar, A.Levstik, C. Huang and Q.M. Zhang; Phys. Rev. Lett. **92**, 047604 (2004).

[37] M.Pollak and G.E. Pike; Phys. Rev. Lett. **28**, 1449 (1972).

[38] M. D. Austin and S. Y. Chou; Appl. Phys. Lett. **81**, 4431 (2002).

[39] S. M. Sze; Physics of Semiconductor Devices, Wiley, New York 1981.

[40] B. H. Hamadani, C. A. Richter, J. S. Suehle, and D. J. Gundlach; Appl. Phys. Lett. **92**, 203303 (2008).

[41] D. James, S. M. Scott, Z. Ali, and W. T. O'Hare; Mikrochim. Acta **149**, 1 (2005).

[42] D. T. Eddington, R. H. Liu, J. S. Moore and D. J. Beebe; Lab Chip **2**, 96 (2001).

[43] X. Peng, G. Horowitz, D. Fichou and F. Garnier; Appl. Phys. Lett. **57**, 2013 (1990).

[44] D. W. Hatchett, M. Josowicz, J. Janata and D. R. Baer, Chem. Mater. **11,** 2989 (1999).

[45]C.W. Tang and S.A.VanSlyke; Appl. Phys. Lett. **51,** 913 (1987).

[46] N.S. Sariciftci, L. Smilowitz, A.J. Heeger, F. Wudl, Science **258**, 1474 (1992).

[47] V. Dediu, M. Murgia, F.C. Matacotta, C. Taliani, S. Barbanera, Sol. State Commun., **122,** 181 (2002).

[48] Z.Zhang and M.G. Lagally; Science **276**, 276 (1997).

[49] P.W.M. Blom and M.J.M. deJong, Philips J. Res. **51**, 479 (1998).

[50] L. Ma and Y. Yang; Appl. Phys. Lett. **85**, 5084 (2004).

[51] M. Matters, D.M. de Leeuw, P.T. Herwig and A.R. Brown; Synth. Met.,**102**, 998 (1999).

[52] A.F. Mayadas and M. Shatzkes; Phys. Rev. B **1**, 1382 (1970).

[53] Ward C. Sumpter, Chemical Reviews **34,** 393 (1944).

[54] H. Sirringhaus, N. Tessler, R. H. Friend, Science **280**, 1741 (1998).

[55] A. Babel, S.A. Jenekhe, Synthetic Metals **148**, 169 (2005).

[56] Y.D. Park D H. Kim, Y. Jang, J. Ho Cho, M. Hwang, H. S. Lee, J. A. Lim, K. Cho; Organic Electronics **7**, 514 (2006).

[57] O. Haba, T. Hayakawa, M. Ueda, H. Kawaguchi, and T. Kawazoe, React. Funct. Polym. **37**, 163 (1998).

[58] A. Roviello, A. Buono, A. Carella, G. Roviello, A. Cassinese, M. Barra, and M. Biasiucci, J. Polym. Sci., Part A: Polym. Chem. **45** (9), 1758 (2007).

[59] R . D. McCullough, R. D. Lowe, D. Jayaraman, and M. Anderson, J. Org. Chem. **58**, 904 (1993).

[60] O. Haba, T. Hayakawa, M. Ueda, H. Kawaguchi, and T. Kawazoe, React. Funct. Polym. **37**, 163 (1998).

[61] M. R. Andersson, D. Selse, M. Berggren, H. Järvinen, T. Hjertberg, O.Inganäs, O. Wennerström, and J. E. Österholm, Macromolecules **27**, 6503 (1994).

[62] M.S.A. Abdou, F.P. Orfino, Z.W. Xie, M.J. Deen, S. Holdcroft, Adv. Mater. **6**, 838 (1994).

[63] E.J. Meijer, C. Detcheverry, P.J. Baesjou, E. van Veenendaal, D.M. Leeuw, T.M. Klapwijk, J. Appl. Phys. **93**, 4831 (2003).

[64] D.M. Russell, T. Kugler, C.J. Newsome, S.P. Li, M. Ishida, T. Shimoda; Synthetic Metals **156**, 769 (2006).

[65] S. K. Dwivedi, A. Kumar and S. Kumar; Adv. Mater. Opt. Electron. **9**, 234 (1999).

[66] M.A. Majeed Khan, M. Zulfequar and M. Husain; Physica B **366**, 1 (2005).

[67] J. A. Geurst, Phys. Status Solidi **15**, 107 (1966).

[68] W. A. Phillips, Phil. Mag.B **43**, 747 (1981).

[69] D. Emin, T. Holstein, , Ann. Phys., N.Y. **53**, 439 (1969).

[70] V. Bobnar, A. Levstik, C. Huang, and Q. M. Zhang, Phys. Rev. B **71**, 041202 (2005).

[71] T. Dollase, H. W. Spiess, M. Gottlieb and R. Yerushalmi-Rozen., Europhys. Lett. **60**, 390 (2002).

[72] P. G. Debenedetti and F. H. Stillinger, Nature (London) **410**, 259 (2001).

[73] M. Nicodemi and H. J. Jensen, Phys. Rev. Lett. **86**, 4378 (2001).

[74] J. D. Mc Coy, J. G. Curro, J. Chem. Phys. **116**, 9154 (2002).

[75] J. L. Keddie, R. A. L. Jones, and R. A. Cory, Europhys. Lett. **27** 59 (1994).

[76] C. Kim, A. Facchetti, T.J. Marks; Science, **318**, 76 (2007).

[77] J. Kaifeng, J. F. Loeffler, Appl. Phys. Lett. **86**, 241909 (2005).

[78] D. Wallacher, V. P. Soprunyuk, K. Knorr, and A. V. Kityl, Phys. Rev. B **69**, 134207 (2004).

[79] D. Wallacher, V. P. Soprunyuk, K. Knorr, and A. V. Kityl, Phys. Rev. B **66**, 014203 (2002).

[80] H. B. Brom, I. G. Romijn, J. G. Magis, M. Van der Vlenten, and M. A. J.Michels, Appl. Phys. Lett. **85**, 570 (2004).

[81] Show An Chen, H. T. Lee, Macromolecules **28**, 2858 (1995).

[82] T. Sugihara, K. Fujii, H. Haga, and S. Yamamoto, Appl. Phys. Lett. **69**, 2971, (1996).

[83] V. Podozorov, V. M. Pudalov, M. E. Gershenson, Appl. Phys. Lett. **82**, 1739, (2003).

[84] J. Mark, Polymer Data Handbook Oxford University Press, New York, (1999).

[85] J. P. Johari and C. Ferrari, J. Phys. Chem. B **101**, 10191 (1997).

[86] Polymers in Sensors: Theory and Practice (Acs Symposium Series), Naim Akmal and Arthur M. Usmani, Oxford University Press, 1998.

[87] A. G. MacDiarmid. Synth. Met. **84**, 27 (1997).

[88] E. Laukhina, V. Laukhin, M. Mas-Torrent, C. M. Creely, D.V. Petrov, J. Veciana, C. Rovira; IEEE proceeding of the conference TRANSDUCERS & EUROSENSORS '07, pp. 2247-2249 (2007).

[89] B. Adhikari, S. Majumdar, Prog. Polym. Sci. **29**, (2004) 699.

[90] H. Bhai and G. Shi; Sensors, **7**, 267 (2007).

[91] Y. Sakai, Y. Sadaoka, M. Matsuguchi, J. Electrochem. Soc. **136**, 171 (1989).

[92] 5V. Parra, Á. A. Arrieta, J. A. Fernández-Escudero, H. García, C. Apetrei, M. L. Rodríguez-Méndez, and J. A. de Saja, Sens. Actuators B **115**, 54 (2003).

[93] C.Zhang, F. Babonneau, C. Bonhomme, R.M. Laine, C. L. Soles, H. A. Hrisov, A.F. Yee, J. Am. Chem. Soc. **120**, 8380 (1998).

[94] H.Xu, S. WeiKuo, F-C Chang, Polymer Bullrtin **48**, 469 (2002).

[95] E.T.Kopesky, T.S. Haddad, R. E. Cohen, G.H. McKinley, Macromolecules **37**, 8992 (2004).

[96] A. Castaldo, E. Massera, L. Quercia, G. Di Francia, Macromolecular Symposia **247**, 350 (2007).

[97] P. D'Angelo, M. Barra, M. Nicodemi, A. Cassinese, J. Appl. Phys. **101**, 044910 (2007).

[98] S. Tokito, H. Tanaka, K. Noda, A. Okada and Y. Taga, IEEE Transaction on Electron Devices, **44**, 1239 (1997).

[99] K.A. Osipov, V.N. Pavlovskii, E.V. Lutsenko, A.L. Gurskii, G.P. Yablonskii, S. Hartmann, A. Janssen, H.-H. Johannes, R. Caspary, W. Kowalsky, N. Meyer, M. Gersdorff, M. Heuken, P. van Gemmern, C. Zimmermann, F. Jessen, H. Kalisch, R.H. Jansen; Thin Solid Films **515**, (2007) 4834.

[100] C.Kim, A. Facchetti, T.J. Marks; Science **318**, 76 (2007)

[101] J. L. Keddie, R. A. L. Jones, R. A. Cory; Europhys. Lett. **27**, 59 (1994).

[102] D. Y. Kondakov et al; J. Appl. Phys. **93**, 1108 (2003).

[103] Z. H. Xiong, Di Wu, Z. Valy Vardeny and Jing Shi, Nature **427**, 821 (2004).

[104] S. Majumdar, E. Laiho, P. Laukkanen, I.J. Varrynen, H.S. Majumdar, R. Obsterbacka, Appl. Phys. Lett. **89**, (2006) 122114.

[105] V. Dediu, M. Murgia, F. C. Matacotta, C. Taliani and S. Barbanera, Solid St. Commun. **122**, 181 (2002).

[106] W. Brutting, S. Berleb, A.G. Muckl, Org. Elec. **2**, 1 (2001).

[107] A. Moliton, W. Rammal, B. Lucas, Eur. Phys.: J. Appl. Phys. **33**, 175 (2006).

[108] M.P. de Jong, V. Dediu, C. Taliani, W.R. Salaneck, J. Appl. Phys. **94**, 7292 (2003).

[109] L.E. Hueso, I. Bergenti, A. Riminucci, Y. Zhan, V. Dediu, Adv. Mater., **19**, 2639 (2007).

[110] A.S. Wan, A.J. Makinen, P.A. Lane, G.P. Kushto, Chem. Phys. Lett. **446**, 317 (2007).

[111] H. Ishii, K. Sugiyama, E. Ito, K. SEki, Adv. Mater. **11**, 605 (1999).

[112] M.A. Baldo, S.R. Forrest, Phys. Rev. B **64**, 085201 (2001).

[113] J.H. Park, E. Vescovo, H.J. KIm, C. Kwon, R. Ramesh, T. Venkatesan, Phys. Rev. Lett. **81**, 1953 (1998).

[114] J.F. Ren, J.Y. Fu, D.S. Liu, L.M. Mei, S.J. Xie, J. Appl. Phys. **98**, 074503 (2005).

[115] A. Stadler, M. Burghart; IEEE Transactions on Dielectrics and Electrical Insulation; **13**, 850 (2006).

[116] N. Koch, Chem. Phys. Chem, **8**, 1438 (2007)

[117] S. Pratontep, M. Brinkmann, F. Nuesch, L. Zuppiroli; Synth. Met. **146**, 387 (2004).

[118]N. Camillone III, C. E. D. Chidsey, P. Eisenberger and P. Fenter; J. Chem. Phys. **99**, 744 (1993)

[119] R. Schmechel and H.V. Seggern; Phys Stat Sol (a) **201,** 1215 (2004)

[120]L Li, G. Meller and H. Kosina; Solid State Electr. **51**, 445 (2007).

[121] Jean-Pierre Farges; Organic Conductors: Fundamentals and Applications; CRC Press, 1994.

[122] M. Matters, D.M. de Leeuw, P.T. Herwig and A.R. Brown; Synth. Met. **102**, 998 (1999).

[123] S. G. J. Mathijssen, M. Cölle, H. Gomes, E. C. P. Smits, B. De Boer, I. McCulloch, P. A. Bobbert, and Dago de Leeuw; Adv. Mater. **19**, 2785 (2007).

[124] R. A. Street, A. Salleo, and M. L. Chabinyc, Phys. Rev. B **68**, 085316 (2003).

[125] Henrique L. Gomes, Peter Stallinga, Franco Dinelli, Mauro Murgia, Fabio Biscarini,

Dago M. de Leeuw, M. Muccini and K. Müllen; Polym. Adv. Technol. **16**, 227 (2005).

[126] A. Salleo, F. Endicott, and R. A. Street; Appl. Phys. Lett. **86**, 263505 (2005).

[127] G. Gu, M.G. Kane, J. E. Doty and A.H. Firester; Appl. Phys. Lett. **87**, 243512 (2005).

[128] H. L. Gomes, P. Stallinga, M Colle, F. Biscarini, D. M. de Leeuw; J. Non Crystalline Solids **352**, 1761 (2006).

[129] R. A. Street, A. Salleo, and M. L. Chabinyc, Phys. Rev. B **68**, 085316 (2003).

[130] G. Goldmann, D. J. Gundlach and B. Batlogg; Appl. Phys. Lett. **88**, 0635901 (2006).

[131] P. Stallinga, H.L. Gomes, F. Biscarini, M. Murgia, D.M. de Leeuw; J. Appl. Phys. **96,** 5277 (2006).

[132] F.L Kalb, K. Mattenberger, B. Battlog; Phys. Rev. B **78**, 035334 (2008).

[133] G. Gu and M. G. Kane; Appl. Phys. Lett. **92**, 053305 (2008).

[134] R. B. Wehrspohn, S.C Deane, I. D. French, I Gale, J. Hewett. M. J. Powell and J. Robertson; J. Appl. Phys. **87**, 144 (2000).

[135] Libsch FR, Kanicki J. Appl. Phys. Lett. **62**, 1286 (1993).

[136] Deane SC, Wehrspohn RB, Powell MJ. Phys. Rev. B **58**, 12625 (1988).

[137] W.B. Jackson, J.M.Marshall and M.D. Moyer; Phys. Rev. B **39**, 1164 (1989).

[138] G.Gu, M.G.Kane and S.C. Mau; J. Appl. Phys. **101**, 014504 (2007).

[139] M. Mottaghi and G. Horowitz, Organic Electronics **7**, 528 (2006).

[140] T. Miyadera, S. D. Wang, T. Minari, T. Tsukagoshi, and Y. Aoyagi; Appl. Phys. Lett. **93**, 033304 (2008).

[141] H.E. Huitema, G.H. Gelinck, E. Van Veenendaal, E.Cantatore, F.J. Touwslager, L.R.R. Schrijnemakers, J.B. Ph. H. Van der Putten, T.C.T. Geuns, M.J. Beenhakkers, P.J.G. Vam Lieshout, R.W. Lafarre, D.M. De Leeuw, B.J.E. Vam Rens, IDW 1663 (2003).

[142] G. Gu, M.G. Kane, J.E. Doty and A.H. Forester; Appl. Phys. Lett. **89**, 253516 (2006).

[143] G. Gu and M.G. Kane; Proc. SPIE **6336**, 63360H (2006).

[144] S. Cipolloni, L. Mariucci, A. Valletta, D. Simeone, F. De Angelis and G. Tortunato; Thin Solid Films **515**, 7546 (2007).

[145] M. Debucquoy, S. Verlaak, S. Strudel, K. Myny, J. Genoe and P. Hermemans; Appl. Phys. Lett. **91**, 103508 (2007).

[146] P. Stoliar, R. Kshirsagar, M. Massi, P. Annibale, C. Albonetti, D. M. de Leeuw, and F. Biscarini; J. Am. Chem. Soc. **129**, 6477 (2007).

[147] F. Dinelli, M. Murgia, J. F. Moulin, M. Cavallini, P. Levy, F. Biscarini, and D. De Leeuw; Phys. Rev. Lett. **92**, 116802 (2004).

[148] R. Ruiz, A. Papadimitratos, A. C. Mayer, G. G. Malliaras; Adv. Mater. **17**, 1795 (2005).

[149] F. Biscarini, P. Samorì, O. Greco, and R. Zamboni; Phys. Rev. Lett. **78**, 2389 (1997).

[150] R.Ruiz, B.Nickel, N.Koch, G.Scoles, L.C.Feldman, R.F.Haglund, A.Kahn, and F.Family; Phys. Rev. Lett. **91**, 136102 (2003).

[151] P.Annibale, C. Albonetti, P.Stoliar, and F. Biscarini; J. Phys. Chem. A **111,** 12854 (2007).

[152] H. Yanagisawa, T. Tamaki, M. Nakamura and K. Kudo; Thin Solid Films **464**, (2004) 398

[153] N. Karl, Synth. Met. **133**, (2003) 694.

[154] S. Verlaak, S. Steudel, P. Heremans, D. Janssen and M. S. Deleuze; Phys. Rev. B **68**, 195409 (2003).

[155] D. Knipp, R. A. Street, A. Völkel, and J. Ho; J. Appl. Phys. **93**, 347 (2003).

[156] A. Pimpinelli, J. Villain, Physics of crystal growth, Cambridge University Press, Cambridge (1999).

[157] Z. Zhang, M. G. Lagally, Science **276**, 377 (1997).

[158] S. R. Forrest; Chem. Rev. **97**, 1793 (1997).

[159] F.C Frank and J.H.Van der Merwe; Proc. R. Soc. London Ser. A **198**, 205 (1949).

[160] A. Zangwill. Physics at Surfaces. Cambridge University Press, 1988.

[161] I. N. Stranski and L. Von Krastanow, Abhandlungen der Mathematisch-Naturwissenschaftlichen Klasse. Akademie der Wissenschaften und der Literatur in Mainz **146**, 797 (1939).

[162] D. G. de Oteyza Ph. D. thesis (2006).

[163] J. Lee, J. H. Kim, and Seongil Im J. Appl. Phys. **95**, 3733 (2004).

[164] C.D. Sheraw, T.N. Jackson, D.L. Eaton, J.E. Anthony; Adv. Mater. **15,** 2009 (2003).

[165] M. Brinkmann, S. Graff, F. Biscarini; Phys. Rev. B **66**, 165430 (2002).